THEORY AND ALGORITHMS FOR A QUASI-OPTICAL LAUNCHER DESIGN METHOD FOR HIGH-FREQUENCY GYROTRONS

by

Ungku Fazri Ungku Farid

A dissertation submitted in partial fulfillment of

the requirements for the degree of

Doctor of Philosophy

(Electrical and Computer Engineering)

at the

University of Wisconsin – Madison

2013

Date of final oral examination: 04/30/2013

The dissertation is approved by the following members of the Final Oral Committee:

      David T. Anderson, Professor, Electrical and Computer Engineering
      Ronald J. Vernon, Emeritus Professor, Electrical and Computer Engineering
      Susan C. Hagness, Professor, Electrical and Computer Engineering
      Cary B. Forest, Professor, Physics
      Nader Behdad, Assistant Professor, Electrical and Computer Engineering
      Konstantin M. Likin, Senior Scientist, Electrical and Computer Engineering

ABSTRACT

Theory and Algorithms for a Quasi-optical Launcher Design Method for High-Frequency Gyrotrons

Ungku Fazri Ungku Farid

Gyrotrons are vacuum tubes that can generate high amounts of coherent high-frequency microwave radiation used for plasma heating, breakdown and current drive, and other applications. The gyrotron output power is not directly usable, and must be converted to either a free-space circular TEM_{00} Gaussian beam or a HE_{11} corrugated waveguide mode by employing mode converters. Quasi-optical mode converters (QOMC) achieve this by utilizing a launcher (a type of waveguide antenna) and a mirror system. Adding perturbations to smooth-wall launchers can produce a better Gaussian shaped radiation pattern with smaller side lobes and less diffraction, and this improvement leads to higher power efficiency in the QOMC. The oversize factor (OF) is defined as the ratio of the operating to cutoff frequency of the launcher, and the higher this value is, the more difficult it is to obtain good launcher designs. This thesis presents a new method for the design of any perturbed-wall TE_{0n} launcher that is not too highly oversized, and it is an improvement over previous launcher design methods that do not work well for highly oversized launchers. This new launcher design method is a fusion of three different methods, which are the Iterative Stratton-Chu algorithm (used for fast and accurate waveguide field propagations), the Katsenelenbaum-Semenov phase-correcting optimization algorithm, and Geometrical Optics. Three different TE_{02} launchers were designed using this new method, 1) a highly oversized (2.49 OF) 60 GHz launcher as proof-of-method, 2) a highly oversized (2.66 OF) 28 GHz launcher for possible use in the quasihelically symmetric stellarator (HSX) transmission line at the University of Wisconsin – Madison, and 3) a compact internal 94 GHz 1.54 OF launcher for use in a compact gyrotron. Good to excellent results were achieved, and all launcher designs were independently verified with Surf3d, a method-of-moments based software. Additionally, the corresponding mirror system for each launcher was incorporated in the full analysis of the complete QOMC system evaluation.

ACKNOWLEDGMENTS

First and foremost, I am thankful to God for granting me the ability, patience and opportunity to complete this research project and dissertation. I am also forever grateful to my mother, Rohana, and my father, Ungku Farid, for their undying support and encouragement throughout all these years.

I would like to thank my research supervisor, Prof. Ronald Vernon, for the knowledge, help, employment and guidance that he has given me. This would not have been possible without him. To my current and former group members, thank you for all of your help. Lastly, I'd like to thank the Department of Energy for funding this research.

TABLE OF CONTENTS
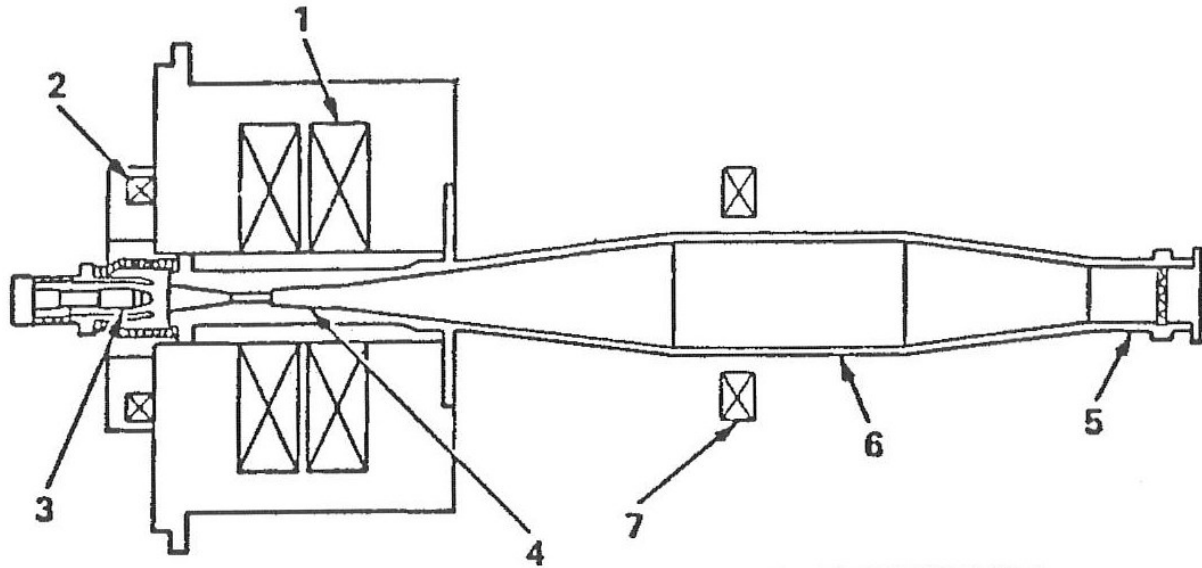
Chapter 1: Introduction

Figure 1.1: Schematic of a VARIAN CW TE_{02} gyrotron with an external mode converter system (not shown on the graph) [1]. The labels are: 1) main magnet coils, 2) gun magnet coil, 3) electron gun, 4) cavity, 5) output waveguide and window, 6) beam collector area, and 7) collector magnet coils. The mode converter system (not pictured) is located to the right of the output waveguide and window.

A gyrotron is a device that can deliver high amounts of (pulsed or CW) output RF power (reaching 2 MW) at frequencies ranging from 1 to 235 GHz. There are no other comparable high-power (>10 kW) RF sources (solid state devices [2] or vacuum tubes [3]) apart from gyrotrons [4]. Gyrotrons are a form of electron resonance maser (ERM), and theoretically gyrotrons can be very efficient (more than 50% with depressed collectors [5]). Among the uses of gyrotrons are: 1) Nuclear Magnetic Resonance (NMR) spectroscopy, 2) industrial applications (mining, welding and ceramic sintering), 3) military applications (millimeter-wave radars and Active Denial Systems (ADS)), 4) active plasma diagnostics, and 5) Electron Cyclotron Resonance Heating (ECRH) and Electron Cyclotron Current Drive (ECCD) in plasma fusion reactors. Recent gyrotron research has been heavily focused on ECRH and ECCD, with the aim of generating safe, renewable and clean energy from the controlled nuclear fusion of deuterium and/or tritium, such as the international nuclear research and engineering project (ITER) [6] in Cadarache, France.

In general, a gyrotron functions the same way as a travelling wave tube (TWT); an electron beam interacts with a magnetic field inside a structure to generate coherent electromagnetic waves. Figure 1.1 shows the schematic

of an early generation gyrotron that has an external mode converter system. Power is coupled from the kinetic energy of the weakly-relativistic injected electron beam to a microwave mode inside the cavity. The spent electrons are then collected on the collector surface. The gyrotron window functions as a vacuum barrier. The window material and dimensions are chosen and designed for minimal power loss and reflection. This window is usually made of a dielectric material with low loss tangent and excellent thermal conductivity (e.g. Chemical Vapor Deposition (CVD) diamond). There are many types of window designs, and normally a single-disk or double-disk type window [7] is utilized for this specific gyrotron type.

Conversion of the gyrotron output mode to a different mode where power is easier and more efficiently extracted is not an easy task. Apart from TE_{0n} modes, most of these gyrotron output modes such as higher order rotating modes (e.g. $TE_{22,6}$ or $TE_{20,9}$) have very high ohmic losses per unit distance, so the power cannot be efficiently transmitted over a moderate distance. Also, converting these high-loss modes to low-loss modes (e.g. TE_{01}) might not be practical or possible. Plus these modes do not propagate well through bends or curves in any conventional high-power microwave transmission line. Extracting the power through conventional waveguide or horn antennas also does not work because the angular spread of the radiation pattern will be too large and a lot of the power cannot be sufficiently recovered. In general, mode converters are employed to transform the microwave output mode from the gyrotron into a more practical and usable mode. Typically this mode is a free space Gaussian beam (i.e. TEM_{00} mode) or the low-loss HE_{11} mode in an overmoded circular corrugated waveguide. For this type of TE_{02} gyrotron, mode conversion is done externally and is achieved by waveguide mode converters or quasi-optical mode converters (QOMC). The former method was invented first and is composed of a series of different types of waveguide converters. Because the TE_{02} mode cannot be directly converted into the HE_{11} mode, the following circuitous mode conversion route is sometimes taken: 1) TE_{02} to TE_{01} using varying-radius mode converters [8]-[10], 2) TE_{01} to TE_{11} using serpentine mode converters [8], and finally 3) TE_{11} to HE_{11} using corrugated waveguides with special slot depth profiles [11].

Waveguide mode converters fail at high power levels because of arcing. Electric field arcs can form at the sharp edges or joints inside the waveguide mode converters and/or transmission lines. The presence of dust particles also causes arcing. Spurious modes from the gyrotron, and misalignment and mode conversion along the transmission line further exacerbate this arcing problem [12]. For short pulses of power, arcing may even occur at

the leading front of the gyrotron pulse [12]. In the HSX (a quasihelically symmetric stellarator operated by the University of Wisconsin – Madison) transmission line, the waveguide mode converter was replaced because waveguide arcing limited the power level operation to 50 kW [13].

A QOMC is normally composed of a Vlasov launcher and mirror(s), and works by transforming the gyrotron output mode into a fundamental circular Gaussian TEM_{00} free-space mode. Under ideal conditions, this TEM_{00} mode can couple 98% of its power to the HE_{11} mode [14]. Basically a Vlasov launcher is a waveguide with a spiral or rectangular cut, and more about it is covered in section 2.3. The launcher works to radiate the waveguide power to the mirror system where the fields are shaped and focused into the circular TEM_{00} mode. These mirrors are located in the radiating near-field region of the launcher and each other. An example is a simple TE_{0n} QOMC which consists of a launcher and a single parabolic reflector, as illustrated in Fig. 1.2. The ideal output of this QOMC would be a collimated beam. Perturbations can be added to the mirror and/or launcher to improve the conversion efficiency (for maximum power transfer). For launchers, perturbations can improve the radiation quality by concentrating more power in the main lobe (that might increase the Gaussian content) and reduce the side lobes. In mirrors, perturbations can raise the Gaussian content of the main lobe. Depending on the requirements of the QOMC, sometimes up to four mirrors are used. Because the mode conversion is done in open space, arcing is much less likely to occur even for high power levels. Furthermore, this method can be extended to other higher order gyrotron output modes (e.g. $TE_{22,6}$) where no such waveguide mode converters exist. For the HSX transmission line, power levels of 100 kW without arcing have been successfully achieved using a simple QOMC similar to Fig. 1.2 [13].

Several methods have been developed for perturbed mirror [14]-[20] and launcher [21]-[26] design. The launcher oversize factor (OF) is a measure of how far a launcher operates above the cut off frequency, and it ranges from 1.00+. The higher the OF, the harder it is to design good launchers. For TE_{0n} type launchers (which are usually external launchers), the OF is typically high, roughly higher than 1.20, whereas for higher order rotating mode launchers, the OF is usually limited to less than 1.15. Internal launchers are normally associated with higher order rotating modes and thus have low OFs, but there are some TE_{0n} type internal launchers that have high OFs. Currently, successful launcher designs with OFs of only up to 1.38 [27] have been reported by other groups. This
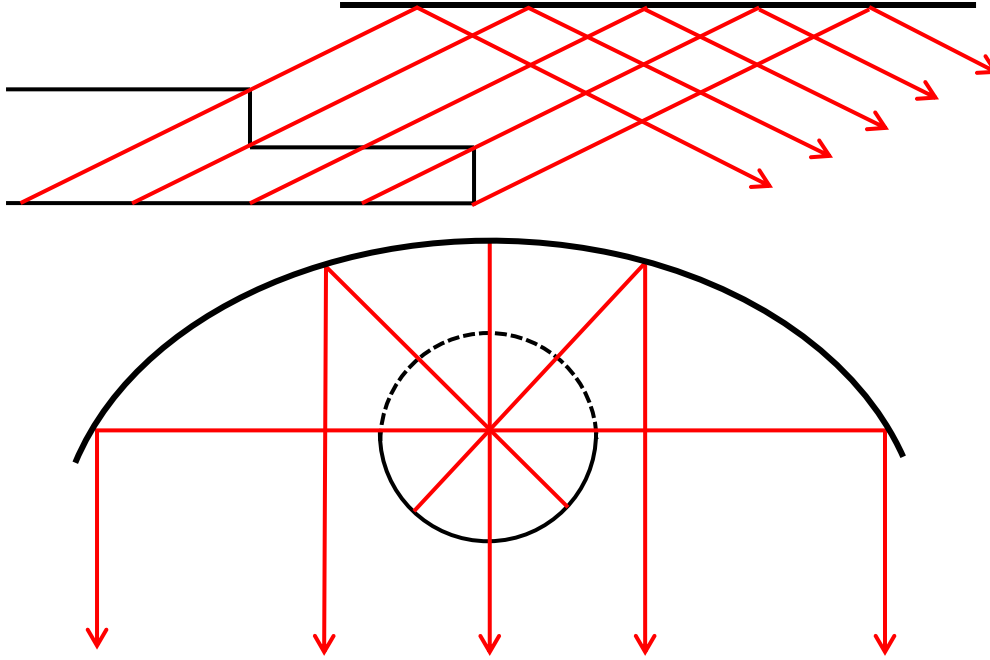
Figure 1.2: Schematic representation of a cross sectional view of a simple TE_{0n} QOMC which consists of a rectangular cut Vlasov launcher and a parabolic reflector. a) Side view (above), and (b) end view (below). Red arrows indicate the propagating rays.

thesis will present a new launcher design method and algorithm for the design of any perturbed-wall TE_{0n} launchers that are not too highly oversized. The relevant background material that comprises this design methodology will also be presented. As will be proven, this launcher design method produces good to excellent results, even for highly oversized launchers where previous methods fail. Three different perturbed-wall TE_{02} launchers covering a wide range of frequency and OFs have been designed using this method; 1) a highly oversized proof-of-method (PoM) 60 GHz 2.49 OF launcher [28], 2) a highly oversized 28 GHz 2.66 OF launcher for possible use by HSX, and 3) a compact 94 GHz 1.54 OF internal launcher for use in an ADS. All results will be independently verified using Surf3d [29], which is the industry-standard QOMC electromagnetic modeling software. Surf3d is a Method of Moments (MoM) based software and the code written for this new launcher design method utilizes a completely different set of methods and algorithms than the MoM. At no point in this launcher design method is Surf3d (or any other MoM based methods) used; Surf3d is an analysis tool and not a synthesis tool, and it is only used to confirm the results of the launcher design method. It will be shown that the results agree to a high level of correlation. No mirror design will be done for this thesis, however, mirrors designed by other people will be included for the analysis of the performance of complete QOMC systems.

Chapter 2 will present the Geometrical Optics (GO) theory for fields in circular waveguides. This theory is useful in providing a simple and intuitive grasp of field propagation in waveguides, but solely basing launcher designs on this theory would not produce good results. Field and modal parameters will be introduced and explained, and some of them will be mathematically derived to further aid in understanding this GO theory. The concept of Brillouin zones, which is integral for the launcher design method, is also covered and explained. This chapter ends with the introduction and explanation of smooth-wall Vlasov launchers.

Chapter 3 is about the phase-correcting Katsenelenbaum-Semenov (KS) algorithm, which is the optimization algorithm used in this launcher design method. This chapter starts off with a basic two phase-corrector system, and is later expanded to cover multi phase-corrector systems. The concept of back propagation of fields which is a crucial component of the KS algorithm is also introduced and discussed. Lastly, two-dimensional phase-unwrapping methods for both ideal (i.e. no phase residues) and non-ideal (i.e. with phase residues) cases with accompanying examples are briefly covered.

Chapter 4 examines the Iterative Stratton-Chu (ISC) method. This is the method used for fast and accurate field propagation inside the waveguide, and is the key enabler for the design of highly oversized launchers. This chapter commences with a discussion of scalar waveguide field propagation methods, which is the current method used by other launcher design methods. The derivation and mathematics of the ISC are discussed in great detail, and methods for efficient implementation of the ISC method are also examined. Example field calculations from both the ISC and scalar methods are provided.

Chapter 5 is the main crux of this thesis, and it is about the new launcher design method. A complete and detailed description of this new method is given, including the design objectives and launcher requirements, and also evaluation criteria of the results. Next, a discussion of the target Gaussian beam definition is provided, followed by an analysis and mathematical derivation of the phase corrections to perturbations conversion. The chapter is capped off with a summary of helpful guidelines for the optimization of essential algorithmic and launcher parameters.

Chapter 6 covers the topic of highly oversized launchers. Two types of perturbed-wall launchers are presented here; the PoM launcher and the HSX launcher. First, problems with the radiation pattern from smooth-wall launchers are investigated. Next, the results of the near-field and far-field patterns for the perturbed-wall

launchers are examined and discussed, and are then compared to the smooth-wall case. For the PoM launcher, additional launcher field analyses (e.g. modal spectrum, field evolution and correlation calculations to Surf3d results) are performed. The mirror systems for both launchers are also introduced. Additionally for the HSX mirror system, a study of beam and power level improvements from its first mirror by the perturbed-wall launcher over the smooth-wall launcher is presented.

In Chapter 7, the launcher design method is extended to design a compact launcher, i.e. the ADS launcher. The definition of compact launchers is first established. Then the accuracy limitations of the ISC method for modeling fields after the launcher cut is looked at using Surf3d simulations as the benchmark. This is done for the smooth-wall and perturbed-wall ADS launchers. Similar to Chapter 6, results of near-field and far-field patterns for the compact perturbed-wall ADS launcher are examined. This chapter concludes with a short description of the single-mirror system used by the ADS.

Chapter 8 will review the strengths and limitations of this launcher design method, and also draw some conclusions from this research. Finally, other potential topics for future investigations are offered.

Chapter 2: Geometrical Optics Theory of Circular Waveguides

2.1 TE and TM fields in circular waveguides

A complete description of the fields in a circular waveguide is integral in understanding gyrotron launchers. Numerous electromagnetics textbooks cover the derivation and analysis of fields in circular waveguides [30, pp. 470-491], [31, pp. 194-198], therefore such details are not presented here. Fields in a smooth and untapered circular waveguide can be represented in the form of TE and TM modes. The H_z component is the generating function for the TE mode and the E_z component is the generating function for the TM mode [30, pp. 272-273, 275-276] [31, pp. 100-104]. All of the other field components can be derived from the generating function. The general and complete equations for the TE modes propagating in the +**z** direction are

$$H_z^{+}(\rho,\phi,z) = J_m(\beta_\rho \rho)(A_{mn}e^{-jm\phi} + B_{mn}e^{+jm\phi})e^{-j\beta_z z}$$

$$H_\phi^{+}(\rho,\phi,z) = \frac{-jm\beta_z}{\beta_\rho^2 \rho} J_m(\beta_\rho \rho)(-A_{mn}e^{-jm\phi} + B_{mn}e^{+jm\phi})e^{-j\beta_z z}$$

$$H_\rho^{+}(\rho,\phi,z) = \frac{-j\beta_z}{\beta_\rho} J'_m(\beta_\rho \rho)(A_{mn}e^{-jm\phi} + B_{mn}e^{+jm\phi})e^{-j\beta_z z}$$

$$E_z^{+}(\rho,\phi,z) = 0$$

$$E_\phi^{+}(\rho,\phi,z) = -Z_{mn}^{TE} H_\rho^{+}(\rho,\phi,z)$$

$$E_\rho^{+}(\rho,\phi,z) = Z_{mn}^{TE} H_\phi^{+}(\rho,\phi,z). \tag{2.1.1}$$

While for TM modes the expressions for fields propagating in the +**z** direction are

$$E_z^{+}(\rho,\phi,z) = J_m(\beta_\rho \rho)(A_{mn}e^{-jm\phi} + B_{mn}e^{+jm\phi})e^{-j\beta_z z}$$

$$E_\phi^{+}(\rho,\phi,z) = \frac{-jm\beta_z}{\beta_\rho^2 \rho} J_m(\beta_\rho \rho)(-A_{mn}e^{-jm\phi} + B_{mn}e^{+jm\phi})e^{-j\beta_z z}$$

$$E_\rho^{+}(\rho,\phi,z) = \frac{-j\beta_z}{\beta_\rho} J'_m(\beta_\rho \rho)(A_{mn}e^{-jm\phi} + B_{mn}e^{+jm\phi})e^{-j\beta_z z}$$

$$H_z^+(\rho,\phi,z)=0$$

$$H_\phi^+(\rho,\phi,z)=\frac{E_\rho^+(\rho,\phi,z)}{Z_{mn}^{TM}}$$

$$H_\rho^+(\rho,\phi,z)=\frac{-E_\phi^+(\rho,\phi,z)}{Z_{mn}^{TM}} \tag{2.1.2}$$

In both modes a factor of $e^{j\omega t}$ is implied here (and throughout this dissertation). The other variables are defined as

$$\omega=2\pi f$$

$$\beta=\frac{2\pi}{\lambda}$$

$$\beta_\rho(\text{TE})=\frac{\chi'_{mn}}{a},\ \beta_\rho(\text{TM})=\frac{\chi_{mn}}{a}$$

$$\beta^2=\beta_\rho^2+\beta_z^2. \tag{2.1.3}$$

The azimuthal index is represented by m (m = 0, 1, 2…) while the radial index is represented by n (n = 1, 2, 3…). J_m is the Bessel function of the first kind of order m and J'_m is the first derivative of J_m. The nth zero of J_m is represented by χ_{mn} (eigenvalue of the TM$_{mn}$ mode) and the nth zero of J'_m is represented by χ'_{mn} (eigenvalue of the TE$_{mn}$ mode). These $e^{\mp jm\phi}$ terms represent fields rotating in the clockwise (CW) and counterclockwise (CCW) direction respectively, with A_{mn} and B_{mn} being their corresponding constants. Alternately, the rotational expressions can also be substituted with $\sin(m\phi)$ or $\cos(m\phi)$. The radius of the waveguide is a, the speed of light is c, the frequency of operation is f, and the wavelength is λ. For this report, the circular waveguide contains only empty space so the permittivity, ε, is ε_o and the permeability, μ, is μ_o. Wave impedances for the TE and TM modes are

$$Z_{mn}^{TE}=\frac{\omega\mu}{(\beta_z)_{mn}},\ Z_{mn}^{TM}=\frac{(\beta_z)_{mn}}{\omega\varepsilon}. \tag{2.1.4}$$

2.2 Geometrical Optics visualization of fields

The fields described in the previous section can be visualized as plane waves propagating and bouncing inside the waveguide [32]. From this point onward, for the sake of simplicity and brevity, only the H_z field (the generating function of the TE mode) will be described and analyzed in terms of Geometrical Optics (the same approach can be expanded for the other mode and fields).

Geometrical Optics of circular waveguides requires a basic understanding of Bessel functions. The Bessel function of the first kind, J_m can be expressed as

$$J_m(x) = \frac{H_m^{(1)}(x) + H_m^{(2)}(x)}{2} \tag{2.2.1}$$

where $H_m^{(1)/(2)}(x)$ are known respectively as the Hankel functions of the first and second kind (also called Bessel functions of the third kind). These Hankel functions can also be expressed in terms of other types of Bessel function,

$$H_m^{(1)/(2)}(x) = J_m(x) \pm jY_m(x) \tag{2.2.2}$$

where $Y_m(x)$ is called the Neumann function (also known as Bessel function of the second kind), and it has a singularity at the origin. For large arguments where $x > m$, the Hankel function can be approximated as

$$H_m^{(1)/(2)}(x) \approx \sqrt{\frac{2}{\pi\sqrt{x^2 - m^2}}} e^{j\left(\pm\sqrt{x^2 - m^2} \mp m \, \cos^{-1}\left(\frac{m}{x}\right) \mp \frac{\pi}{4}\right)}. \tag{2.2.3}$$

Equation (2.2.3) demonstrates the fact that the incoming part (i.e. radially incoming) of the field is signified by $H_m^{(1)}(x)$, while the outgoing part (i.e. radially outgoing) of the field is denoted by $H_m^{(2)}(x)$. Only the phase component is of interest, and in practice, the phase approximation of Eq. (2.2.3) is close to the exact value, as shown in Fig 2.2.1. This approximation becomes better the farther away it is from the origin and for higher order modes.

The argument x in Eqs (2.2.1) to (2.2.3) is a placeholder for $\beta_\rho \rho$, and $\beta_\rho \rho$ is equivalent to $\chi'_{mn}\left(\frac{\rho}{a}\right)$, with a minimum value of $\chi'_{11} = 1.841$ (lowest order TE_{11} mode).
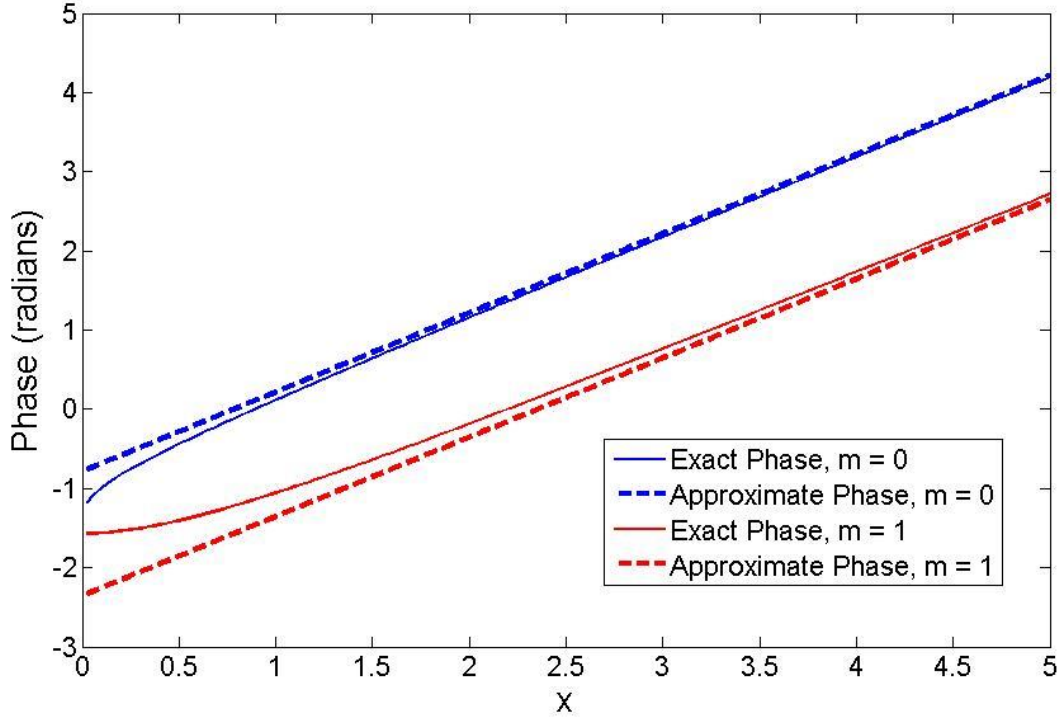
Figure 2.2.1: Comparison between the phase values of the approximation of $H_m^{(1)}(x)$ in Eq. (2.2.3) and the exact value of $H_m^{(1)}(x)$ for m = 0 and m = 1.

Taking Eq. (2.2.3) and inserting it into the outgoing H_z field expression in Eq. (2.1.1) gives a phase component of

$$\arg(H_z^{+}(\rho,\phi,z)) \approx -\sqrt{\beta_\rho^2 \rho^2 - m^2} + m\cos^{-1}\left(\frac{m}{\beta_\rho \rho}\right) - m\phi - \beta_z z + \frac{\pi}{4}. \tag{2.2.4}$$

A wavefront with a constant phase of K for the outgoing H_z field can be described mathematically as

$$\arg(H_z^{+}(\rho,\phi,z)) - K = 0, \tag{2.2.5}$$

and the gradient of this wavefront is

$$\mathbf{N}(\rho,\phi,z) = \nabla(\arg(H_z^{+}(\rho,\phi,z)) - K) \approx \beta_\rho \sqrt{1 - \frac{m^2}{\beta_\rho^2 \rho^2}}\hat{\boldsymbol{\rho}} + \frac{m}{\rho}\hat{\boldsymbol{\phi}} + \beta_z \hat{\mathbf{z}}. \tag{2.2.6}$$

Locally, these planes of constant wavefronts can be thought of as a continuous beam of rays, with the gradient of the wavefront representing the direction of the rays, as shown in Fig. 2.22. The reader is reminded that on the waveguide walls, all these approximations are very close to the exact value. On the waveguide walls, Eq. (2.2.6) becomes

$$\mathbf{N}(a,\phi,z) \approx \frac{\sqrt{\chi'_{mn}{}^2 - m^2}}{a} \hat{\boldsymbol{\rho}} + \frac{m}{a} \hat{\boldsymbol{\phi}} + \beta_z \hat{\mathbf{z}}. \tag{2.2.7}$$

In the waveguide axis plane, it can be seen that the rays propagate at a fixed angle to the waveguide axis, and this angle is known as the axial bounce angle, θ_b. Mathematically, the axial bounce angle is derived as follows,

$$\cos\theta_b = \frac{\mathbf{N}(a,\phi,z)\cdot\hat{\mathbf{z}}}{|\mathbf{N}(a,\phi,z)||\hat{\mathbf{z}}|} = \frac{\beta_z}{\sqrt{\beta_\rho{}^2 + \beta_z{}^2}} = \frac{\beta_z}{\beta}, \quad \sin\theta_b = \frac{\beta_\rho}{\beta}. \tag{2.2.8}$$

In the transverse plane (i.e. the radial cross section) on the waveguide walls, the rays propagate normal to the wavefront of

$$\mathbf{N_t}(a,\phi,z) \approx \frac{\sqrt{\chi'_{mn}{}^2 - m^2}}{a} \hat{\boldsymbol{\rho}} + \frac{m}{a} \hat{\boldsymbol{\phi}}. \tag{2.2.9}$$

Similarly, the rays propagate at a fixed angle, ψ, in the azimuth. This angle can be obtained mathematically as

$$\cos\psi = \frac{\mathbf{N_t}(a,\phi,z)\cdot\hat{\boldsymbol{\phi}}}{|\mathbf{N_t}(a,\phi,z)||\hat{\boldsymbol{\phi}}|} = \frac{m}{\chi'_{mn}}. \tag{2.2.10}$$

In the radial cross section, between successive reflections on the waveguide walls, each ray would be shifted azimuthally with respect to the waveguide axis by an angle called the azimuthal bounce angle, 2ψ.
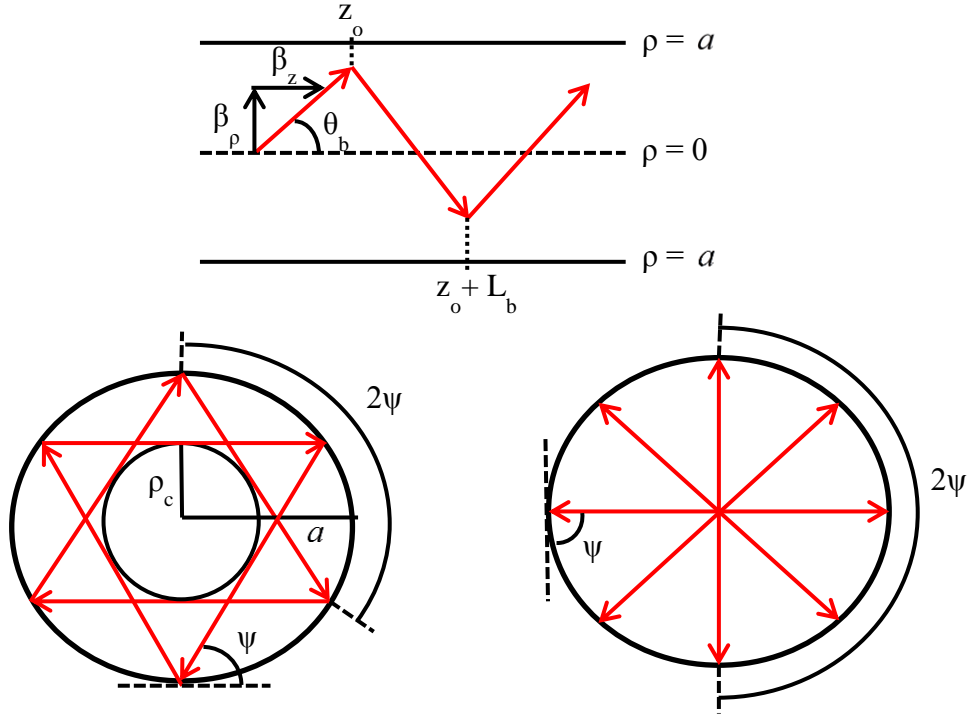
Figure 2.2.2: Rays of a general TE$_{mn}$ mode propagating inside a waveguide by bouncing along the waveguide walls, with the arrows representing the propagation direction. a) Above, schematic representation of the side view (waveguide axis plane) of a generalized TE$_{mn}$ mode. b) Left, radial cross-section (transverse plane) of a TE$_{22,6}$ mode, where the value of $2\pi / 2\psi$ is close to 3. c) Right, radial cross-section of a generalized TE$_{0n}$ mode, where the value of $2\pi / 2\psi$ is 2.

From a radial cross-section view (Fig. 2.2.2b), all of the bouncing rays are tangent to an inner circle called the caustic circle with a radius of

$$\rho_c = a\cos\psi. \tag{2.2.11}$$

No rays whatsoever propagate inside this caustic circle, however, this does not mean that the fields inside the caustic circle are zero. Qualitatively, the fields decay radially inside the caustic circle. In the waveguide axis plane, between consecutive reflections on the waveguide walls, each ray would have travelled a distance of one bounce length projected along the waveguide axis, defined as

$$L_b = \frac{2a}{\tan\theta_b}\sqrt{1 - \left(\frac{m}{\chi'_{mn}}\right)^2}. \tag{2.2.12}$$

For a fixed waveguide radius and frequency, θ_b increases for higher order TE_{mn} modes. For a fixed waveguide radius and mode, θ_b also increases for increasing frequency, f. As a mode operates farther away from the cutoff frequency, f_c, θ_b becomes smaller ($\lim_{f \gg f_c} \theta_b = 0^\circ$) and as a mode operates closer to f_c, θ_b gets larger ($\lim_{f \to f_c} \theta_b = 90^\circ$). A parameter for indicating how far a mode operates from the cutoff frequency is the oversize factor

$$OF = \frac{f}{f_c} = \csc \theta_b. \tag{2.2.13}$$

There is a special class of TE modes, TE_{0n} modes, where there is no field variation in the azimuthal direction (m = 0). For these TE_{0n} modes, the azimuthal bounce angle, 2ψ, is always 180° and there is no caustic radius ($\rho_c = 0$). Additionally for this class of modes, the $H_\phi(\rho,\phi,z)$ and $E_\rho(\rho,\phi,z)$ field components are exactly zero everywhere, and the H_z generating function is the only nonzero field component on the waveguide walls. Table 2.2.1 illustrates the different field structure and mode parameters between two different TE modes.

Another way of describing the TE_{mn} field propagation mathematically (only valid for non-TE_{0n} modes) can be done by utilizing the Bessel identity [33, p. 13]

$$\frac{m}{2\pi x} J_m(x) = \int_0^{2\pi} e^{jx\sin\phi'-m\phi'} \cos \phi' d\phi'. \tag{2.2.14}$$

Rewriting the H_z generating function in Eq. (2.1.1) with the Bessel function identity of Eq. (2.2.9) yields

$$H_z^+(\rho,\phi,z) = \frac{2\pi\beta_\rho\rho}{m} \int_0^{2\pi} e^{-j\beta S(\rho,\phi,z,\phi')} \cos \phi' d\phi', \tag{2.2.15}$$
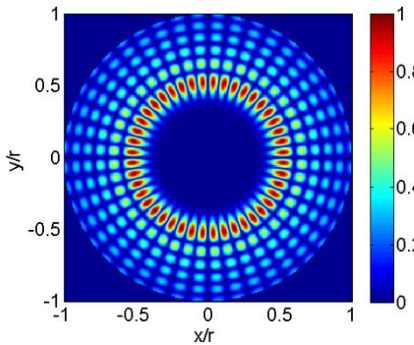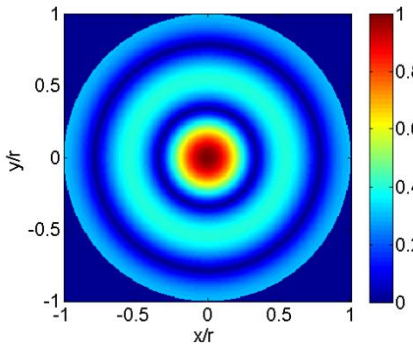
where

$$S(\rho,\phi,z,\phi',z') = \frac{1}{\beta}\Big[\beta_z z - \beta_\rho\rho\sin\phi' + m(\phi+\phi')\Big]. \tag{2.2.16}$$

Equation (2.2.15) describes the H_z generating function as a spectrum of plane waves. At the waveguide walls, it can be seen that

$$\nabla S(a,\phi,z,\phi') = \frac{\partial S(a,\phi,z,\phi')}{\partial \phi'} = 0, \qquad (2.2.17)$$

when $\phi' = \psi$ from Eq. (2.2.10). The value $S(\rho,\phi,z,\phi')$ is an eikonal, and the value ∇S (normal of the TE_{mn} fields on the waveguide walls) represents the propagation direction of the rays [34].

Table 2.2.1: Field Structure and Mode Parameters Comparison Between the $TE_{22,6}$ Mode and TE_{02} Mode. For the TE_{02} mode, three types of launchers are presented: 1) the PoM launcher, 2) the HSX launcher, and 3) the ADS launcher.

|**H**| radial cross section				
mode	$TE_{22,6}$	TE_{02} (PoM)	TE_{02} (HSX)	TE_{02} (ADS)
waveguide radius, a	2.10 cm	1.39 cm	3.175 cm	0.55 cm
Frequency, f	110 GHz	60 GHz	28 GHz	94 GHz
OF	1.06	2.49	2.66	1.54
θ_b	70.80°	23.67°	22.12°	40.35°
2ψ	122.34°	180°		
L_b	1.28 cm	6.34 cm	15.62 cm	1.29 cm
ρ_c	1.01 cm or $0.481a$	0 cm		
α_1	74.05°	34.55°	32.56°	52.15°
D_1	3.77 cm	12.68 cm	31.25 cm	2.59 cm

2.3 Brillouin zones and Vlasov launchers

From the preceding section, it can be seen that all of the rays completely bounce off a segment of the waveguide walls, and this segment is called a Brillouin zone [32]. Brillouin zones are periodic and when unrolled onto a planar surface, they form parallelograms. This concept is illustrated in Fig 2.3.1. A Brillouin zone is not unique; geometrically translating or rotating a Brillouin zone will still yield a Brillouin zone. A different way of thinking about Brillouin zones is as a set of cylindrical mirrors that reflects and propagates beams. These cylindrical mirrors border one another (no overlapping) so that a complete circular waveguide is formed. Thus, by removing just one Brillouin zone from a circular waveguide, all of the fields will exit through this hole and no fields at all (or power for that matter) will further propagate in the waveguide (neglecting diffraction). In Vlasov launchers, the last Brillouin zones at the end of an unperturbed waveguide are cut off so that all of the fields and power in the waveguide propagate to free space [35]. In general, the radiation patterns out of Vlasov launchers are severely difficult to work with and perturbations on the walls and/or outside mirrors are utilized to help improve the radiation pattern. The side view of two different launchers is shown in Fig. 2.3.2.

As shown in Fig. 2.3.1, the rays bounce on the waveguide walls along a helical line, and this pitch angle is defined mathematically as

$$\alpha_1 = \tan^{-1}\left(\frac{\psi \tan \theta_b}{\sin \psi} \right). \tag{2.3.1}$$

After a ray has traversed a full 2π radians in the azimuth on the waveguide walls, it will have travelled a distance in the axial direction by an amount of

$$D_1 = 2\pi a \cot \alpha_1, \tag{2.3.2}$$

and this parameter is called the pitch distance. For a particular TE_{mn} mode, if D_1 is an integer multiple of the bounce length, L_b, then the ray picture of that mode would also make an integer number of bounces in the azimuth as it completes a full 2π radians in the radial cross-sectional plane (i.e. the value of $2\pi / 2\psi$ is also an integer). The opposite is also true.
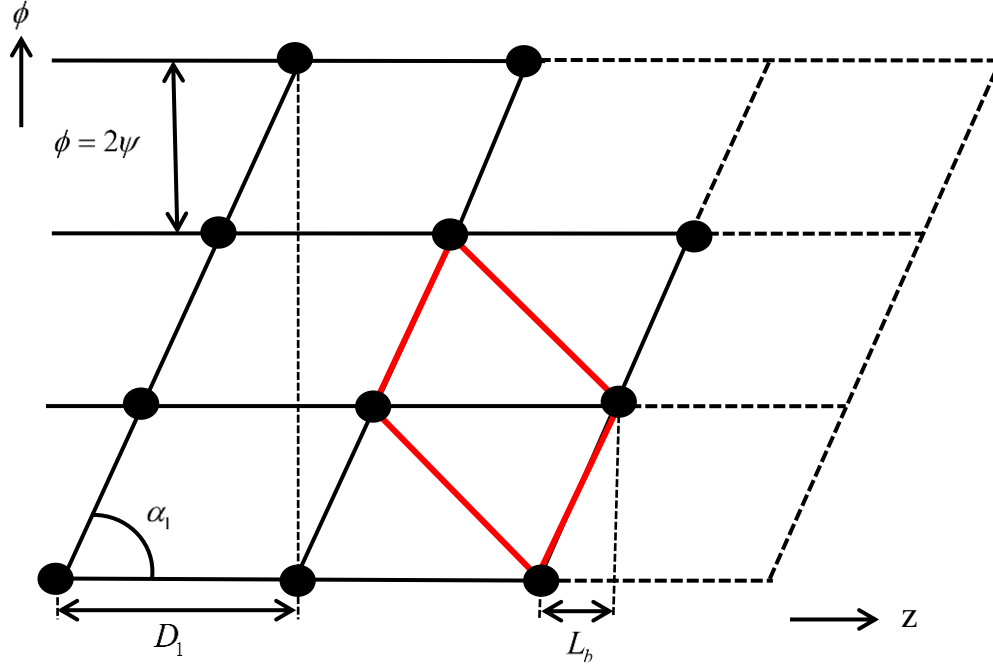
a) Brillouin zones for a TE$_{22,6}$ mode, where 2ψ is close to 120°, and D_1 / L_b is close to 3.
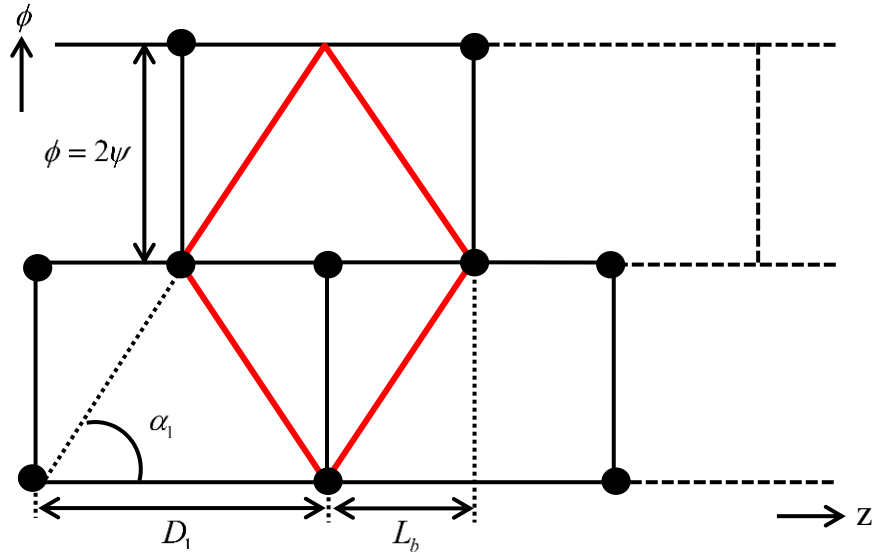
b) Brillouin zones for a TE$_{02}$ mode, where 2ψ is exactly 180°, and D_1 / L_b is 2.

Figure 2.3.1: Unrolled Brillouin zones for different TE modes. Broken lines indicate regions to be excised in a Vlasov launcher. Black dots trace out the rays bouncing location on the walls. Red parallelograms indicate other possible Brillouin zone. Figures are not to scale.
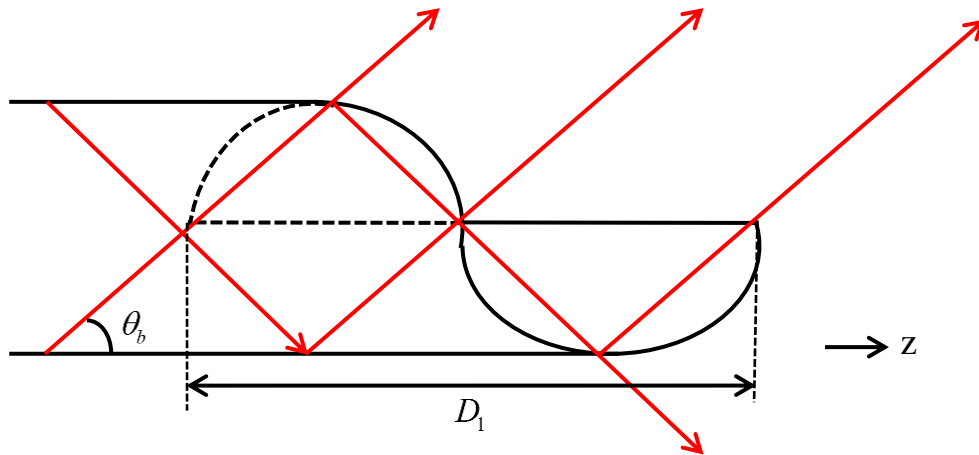
a)   Spiral-cut $TE_{22,6}$ (rotating mode) launcher.
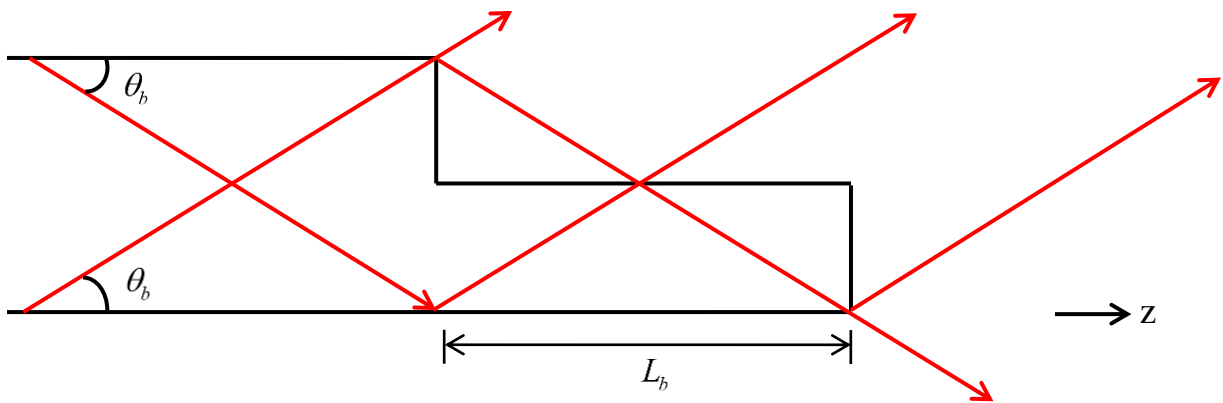
b) Rectangular-cut TE_{02} (non-rotating mode) launcher.

Figure 2.3.2: Schematic representation of the side view of two different Vlasov launchers. Red arrows indicate propagating rays in or exiting the launchers. Figures are not to scale.

Chapter 3: The Katsenelenbaum-Semenov Method

The Katsenelenbaum-Semenov (KS) method [36] is an iterative phase-correcting optimization algorithm and it is widely used in solving electromagnetic related problems and applications [17] [18] [21] [23]. It is relatively simple to implement, very dynamic and robust (applicable to a wide range of uses), and it is also quite fast. However, this algorithm does not guarantee that the result is the globally optimized solution; only the local optimum solution is obtained. Additionally, since this algorithm is based on the phase information, phase-unwrapping methods might need to be employed. Depending on the accuracy requirement of the unwrapped phase, sometimes very sophisticated phase-unwrapping methods are needed.

3.1 Basic two phase corrector Katsenelenbaum-Semenov method

A set of two thin lenses can be used in principle to transform a certain initial incident beam into a specified resulting target beam, if the transformation is not too radical. These thin lenses can be thought of as ideal phase-shifters that only change the phase distribution of the fields while preserving the amplitude distribution. As a beam passes through a thin lens, its phase distribution is altered, and by the process of constructive and destructive interference, the amplitude and phase of that beam will change as the beam propagates away, thereby changing the initial properties of the beam. A pictorial explanation of this concept for a pair of phase-correctors is presented in Fig. 3.1.1. In this formulation, phase correctors are planar-shaped (for simplicity), but, without loss of generality, these phase correctors can be extended into other shapes such as cylindrical or parabolic reflectors. It must also be noted that the starting surface (i.e. initial guess) of the phase correctors might or might not lead to different solutions (e.g. phase corrections) [15].

From Fig. 3.1.1, the initial incident field $\mathbf{E_o}$ has an amplitude distribution of E_o and phase distribution of ϕ, and the target beam $\mathbf{E_T}$ has an amplitude distribution of E_T and phase distribution of θ. Both $\mathbf{E_o}$ and $\mathbf{E_T}$ fields are only polarized in the $\mathbf{x}$ direction. $\mathbf{E_o}$ is propagated through the first phase corrector and acquires an extra phase term of ψ_o^n and $\mathbf{E_T}$ is back propagated (evaluating a beam at its earlier evolution) across the second phase corrector and attains a phase term of ψ_T^n. Initially these phase correctors have zero "thickness" so the extra phase terms are

zero, $\psi_o^{n=0} = \psi_T^{n=0} = 0$. Now there are two options, whether to do the phase corrections on the left phase corrector first and then do the second phase corrections on the right phase corrector or vice versa (sometimes both methods would yield the same result but with different phase corrector profiles, however, in certain applications like the launcher design method in Chapter 5, one of the methods would give better results). From here on, the discussion will focus on the former method. $\mathbf{E_T}$ is back propagated by z = -d to the left phase corrector, resulting in an amplitude distribution of $\mathbf{E_T}'$ and phase distribution of $\alpha_T^{n=0}{}'$. The first phase corrections on the left phase corrector, $\psi_o^{n=1}$, is taken as the phase difference between $\mathbf{E_T}'$ and $\mathbf{E_o}$, and it is added to the "thickness" of the left phase corrector. This process is repeated for the right phase corrector (now $\mathbf{E_o}$ undergoes an extra phase term of $\psi_o^{n=1}$ instead of $\psi_o^{n=0} = 0$); $\mathbf{E_o}$ is forward propagated by z = +d to the right phase corrector resulting in an amplitude of E'_o and phase of $\alpha_o^{n=0}{}'$. The phase correction on the right phase corrector, $\psi_T^{n=1}$ is taken as the phase difference between $\mathbf{E_T}$ and $\mathbf{E_o}'$, and then it is added to the "thickness" of the right phase corrector. These steps can be repeated until convergence (the complex scalar coupling coefficient, c_{cs}, of the $\mathbf{x}$ co-polarization between $\mathbf{E_o}'$ and $\mathbf{E_T}$ is 99.9% or any other chosen value) is achieved i.e. the phase differences between iterations, $\Delta\beta_o^n$ and $\Delta\beta_T^n$ is close to zero. The flowchart of this algorithm is presented in Fig. 3.1.2. The equations to convert the phase shifts to actual perturbations will be covered in section 5.3.

$$\alpha_o^n(x,y) = \phi(x,y) + \psi_o^n(x,y) \qquad\qquad \alpha_T^n(x,y) = \theta(x,y) - \psi_T^n(x,y)$$

$$\psi_o^{n+1}(x,y) = \alpha_T^n{}'(x,y) - \phi(x,y) \qquad\qquad \psi_T^{n+1}(x,y) = \theta(x,y) - \alpha_o^n{}'(x,y)$$
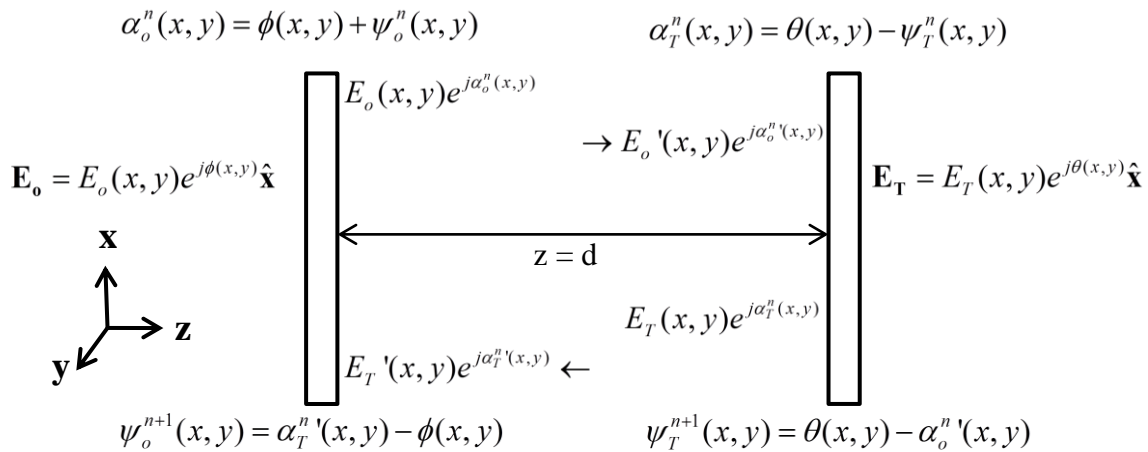
Figure 3.1.1: Pictorial illustration for the K-S method for two phase-correctors situated on the x-y plane and beam propagation along the z axis. The initial incident field is $\mathbf{E_o}$ and the target field is $\mathbf{E_T}$. The n superscript indicates iteration number, the rightward arrow indicates forward propagation and the leftward arrow indicates back propagation. The primes represent field propagation over a distance of z = ±d.

Figure 3.1.2: Flowchart for the KS method for two phase correctors as described in Fig. 3.1.1

3.2 General theory of back propagating fields

While forward propagation of beams or fields is intuitive and easily understood, the concept of back propagation might not be as clear. Back propagation is defined as the evaluation of a beam at an earlier point of its propagation evolution, similar to rewinding a video. Back propagation is unphysical and only exists as theoretical and mathematical concepts. A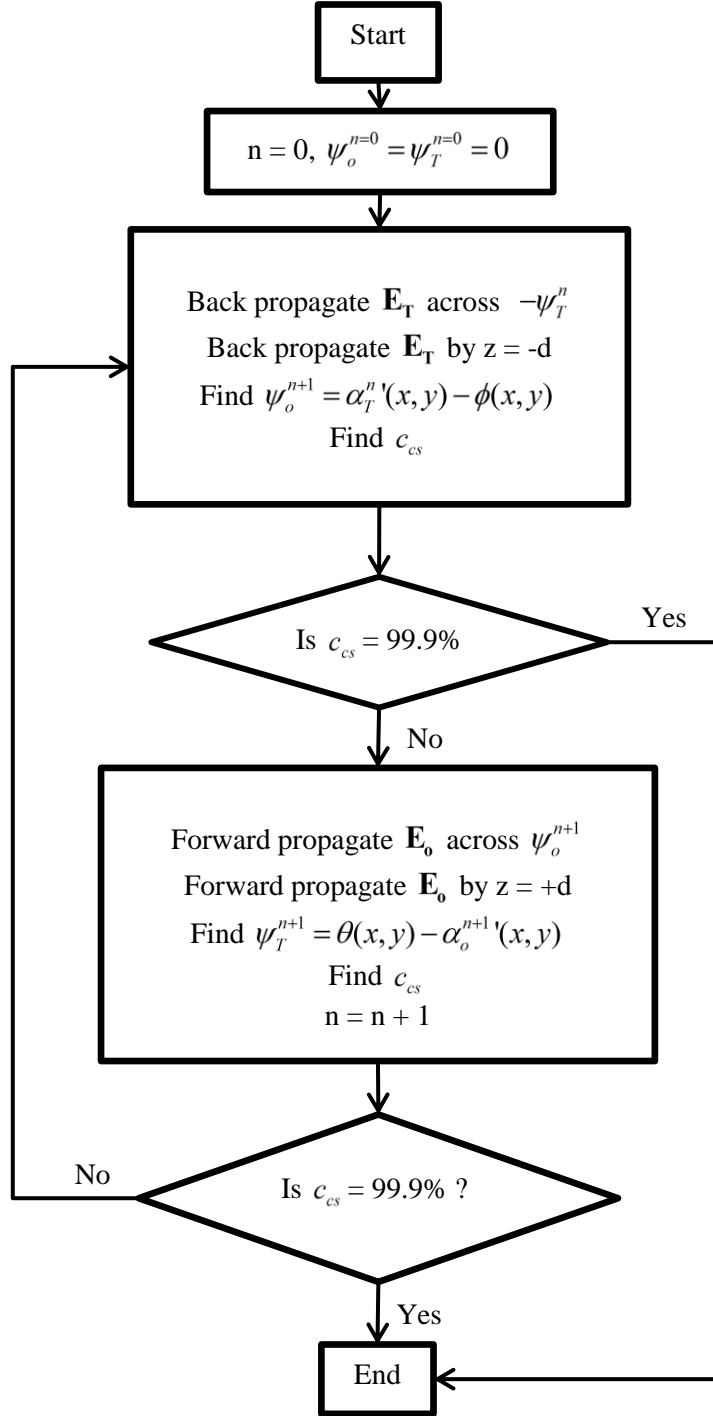 simple mathematical analysis of back propagation will be performed [20] to reinforce this concept. Similar to Fig. 3.1.1, an electric field, $\mathbf{E}$ is propagating in the $+\mathbf{z}$ direction with a spectral distribution of $\tilde{\mathbf{E}}$, defined as

$$\mathbf{E}(x,y,z) = \frac{1}{2\pi}\int_{-\infty}^{\infty}\int_{-\infty}^{\infty}\tilde{\mathbf{E}}(\beta_x,\beta_y)e^{-j\beta_x x}e^{-j\beta_y y}e^{-j\beta_z z}d\beta_x d\beta_y \tag{3.2.1}$$

where $\beta_z = \sqrt{\beta^2 - \beta_x^2 - \beta_y^2}$. From Eq. (3.2.1), $\mathbf{E}$ is the 2 Dimensional Fourier Transform of $\tilde{\mathbf{E}}$. $\mathbf{E}$ can be forward propagated or back propagated respectively by a $\pm\delta z$ amount, yielding

$$\mathbf{E}(x,y,z\pm\delta z) = \frac{1}{2\pi}\int_{-\infty}^{\infty}\int_{-\infty}^{\infty}\tilde{\mathbf{E}}(\beta_x,\beta_y)e^{-j\beta_x x}e^{-j\beta_y y}e^{-j\beta_z(z\pm\delta z)}d\beta_x d\beta_y. \tag{3.2.2}$$

In both forward and back propagation cases in Eq. (3.2.2), the direction of power flow (the Poynting vector, $\mathbf{S}$) is the same as the wavevector ($\boldsymbol{\beta} = \beta_z\hat{\mathbf{z}}$), which is in the $+\mathbf{z}$ direction. This is known as a right handed system. Taking the conjugate of Eq. (3.2.1) (and after applying some change of variables) yields,

$$\mathbf{E}^*(x,y,z) = \frac{1}{2\pi}\int_{-\infty}^{\infty}\int_{-\infty}^{\infty}\tilde{\mathbf{E}}^*(-\beta_x,-\beta_y)e^{-j\beta_x x}e^{-j\beta_y y}e^{j\beta_z z}d\beta_x d\beta_y, \tag{3.2.3}$$

where $\mathbf{E}^*$ is the same $\mathbf{E}$ in Eq. (3.2.1) except now the propagation direction is reversed (-$\mathbf{z}$ direction). Applying the same analysis in Eq. (3.2.2) to $\mathbf{E}^*$ produces,

$$\mathbf{E}^*(x,y,z\pm\delta z) = \frac{1}{2\pi}\int_{-\infty}^{\infty}\int_{-\infty}^{\infty}\tilde{\mathbf{E}}^*(-\beta_x,-\beta_y)e^{-j\beta_x x}e^{-j\beta_y y}e^{j\beta_z(z\pm\delta z)}d\beta_x d\beta_y. \tag{3.2.4}$$

Now $-\delta z$ is considered as forward propagating the $\mathbf{E}^*$ field (move in the -$\mathbf{z}$ direction) and $+\delta z$ as back propagating the $\mathbf{E}^*$ field (i.e. evaluating the $\mathbf{E}^*$ field at an earlier point of its evolution in $\mathbf{z}$). In conclusion, for this

case, back propagating the **E** field is equivalent to forward propagating the **E*** field and vice versa (this is not a general formulation because the **H** field was not included in the analysis). Using the same forward propagating method for both forward propagation and back propagation also reduces the complexity of the KS method.

The validity of Eqs. (3.2.3) and (3.2.4) can be proven by taking the complex conjugate of Maxwell's equations (Faraday's law and Ampere's law) and rewriting them in the form of

$$\nabla \times \mathbf{E}^* = -j\omega(-\mu)\mathbf{H}^* \tag{3.2.5}$$

$$\nabla \times \mathbf{H}^* = \mathbf{J}^* + j\omega(-\varepsilon)\mathbf{E}^*. \tag{3.2.6}$$

In order for the conjugate fields to satisfy Maxwell's equations, both μ and ε must be negative. This is known as a left handed system, where the direction of power flow is opposite to the propagation direction [37], i.e. **E*** and **H*** are propagating in the –**z** direction, but the Poynting vector, **S ,** is in the +**z** direction. Utilizing this system, back propagation of **E** and **H** is achieved by changing ε and μ to negative values, setting the source fields of **E** and **H** respectively to **E*** and **H***, and then forward propagating the **E*** and **H*** fields.

Another way of rewriting Eqs. (3.2.5) and (3.2.6) is

$$\nabla \times \mathbf{E}^* = -j\omega\mu(-\mathbf{H}^*) \tag{3.2.7}$$

$$\nabla \times \mathbf{H}^* = \mathbf{J}^* + j\omega\varepsilon(-\mathbf{E}^*), \tag{3.2.8}$$

where instead of collecting the negative values with ε and μ, the negative values are now collected with the conjugated fields. This formulation still remains a right handed system. For this case, back propagation is done by setting the source **E** and **H** fields respectively to –**E*** and –**H***, and then forward propagating the –**E*** and –**H*** fields. However, for this formulation, between each successive back propagations, the **E*** and **H*** source fields must be multiplied by -1, as required in Eqs. (3.2.7) and (3.2.8). For this research, this is the preferred method because values of ε and μ do not have to be changed for back propagation.

3.3 General K phase corrector Katsenelenbaum-Semenov method

The KS method does not have to be limited to two phase correctors; it can be generalized to include numerous phase correctors. In certain applications, the field distribution between the initial and target fields can be large, and/or the perturbations are required to be small. Instead of distributing the phase shifts across two phase correctors, the phase shifts can be divided into many more phase correctors, resulting in smaller perturbations per phase corrector [15]. A diagram of a generalized K phase corrector KS method is presented in Fig. 3.3.1. For K phase correctors there are K! ways of doing the phase corrections (e.g. 6 total configurations for K = 3; the first phase corrections can be done for the center phase corrector, followed by the right phase corrector and lastly the left phase corrector). For simplicity, the phase corrections are calculated from right to left (i.e. from the Kth phase corrector to the first phase corrector), and this is the opposite approach taken in section 3.1. Similar to section 3.1, although the method is presented for planar phase correctors for simplicity, it can be generalized to other types of surfaces.

$$\psi_K^n(x,y) = \theta(x,y) - \alpha_{K-1}^n{'}(x,y)$$
$$\psi_k^n(x,y) = \sigma_{K-k}^n{'}(x,y) - \alpha_{k-1}^n{'}(x,y)$$
$$\psi_1^n(x,y) = \sigma_{K-1}^n{'}(x,y) - \phi(x,y)$$
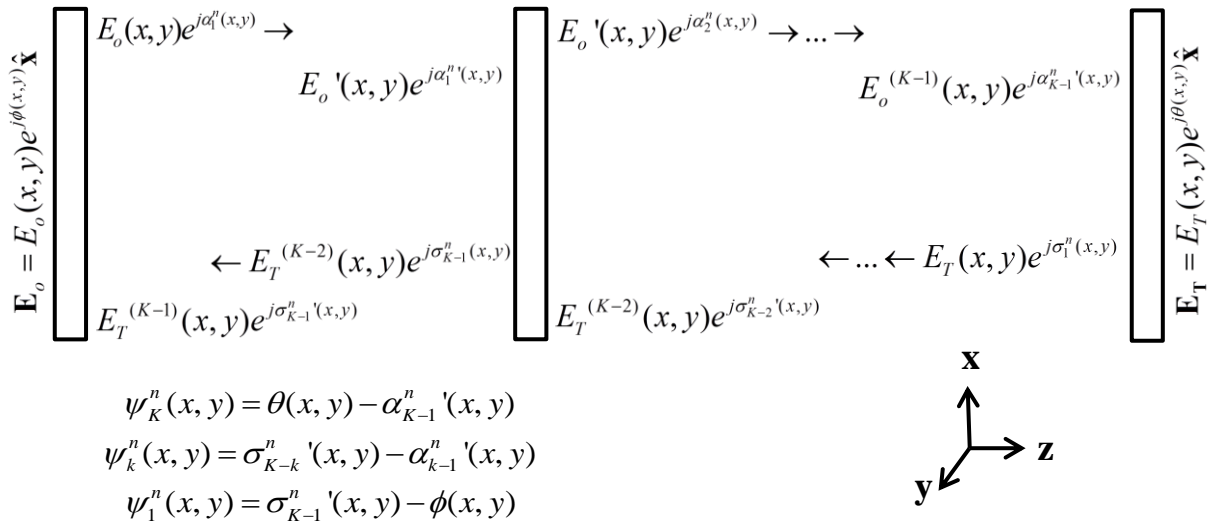
Figure 3.3.1: Diagram of the KS method for a system of K phase correctors. The phase correctors are numbered from left to right, and are represented by k (k = 1, 2, ..., K). The variable n indicates the iteration number (n = 0, 1, ..., N). The primes indicate propagation over a certain distance in $\pm\mathbf{z}$.

From Fig. 3.3.1, starting off with zero phase shifts everywhere $(\psi_k^{n=0} = 0)$, $\mathbf{E_o}$ is forward propagated all the way to the last phase corrector, and the phase difference between $\mathbf{E_T}$ and $\mathbf{E_o}^{(K-1)}$ is taken as the phase correction on the last phase corrector, ψ_K^n. This process is repeated for the penultimate phase corrector (ψ_{K-1}^n); $\mathbf{E_o}$ is forward

propagated to the penultimate phase corrector resulting in $\mathbf{E_o}^{(K-2)}$ and $\mathbf{E_T}$ is back propagated across the last phase corrector (and experiences a phase shift of ψ_K^n) yielding $\mathbf{E_T}'$, and the phase difference between $\mathbf{E_o}^{(K-2)}$ and $\mathbf{E_T}'$ is taken as ψ_{K-1}^n . This whole step is repeated for the rest of the phase correctors until convergence is achieved, and if necessary, it can be repeated for other iterations too (n = 1, 2, 3, …., N). The flowchart for this generalized method is presented in Fig. 3.3.2.


```
                          ┌─────────┐
                          │  Start  │
                          └─────────┘
                               │
                ┌──────────────────────────────────────┐
                │ Set n = 0, k = K, ψ^{n=0}_{k=K,K-1,…1}=0 │
                └──────────────────────────────────────┘
                               │
        ┌──────────────────────────────────────────────┐
        │ Forward propagate E_o to E_o^{(k-1)}           │
        │ Back propagate E_T to E_T^{(K-k)}              │
        │ Find ψ_k^n(x,y) = σ_{K-k}^n '(x,y) − α_{k-1}^n '(x,y) │
  ┌──── │ k = k-1                                        │
  │     │ Find c_cs                                      │
  │     └──────────────────────────────────────────────┘
  │  ┌──────────┐
  │  │ k = K    │
  │  │ n = n+1  │
  │  └──────────┘
  │      Yes
  │  ◇ Is k = 1 ?  ◇ Is c_cs = 99.9% ?
  │   No       No                   Yes
  │                               ┌─────┐
  │                               │ End │
  │                               └─────┘
```

Forward propagate $\mathbf{E_o}$ to $\mathbf{E_o}^{(k-1)}$

Back propagate $\mathbf{E_T}$ to $\mathbf{E_T}^{(K-k)}$

Find $\psi_k^n(x,y) = \sigma_{K-k}^n{}'(x,y) - \alpha_{k-1}^n{}'(x,y)$

$k = k-1$

Find c_{cs}

$k = K$
$n = n+1$

Yes

No

No

Is k = 1 ?
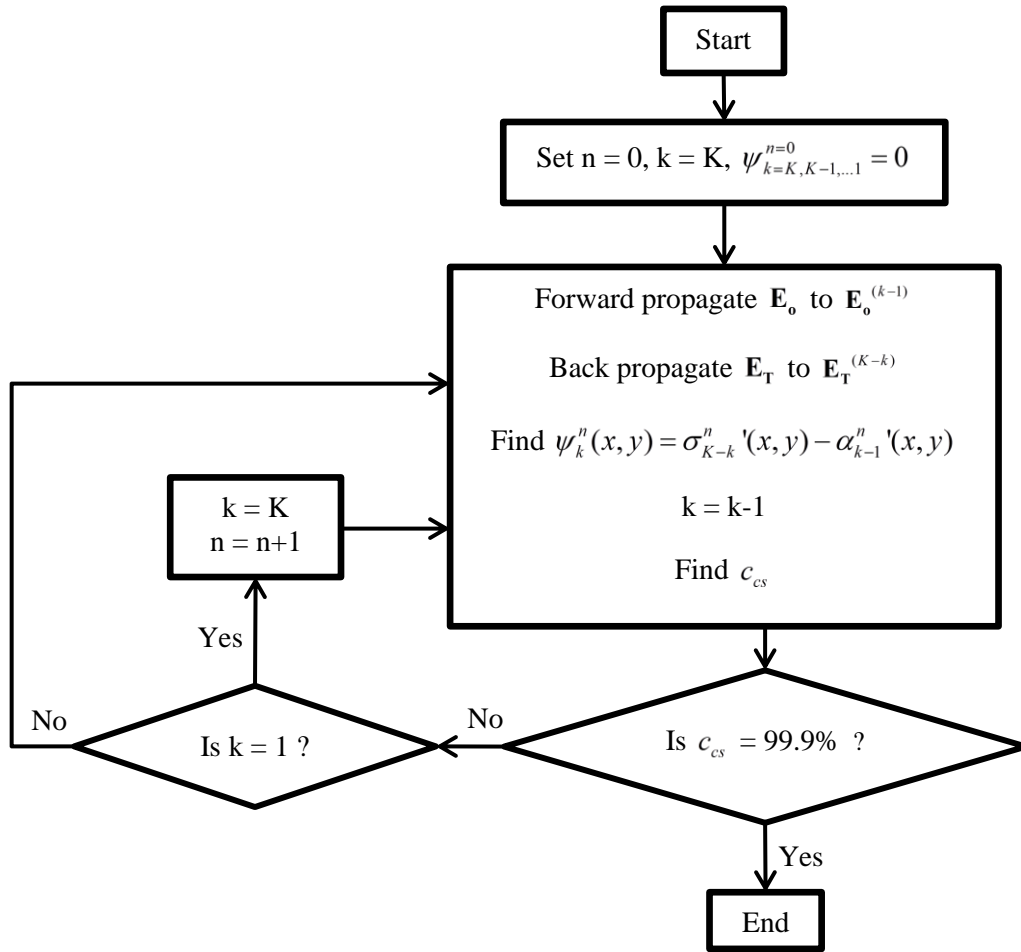
Is $c_{cs} = 99.9\%$?

Yes

Figure 3.3.2: Flowchart for the KS method for K phase correctors as described in Fig. 3.3.1

3.4 Two-Dimensional phase unwrapping

The phase (or argument), ϕ, of a function, $f(\mathbf{x})$, is defined mathematically as

$$\phi(\mathbf{x}) = \tan^{-1}\frac{\mathrm{Im}(f(\mathbf{x}))}{\mathrm{Re}(f(\mathbf{x}))}. \tag{3.4.1}$$

The problem with this definition is that the inverse tangent function is only defined in the $(-\pi, \pi]$ domain, therefore any ϕ values that exceed $\pm\pi$ will get wrapped (i.e. ϕ modulo 2π). For most applications the phase must be smooth in order to avoid discontinuities (i.e. the perturbations in a waveguide or on a mirror must be continuous). In one dimension, phase unwrapping is relatively simple to perform (assuming that there are no phase residues and the function is appropriately sampled) because it is path independent and the corrections to the discontinuities in the phase can be done locally. A simple formula for one-dimensional path integral phase unwrapping is

$$\phi(x) = \int_{x_o}^{x}\frac{\partial\theta(x)}{\partial x}\,dz + \theta(x_0), \tag{3.4.2}$$

where $\phi(x)$ is the unwrapped phase and ranges from $(-\infty, +\infty)$, $\theta(x)$ is the wrapped phase and is defined in the $(-\pi, \pi]$ region, and x_o is just an arbitrary reference point. Equation (3.4.2) is not helpful because it is for continuous functions and in practical phase unwrapping problems, the data is discrete. The discrete formulation equivalent of Eq. (3.4.2) for a discrete wrapped function, $\phi(n)$ (n = 0, 1, …, N) and a discrete unwrapped function, $\theta(n)$ is

$$\phi(n) = \theta(0) + \sum_{n=0}^{N-1}W\left(\Delta\{W[\theta(n)]\}\right), \tag{3.4.3}$$

where the difference operator, Δ is defined as $\Delta\{f(n)\} = f(n+1) - f(n)$ [38, p. 21]. The wrapping operator, W is defined as

$$W\{\phi(n)\} = \theta(n) + 2\pi k(n), \tag{3.4.4}$$

where the integer $k(n)$ is chosen so that $\theta(n)$ is always wrapped $(-\pi < \theta(n) \leq \pi)$. In words, Eq. (3.4.3) states that the unwrapped discrete phase is equivalent to integrating the wrapped phase differences of the wrapped phases.

For two dimensions, phase unwrapping can become much more complicated. Generalizing Eq. (3.4.2) into two dimensions results in

$$\phi(\mathbf{r}) = \int_C \nabla \theta(\mathbf{r}) \cdot d\mathbf{r} + \theta(\mathbf{r_o}), \tag{3.4.5}$$

where C is any path connecting points $\mathbf{r}$ to $\mathbf{r_o}$, and $\nabla \theta(\mathbf{r})$ is the phase gradient. Ideally, Eq. (3.4.5) is path independent only if there are no phase residues. There are numerous ways of solving two-dimensional phase unwrapping problems (that contain no phase residues), and the method used for this thesis is known as the unweighted least-squares approach using FFTs [38, pp. 184-198]. Utilizing this method, the phase corrections are done globally. An example of this method will be given by solving the following phase unwrapping problem. Figure 3.4.1 shows the amplitude and phase of a Gaussian beam with certain parameters, and the wrapped phase is now represented by the discrete function $f_{m,n} (0 \leq m \leq M, 0 \leq n \leq N)$ where m is the x index and n is the y index. The first step is to mirror-reflect and expand $f_{m,n}$ across the x and y axis, resulting in a new function of $F_{m,n} (0 \leq m \leq 2M, 0 \leq n \leq 2N)$, as shown in Fig. 3.4.2. Next the discrete two-dimensional Laplacian of $F_{m,n}$ is calculated (Fig. 3.4.2) using a three-point stencil as

$$\rho_{m,n} = (F_{m+1,n} - F_{m,n} + F_{m-1,n}) + (F_{m,n+1} - F_{m,n} + F_{m,n-1}). \tag{3.4.6}$$

The function $F_{m,n}$ is now a periodic function and it is the same as imposing Neumann boundary conditions on the original unexpanded $f_{m,n}$ function. The unwrapped function can be found from

$$\phi_{m,n} = IFFT \left(\frac{FFT(\rho_{m,n})}{2\cos\left(\dfrac{\pi m}{M}\right) + 2\cos\left(\dfrac{\pi n}{N}\right) - 4} \right), \tag{3.4.7}$$
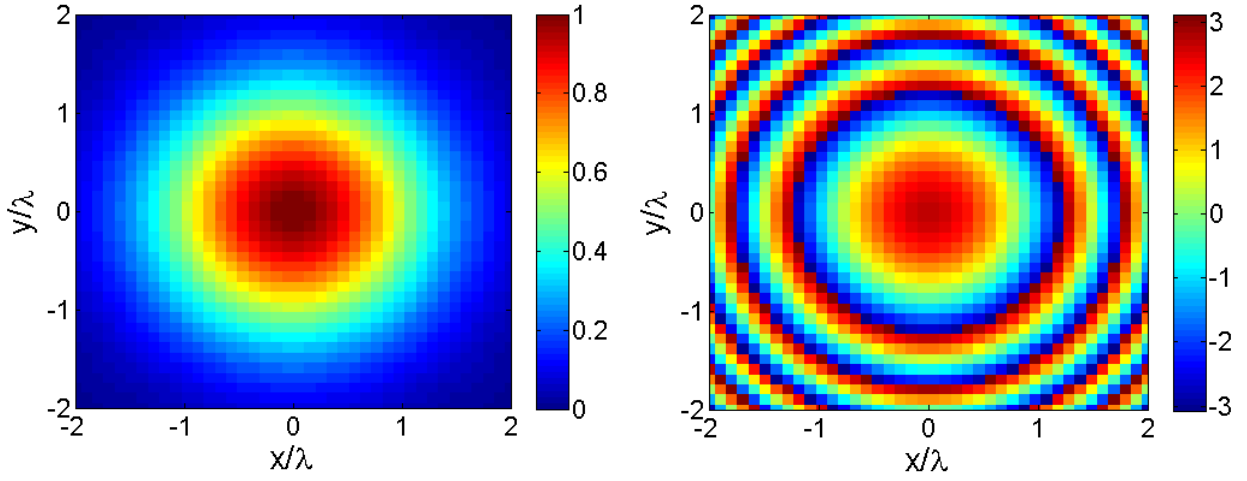
Figure 3.4.1: Amplitude (left) and wrapped phase in radians (right) of a planar cut of a Gaussian beam (f = 60 GHz and waists of 1 cm) 4 cm away from the waist. The sample size is 10 points/wavelength (N_λ = 10).

and the m and n indices should be reduced back to the original domain $(0 \leq m \leq M, 0 \leq n \leq N)$. The unwrapped phase solution to Fig. 3.4.1 is presented in Fig. 3.4.3. Because Eq. (3.4.5) is defined only up to an additive constant, the unwrapped solution from Eq. (3.4.5) can also be shifted by an arbitrary phase constant.
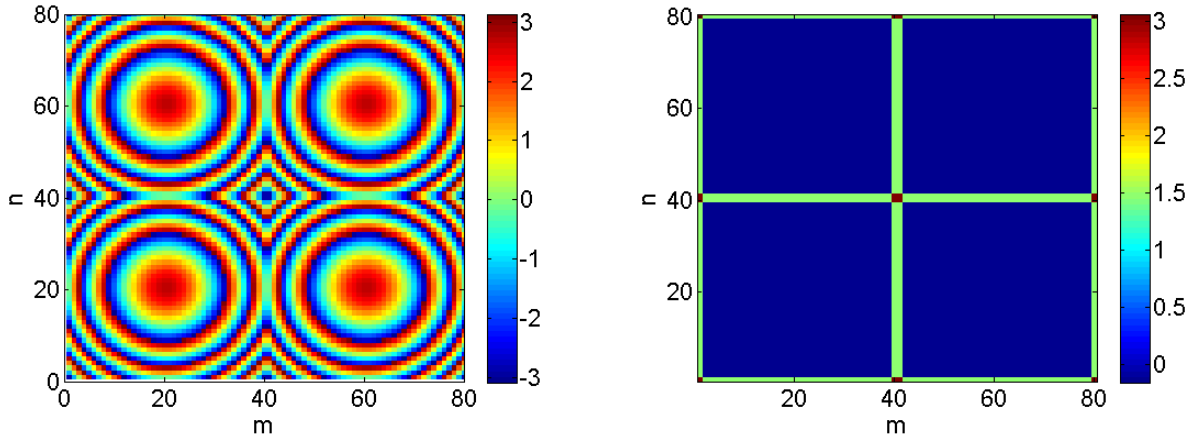

Figure 3.4.2: Mirror reflection of the wrapped phase in radians of Fig. 3.4.1 across the x and y-axis (left). The discrete two-dimensional Laplacian, $\rho_{m,n}$ (right). The new x and y-axis are now in terms of indices and are double in length.
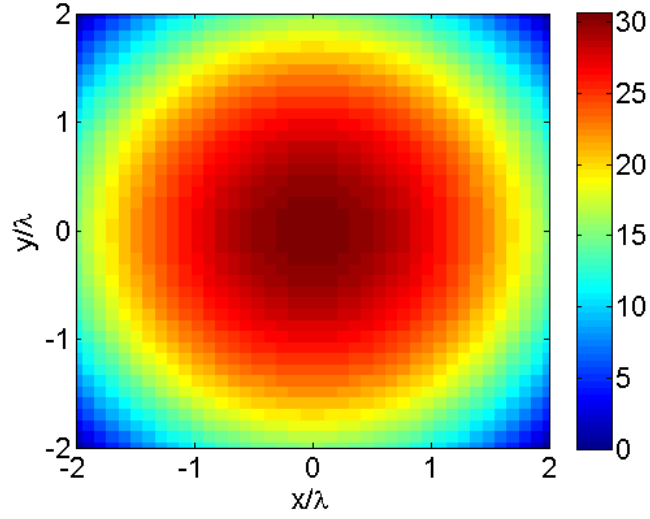
Figure 3.4.3: The unwrapped phase solution of Fig. 3.4.1 in radians.

3.5 Two-Dimensional phase unwrapping with phase residues

The main problem with two-dimensional phase unwrapping problems is that the phase information is almost always corrupted by phase residues. Phase residues can be thought of as phase inconsistencies caused by aliasing, numerical noise, shear or magnitude zeros [38]. The phase residue theorem (cf. residue theorem in complex analysis) states that [38, pp. 42-43]

$$\oint_C \nabla \theta(\mathbf{r}) \cdot d\mathbf{r} = 2\pi \times (\text{sum of phase residues encircled by C}), \tag{3.5.1}$$

and it is this condition that renders Eq. (3.4.5) path dependent. Phase residues can only take integer values, and are nearly always ± 1. The discrete formulation analogue for Eq. (3.5.1) is

$$\sum_m \sum_n \left[W\left(\theta_{m,n+1} - \theta_{m,n}\right) + W\left(\theta_{m+1,n+1} - \theta_{m,n+1}\right) + W\left(\theta_{m+1,n} - \theta_{m+1,n+1}\right) + W\left(\theta_{m,n} - \theta_{m+1,n}\right) \right] = 2\pi \sum q, \tag{3.5.2}$$

where q is the value of the phase residues. The notation presented in this section follows from the previous section.

The method used for this thesis in solving two-dimensional phase unwrapping problems that have phase residues is the preconditioned conjugate gradient (PCG) algorithm developed by Ghiglia and Pritt [38, pp. 223-225]. This PCG method minimizes the L^2-norm of the weighted difference between the unwrapped and wrapped phase gradients. For discrete data, this condition is expressed by

$$\varepsilon^2 = \sum_m \sum_n \left[u_{m,n} \left| \theta_{m+1,n} - \theta_{m,n} - W\left(\phi_{m+1,n} - \phi_{m,n} \right) \right|^2 + v_{m,n} \left| \theta_{m,n+1} - \theta_{m,n} - W\left(\phi_{m,n+1} - \phi_{m,n} \right) \right|^2 \right], \quad (3.5.3)$$

where $u_{m,n}$ and $v_{m,n}$ are the weights. When $u_{m,n} = v_{m,n} = 1$ (i.e. the unweighted case), then Eq. (3.5.3) reduces to the method described in the previous section. Similar to the previous section, an example of this method is presented by solving the following phase unwrapping problem. Figure 3.5.1 displays the amplitude of a Gaussian beam together with some generated phase residues only in the low-intensity regions (as expected from theory). The next step is to assign weights to minimize or exclude the contribution of the phase residues, and there are many ways of achieving this. For this research, binary weights will be employed; a minimum power threshold is set (-24 dB for this example), and all phase values below this threshold level is zero weighted. Figure 3.5.2 displays the weights used for this example. Different weighing schemes will produce different results, but there is a general guideline that can be followed to obtain the best unwrapped phase [14] [20] [38]. The PCG algorithm is then applied to find the unwrapped phase (due to the complexity of this algorithm, the details won't be discussed here). The method described in the previous section is used as the first initial guess in the PCG algorithm.
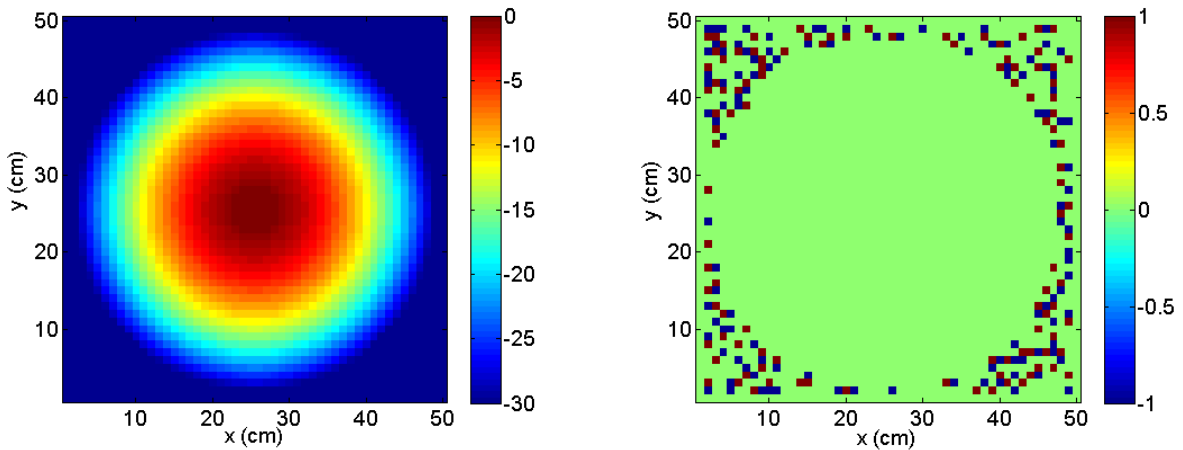

Figure 3.5.1: Amplitude (left) in dB and the phase residues (right) of a Gaussian beam on a planar cut.
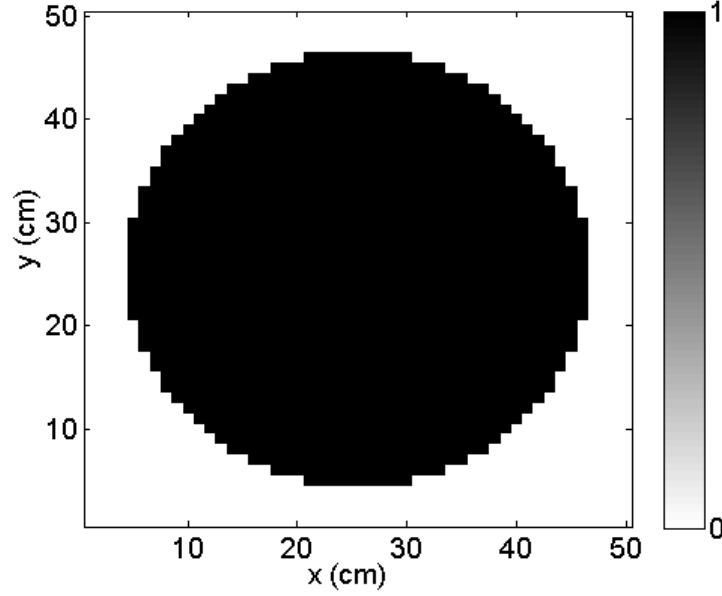
Figure 3.5.2: The two-dimensional binary weights used for this phase unwrapping example, with the minimum power threshold level set to -24 dB.

Because the PCG algorithm unwraps the phase globally, the unwrapped solution might not be congruent to the original wrapped phase, especially in the low intensity regions. Some researchers use the results from the PCG algorithm directly (without further processing), but this is not the approach taken in this thesis. The following equation is applied to the result of the PCG algorithm to enforce congruence

$$\tilde{\theta} = \theta + h + W(\phi - \theta - h), \qquad (3.5.4)$$

and

$$h = \frac{2\pi k}{N}, \qquad (3.5.5)$$

where $\tilde{\theta}$ is the congruent but discontinuous unwrapped phase, the integer k $(0 \leq k \leq N-1)$ is chosen to minimize the number of discontinuities in $\tilde{\theta}$, and N is an integer with usual values of 10 to 20. The downside of enforcing this congruence operation is that discontinuities are created to the unwrapped phase. To smooth the discontinuities,

the unwrapped phase is then low-pass filtered [17]. The final continuous and congruent unwrapped phase for the

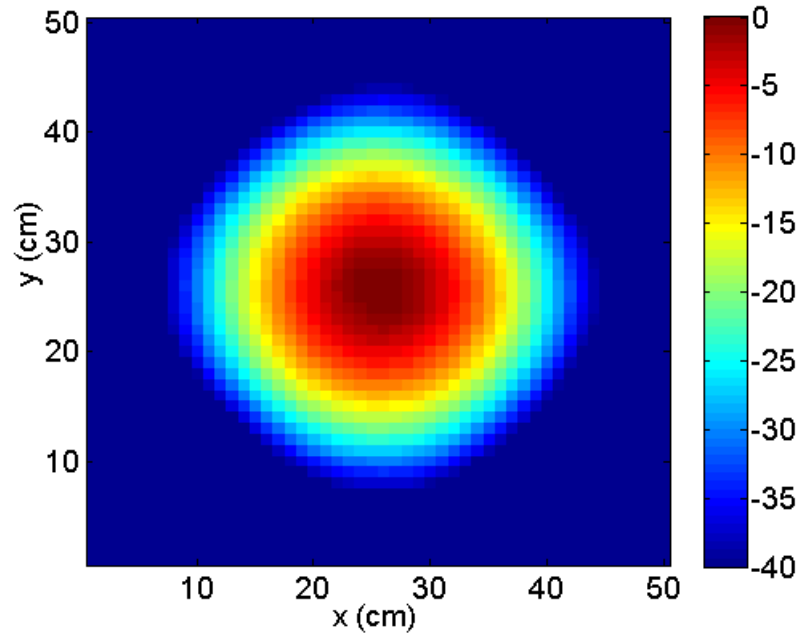example provided in this section is presented in Fig. 3.5.3.

Figure 3.5.3: The final unwrapped phase (in radians) of the phase unwrapping example from Fig. 3.5.1.

This method is relatively computationally intensive, and the time and resources required are roughly

proportional to the computational domain squared. Also, for best results, the numerous parameters must be

optimized. The phase unwrapping example provided here (a simple Gaussian beam on a planar cut) is simpler

compared to cases dealt with in the launcher design method (section 5.1). In the latter case, sometimes applying the

method in the previous section combined with low-pass filtering produces a better result than employing the PCG

method.

Chapter 4: The Iterative Stratton-Chu Method

Modeling and propagating fields in waveguides are critical in any launcher design. The most basic of all field propagation method is geometrical optics (GO), as described in Chapter 2. While GO provides an intuitive grasp of field propagation in waveguides and is simple and relatively fast to implement, it is not sufficiently sophisticated or accurate enough to design efficient launchers. At the other extreme end, the Method of Moments (MoM) technique provides for very accurate analysis of fields, however, it is relatively complicated to implement and very computationally intensive (takes up a lot of processing power and memory, and is very slow). Even by implementing the Multi-Level Fast Multipole Algorithm (MLFMA) to accelerate the MoM, the computation time is still inadequately fast. In this chapter, a few methods for propagating and modeling fields in waveguides are presented. These methods strike a fine balance between accuracy and speed, and are ideal for launcher design. All methods described here assume no ohmic losses.

4.1 Scalar waveguide field propagation methods

One way of modeling and propagating fields in waveguides is to think of it as a scattering problem. A starting incident field is defined as the source and the waveguide is treated as a metallic scatterer. In each propagation step, the starting incident field is scattered by the waveguide to produce a scattered field. This scattered field is equivalent to propagating the incident field by a certain distance in the waveguide. Next, the scattered field is added to the incident field and redefined as the new source field, and the source fields are scattered again repeatedly until the fields propagate throughout the entire section of the waveguide or until the fields converge. There are two main variants of this method; the first being called the Complement method by Chirkov *et al.* [21] and the second by Jin *et al.* [23]. Both methods are essentially the same, except with minor mathematical formulations differences. Chirkov *et al.* were the first to develop it, and Jin *et al.* modified it by implementing the method using FFTs. These methods only work for small perturbations and tapers.

Because H_z is the generating function of TE modes (TM modes are neglected), only the H_z field is represented and propagated (H_ρ and H_ϕ are neglected). This is most accurate for the case where the OF is small

(i.e. the launcher is operating close to cut off and H_z is the largest **H** field component). The H_z source field is defined on the walls of an unperturbed and untapered waveguide, and through multiple iterations, the H_z field is propagated throughout the waveguide. Chirkov *et al.* use the following Kirchoff-Huygens formulation

$$H_z^{i+1}(a,\phi,z) = \frac{\beta a}{2\pi j} \int_{-\infty}^{+\infty} \int_0^{2\pi} H_z^i(a,\phi',z')e^{j\Psi(\phi',z')}G(\phi,z)d\phi'dz', \tag{4.1.1}$$

while Jin *et al.* use a different formulation approximated from the scalar diffraction integral

$$H_z^{i+1}(a,\phi,z) = \int_{-\infty}^{+\infty} \int_0^{2\pi} H_z^i(a,\phi',z')e^{j\Psi(\phi',z')} \frac{\partial G(\phi,z)}{\partial n'} a d\phi'dz'. \tag{4.1.2}$$

Since all the fields are evaluated on the waveguide walls, the ρ variable is replaced with the guide radius, a. The iteration index is i, and the source fields are described by Eq. (2.1.1). The perturbations or phase corrections profile is represented by $\Psi(\phi',z')$, $G(\phi,z)$ is the Green's function, **n'** is the normal to the waveguide surface $(\mathbf{n'} = a\hat{\mathbf{\rho}})$ and the primes indicate the source location. The Green's function used is

$$G(\phi,z) = \frac{e^{-j\beta|\mathbf{R}|}}{4\pi|\mathbf{R}|}, \tag{4.1.3}$$

where |**R**| is the distance from the source to the observation point

$$|\mathbf{R}| = \sqrt{(x-x')^2 + (y-y')^2 + (z-z')^2}, \tag{4.1.4a}$$

and for cylindrical geometry,

$$|\mathbf{R}| = \sqrt{4a^2\sin^2\left(\frac{\phi-\phi'}{2}\right) + (z-z')^2}. \tag{4.1.4b}$$

The phase profile is defined as

$$\Psi(\phi',z') = \pm 2\beta\Delta\rho(\phi',z')\sin\theta_b, \tag{4.1.5}$$

and $\Delta\rho(\phi', z')$ is the perturbation profile and can be expressed as

$$\Delta\rho(\phi', z') = \sum_{p,q} \Delta\rho_{pq} \delta(\phi - \phi_x, z - z_y)$$

where $\delta(\phi - \phi_p, z - z_q) = 1$ for $\phi = \phi_p, z = z_q$ (4.1.6)

$$\delta(\phi - \phi_p, z - z_q) = 0 \text{ for } \phi \neq \phi_p, z \neq z_q.$$

It must be noted that all perturbations must be tapered at the start of the launcher to avoid discontinuities between the launcher and the source fields. The scalar diffraction integral states that

$$H_z(\mathbf{x}) = \iint_S H_z(\mathbf{x}') \frac{\partial G(\mathbf{x})}{\partial n} - G(\mathbf{x}) \frac{\partial H_z(\mathbf{x}')}{\partial n} dS,$$ (4.1.7)

and this equation reduces to Eq. (4.1.2) if the second term can be approximated as zero $\left(\frac{\partial H_z}{\partial n} = 0 \right)$, and this only

occurs when the perturbations are small $\left(|\Delta\rho| \ll a \right)$ and smooth $\left(\frac{\partial(\Delta R)}{\partial n'} \ll 1 \right)$.

The limits of $-\infty \leq z \leq \infty$ in Eqs. (4.1.1) and (4.1.2) must be reduced, and it is separated into two parts; the first part being the source $(-L_{source} \leq z \leq 0)$ and the second part is the launcher $(0 \leq z \leq L)$. Normally L_{source} is 3 or 4 times the launcher length (L) for the Chirkov method, and $L_{source} = 7L$ (depending on the number of iterations required) for Jin's method. Both integrals can be identified as convolution integrals and therefore its computation can be sped up using FFTs. Chirkov *et al.* numerically computes the convolution integral but Jin *et al.* employ FFTs. Numerically computing the integrals will take a relatively long time, but the source calculation needs only to be done once and can be reused in every subsequent iteration. The launcher parts however must be recalculated in each iteration. Implementing Eq. (4.1.2) by FFT results in

$$H_z^{i+1}(a, \phi, z) = IFFT\left(FFT(H_z^i(a, \phi', z')e^{j\Psi(\phi', z')}) \cdot FFT\left(\frac{\partial G(\phi, z)}{\partial n_o} \right) \right).$$ (4.1.8)

In both Eqs. (4.1.1) and (4.1.2) the iteration index must have a lower bound of $i \geq \left\lceil \dfrac{L}{L_b} \right\rceil$ so that the source field has

traversed the entire launcher length. For Eq. (4.1.2), the iteration index has a maximum bound of $i \leq \left\lfloor \dfrac{L_{source}}{L_b} \right\rfloor$

because of the way the source is defined. Both approaches of sourcing the integrals take up large amounts of

memory and a better way of doing it will be presented in section 4.4. Evaluating the Green's function of Eq. (4.1.3)

should be exercised with care so as to avoid the singularity when the source and observation point are at the same

location, i.e. $|\mathbf{R}| = 0$. Other Green's functions are also possible, as will be seen in the following sections. Although

TM fields are not covered in this section, the same analyses used for TE fields can be extended to TM fields.

An example of this propagation method for an untapered and perturbed TE$_{22,6}$ launcher is simulated using

Eq. (4.1.2) and the result is shown in Fig. 4.1.1. It is clear that the perturbation profile has bunched the initial

constant magnitude of the incident fields axially and azimuthally into a Gaussian shape beam by the end of the
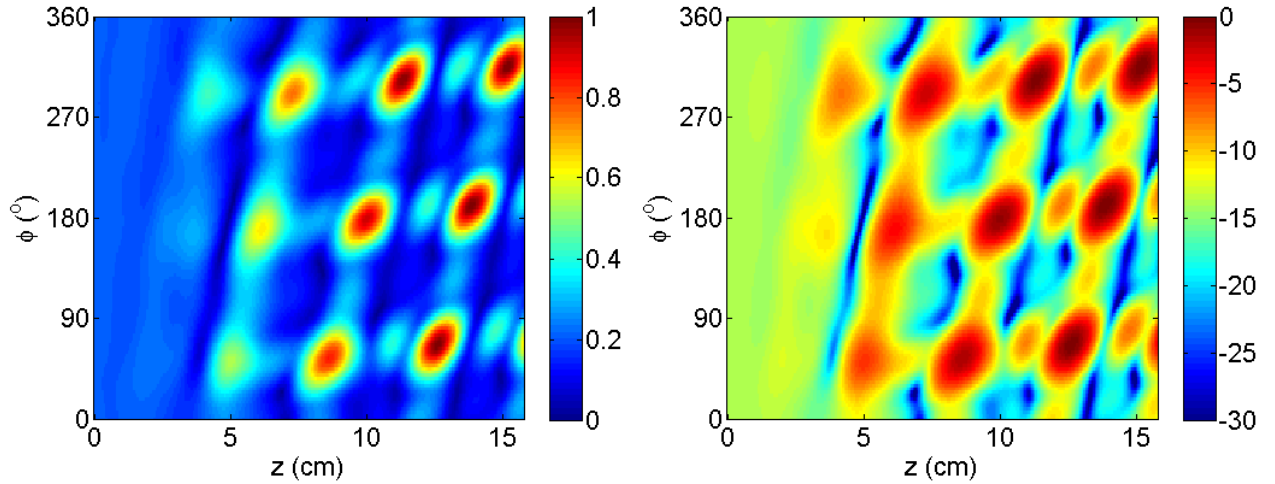
launcher.

Figure 4.1.1: The $\left| H_z \right|$ field for a TE$_{22,6}$ launcher with radius of 2.10 cm at 110 GHz, the linear scale is on the left and the log scale (in dB) is on the right.. The launcher length is 15 cm and the perturbation profile is $\Delta\rho(\phi, z) = a(\varepsilon \cos(\beta_1 z - 3\phi) + \varepsilon \cos(\beta_2 z - \phi)$ where a is the radius, $\varepsilon = 0.0019$, $\beta_1 = 0.168$ cm^{-1} and $\beta_2 = 1.68$ cm^{-1}. The launcher cut is not modeled here and the source field is not shown.

4.2 Theory of the Iterative Stratton-Chu method

The methods described in the previous section have been applied to model and design gyrotron launchers [21] [23] [27]. The main limitation with these scalar methods is their accuracy. In this section, a new method developed by Rock called the Iterative Stratton-Chu (ISC) method is introduced [20] [39] [40]. This method successively evaluates the field solutions to the Stratton-Chu vector diffraction integrals and the cylindrical harmonics equations for solving Maxwell's equations and boundary conditions on the waveguide. Table 4.1.1 summarizes the superiority and improvements of the ISC over the scalar methods and also serves as motivation for employing this method in gyrotron launcher design.

Table 4.1.1: Comparison between the ISC and Scalar Propagation Methods.

Iterative Stratton-Chu	Scalar propagation method
E and **H** fields (TE and TM modes)	Only H_z (or E_z) fields
Field evaluations anywhere	Field evaluation only on the waveguide walls
Perturbations modeled directly	Perturbations modeled indirectly -perturbations modeled as phase shifts projected on the smooth-wall waveguide
Accuracy competitive with Surf3d	Accuracy worsens as the launcher operates further from cutoff (i.e. high OF)
Incoming and outgoing waves are separable	Only the total fields can be modeled
Fast	Very fast (seconds to compute)

The derivation of the ISC starts with the Stratton-Chu vector diffraction integrals

$$\mathbf{H}(\mathbf{r}) = \int_{S} \frac{j\beta}{\eta}\left[\hat{\mathbf{n}} \times \mathbf{E}(\mathbf{r'})\right]G(\mathbf{r},\mathbf{r'}) + \left[\hat{\mathbf{n}} \cdot \mathbf{H}(\mathbf{r'})\right]\nabla'G(\mathbf{r},\mathbf{r'}) + \left[\hat{\mathbf{n}} \times \mathbf{H}(\mathbf{r'})\right] \times \nabla'G(\mathbf{r},\mathbf{r'})dS \qquad (4.2.1a)$$

$$\mathbf{E}(\mathbf{r}) = \int_{S} -j\beta\eta\left[\hat{\mathbf{n}} \times \mathbf{H}(\mathbf{r'})\right]G(\mathbf{r},\mathbf{r'}) + \left[\hat{\mathbf{n}} \cdot \mathbf{E}(\mathbf{r'})\right]\nabla'G(\mathbf{r},\mathbf{r'}) + \left[\hat{\mathbf{n}} \times \mathbf{E}(\mathbf{r'})\right] \times \nabla'G(\mathbf{r},\mathbf{r'})dS, \qquad (4.2.1b)$$

where **r** is the observation vector and **r'** is the source vector, the surface, S, is the inner surface of the circular waveguide, and the unit normal vector is $\hat{\mathbf{n}} = n_\rho \hat{\boldsymbol{\rho}} + n_\phi \hat{\boldsymbol{\phi}} + n_z \hat{\mathbf{z}}$. The waveguide walls are assumed to be perfect electrical conductors (pec) so the boundary conditions specify that $\hat{\mathbf{n}} \cdot \mathbf{H}(\mathbf{r'}) = 0$ and $\hat{\mathbf{n}} \times \mathbf{E}(\mathbf{r'}) = 0$. The free-space Green's function used is

$$G(\mathbf{r},\mathbf{r'}) = \frac{j}{8\pi} \int_{-\infty}^{\infty} \sum_{m=-\infty}^{\infty} J_m(\beta_\rho \rho) H_m^{(2)}(\beta_\rho \rho') e^{-jm(\phi-\phi')} e^{-j\beta_z(z-z')} d\beta_z \text{ for } \rho < \rho'$$

$$G(\mathbf{r},\mathbf{r'}) = \frac{j}{8\pi} \int_{-\infty}^{\infty} \sum_{m=-\infty}^{\infty} J_m(\beta_\rho \rho') H_m^{(2)}(\beta_\rho \rho) e^{-jm(\phi-\phi')} e^{-j\beta_z(z-z')} d\beta_z \text{ for } \rho > \rho' \qquad (4.2.2)$$

and more about this function will be covered in the next section. The fields inside a circular waveguide can also be expressed via cylindrical harmonics [41]

$$\mathbf{H}(\mathbf{r}) = \frac{j}{2\pi\eta} \int_{-\infty}^{\infty} \sum_{m=-\infty}^{\infty} \left(b_m(\beta_z) \mathbf{M}_m(\mathbf{r},\beta_z) + a_m(\beta_z) \mathbf{N}_m(\mathbf{r},\beta_z) \right) d\beta_z \qquad (4.2.3a)$$

$$\mathbf{E}(\mathbf{r}) = \frac{1}{2\pi} \int_{-\infty}^{\infty} \sum_{m=-\infty}^{\infty} \left(a_m(\beta_z) \mathbf{M}_m(\mathbf{r},\beta_z) + b_m(\beta_z) \mathbf{N}_m(\mathbf{r},\beta_z) \right) d\beta_z, \qquad (4.2.3b)$$

where

$$\mathbf{M}_m(\mathbf{r},\beta_z) = \left(\frac{-jm}{\rho} J_m(\beta_\rho \rho) \hat{\boldsymbol{\rho}} - \frac{\partial J_m(\beta_\rho \rho)}{\partial \rho} \hat{\boldsymbol{\phi}} \right) e^{-jm\phi} e^{-j\beta_z z} \qquad (4.2.3c)$$

$$\mathbf{N}_m(\mathbf{r},\beta_z) = \left(\frac{-j\beta_z}{\beta} \frac{\partial J_m(\beta_\rho \rho)}{\partial \rho} \hat{\boldsymbol{\rho}} - \frac{m\beta_z}{\beta\rho} J_m(\beta_\rho \rho) \hat{\boldsymbol{\phi}} + \frac{\beta_z^2}{\beta} J_m(\beta_\rho \rho) \hat{\mathbf{z}} \right) e^{-jm\phi} e^{-j\beta_z z}. \qquad (4.2.3d)$$

The cylindrical harmonics formulation in Eqs. (4.2.3a) to (4.2.3d) assumes no TM to TE coupling (and vice versa). This assumption results in the decoupling of Eqs. (4.2.1a) and (4.2.1b). In well-designed launchers, there should be negligible to minimal modal coupling. Also, Rock argues that coupling between TE and TM modes is small when

the launcher is operating close to cut off and when the perturbations are small to moderate in size [20]. The TE modes are signified by $a_m(\beta_z)$ and the TM modes by $b_m(\beta_z)$. A physical interpretation of the coefficients $a_m(\beta_z)$ and $b_m(\beta_z)$ are as the cylindrical spectra of the respective modes. For TE modes only $(b_m(\beta_z) = 0)$, equating Eq. (4.2.1a) and Eq. (4.2.3a) (and after some algebraic rearrangements) yields

$$H_z(\mathbf{r}) = \frac{j}{2\pi\eta} \int_{-\infty}^{\infty} \sum_{m=-\infty}^{\infty} a_m(\beta_z) \left(\frac{\beta_z^2}{\beta} \right) J_m(\beta_\rho\rho) e^{-jm\phi} e^{-j\beta_z z} d\beta_z \tag{4.2.4a}$$

$$H_\phi(\mathbf{r}) = \frac{j}{2\pi\eta} \int_{-\infty}^{\infty} \sum_{m=-\infty}^{\infty} a_m(\beta_z) \left(\frac{-m\beta_z}{\beta\rho} \right) J_m(\beta_\rho\rho) e^{-jm\phi} e^{-j\beta_z z} d\beta_z \tag{4.2.4b}$$

$$H_\rho(\mathbf{r}) = \frac{j}{2\pi\eta} \int_{-\infty}^{\infty} \sum_{m=-\infty}^{\infty} a_m(\beta_z) \left(\frac{-j\beta_z}{\beta} \right) \frac{\partial J_m(\beta_\rho\rho)}{\partial\rho} e^{-jm\phi} e^{-j\beta_z z} d\beta_z \tag{4.2.4c}$$

$$E_\phi(\mathbf{r}) = \frac{1}{2\pi} \int_{-\infty}^{\infty} \sum_{m=-\infty}^{\infty} a_m(\beta_z)(-1) \frac{\partial J_m(\beta_\rho\rho)}{\partial\rho} e^{-jm\phi} e^{-j\beta_z z} d\beta_z \tag{4.2.4d}$$

$$E_\rho(\mathbf{r}) = \frac{1}{2\pi} \int_{-\infty}^{\infty} \sum_{m=-\infty}^{\infty} a_m(\beta_z) \left(\frac{-jm}{\rho} \right) J_m(\beta_\rho\rho) e^{-jm\phi} e^{-j\beta_z z} d\beta_z \tag{4.2.4e}$$

where

$$a_m(\beta_z) = \frac{\beta\eta}{4\beta_\rho^2} \left(jm A_m(\beta_z) + B_m(\beta_z) \right) \tag{4.2.4f}$$

and

$$A_m(\beta_z) = \int_{-\infty}^{\infty} \int_0^{2\pi} \frac{\left(n_\phi H_z - n_z H_\phi \right)}{|n_\rho|} H_m^{(2)}(\beta_\rho\rho') e^{jm\phi'} e^{j\beta_z z'} d\phi' dz' \tag{4.2.4g}$$

$$B_m(\beta_z) = \int_{-\infty}^{\infty} \int_0^{2\pi} \frac{\rho'\left(n_\rho H_z - n_z H_\rho \right)}{|n_\rho|} \frac{\partial H_m^{(2)}(\beta_\rho\rho')}{\partial\rho'} e^{jm\phi'} e^{j\beta_z z'} d\phi' dz'. \tag{4.2.4h}$$

For TM modes $(a_m(\beta_z) = 0)$, equating Eq. (4.2.1b) and Eq. (4.2.3b) (and after some algebraic manipulations) gives

$$E_z(\mathbf{r}) = \frac{j}{2\pi\eta} \int\limits_{-\infty}^{\infty} \sum\limits_{m=-\infty}^{\infty} b_m(\beta_z) \left(\frac{\beta_z^2}{\beta}\right) J_m(\beta_\rho\rho) e^{-jm\phi} e^{-j\beta_z z} d\beta_z \qquad (4.2.5a)$$

where

$$b_m(\beta_z) = \frac{\beta}{4\beta_\rho^2} \left(\beta\eta C_m(\beta_z) + D_m(\beta_z)\right) \qquad (4.2.5b)$$

and

$$C_m(\beta_z) = \int\limits_{-\infty}^{\infty} \int\limits_{0}^{2\pi} \frac{\rho'\left(n_\rho H_\phi - n_\phi H_\rho\right)}{|n_\rho|} H_m^{(2)}(\beta_\rho\rho') e^{jm\phi'} e^{j\beta_z z'} d\phi' dz' \qquad (4.2.5c)$$

$$D_m(\beta_z) = \int\limits_{-\infty}^{\infty} \int\limits_{0}^{2\pi} \frac{\rho'\left(n_\rho E_\rho + n_\phi E_\phi + n_z E_z\right)}{|n_\rho|} H_m^{(2)}(\beta_\rho\rho') e^{jm\phi'} e^{j\beta_z z'} d\phi' dz'. \qquad (4.2.5d)$$

Figure (4.2.1) summarizes the equations described in this section. Starting off with an initial guess (could be initial fields [i.e. $\mathbf{E_o}(\mathbf{r})$ or $\mathbf{H_o}(\mathbf{r})$] or initial cylindrical spectrum [i.e. $a_{m_o}(\beta_z)$ or $b_{m_o}(\beta_z)$]), the final solution is built by successively approximating the fields and cylindrical spectrum in each iteration. The number of iterations needed for convergence depends on the initial guess and the perturbations. The closer the initial guess is to the final solution, the fewer iterations are needed. Similarly, the smaller the perturbation size or the less rapid/oscillatory the perturbations are, the fewer iterations are needed. For an unperturbed and untapered waveguide, only one iteration per Brillouin zone is needed to achieve convergence. As stated in Eqs. (4.2.4g) and (4.2.4h), not all fields can be used as the initial starting guess. For example, in an untapered and unperturbed waveguide ($n_\phi = n_z = 0$ and $n_\rho = 1$), injecting either H_ϕ and/or H_ρ as the initial guess will only converge to field solutions and a cylindrical spectrum of zero. In this research, the initial starting guess is always the H_z field of an unperturbed waveguide. Rock has proven that the ISC formulation can be reduced to the scalar propagation methods [20].
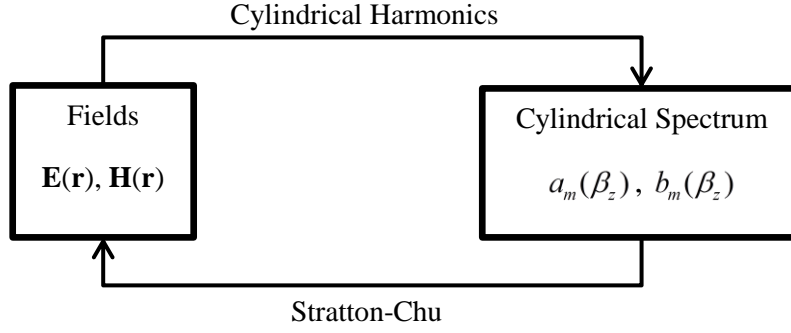
Figure 4.2.1: Diagram illustrating the successive approximations method for finding the converged fields and cylindrical spectrum.

4.3 The Green's function used in the ISC

Green's functions can be expressed in several ways, however, some converge faster than others. The Green's function used in the ISC method in Eq. (4.2.2) is one of the ways of expressing the Green's function for a cylindrical coordinate system. The latter Green's function is better because, 1) there is no singularity when the observation and source points coincide, 2) it can be expanded in terms of infinitesimals of the radius, i.e. $\Delta\rho$, and 3) it is defined in the spectral domain (vs. the spatial domain for the former). The second reason allows for modeling the perturbations in terms of FFTs (more on this in the next section) and the third reason lets the FFT implementation of the convolution integral to be done with one less FFT step. For example in the scalar propagation method, Eq. (4.1.2) can be rewritten as

$$H_z^{i+1}(a,\phi,z) = \int_{-\infty}^{\infty} \sum_{m=-\infty}^{\infty} J_m(\beta_\rho\rho) \frac{\partial H_m^{(2)}(\beta_\rho\rho')}{\partial\rho'} \left(\int_{-\infty}^{+\infty} \int_0^{2\pi} H_z^i(a,\phi',z') e^{j\Psi(\phi',z')} e^{jm\phi'} e^{j\beta_z z'} \rho'd\phi'dz' \right) \\ \cdot e^{-jm\phi} e^{-j\beta_z z} d\beta_z, \quad (4.3.1)$$

where $H_m^{(2)}(\beta_\rho\rho')$ can be pulled out from the source integral because it is not a function of ϕ' and z'. Carrying out Eq. (4.2.6) by FFT returns

$$H_z^{i+1}(a,\phi,z) = FFT\left[J_m(\beta_\rho\rho)\frac{\partial H_m^{(2)}(\beta_\rho\rho')}{\partial\rho'} \cdot IFFT(H_z^{i}(a,\phi',z')e^{j\Psi(\phi',z')}) \right]. \qquad (4.3.2)$$
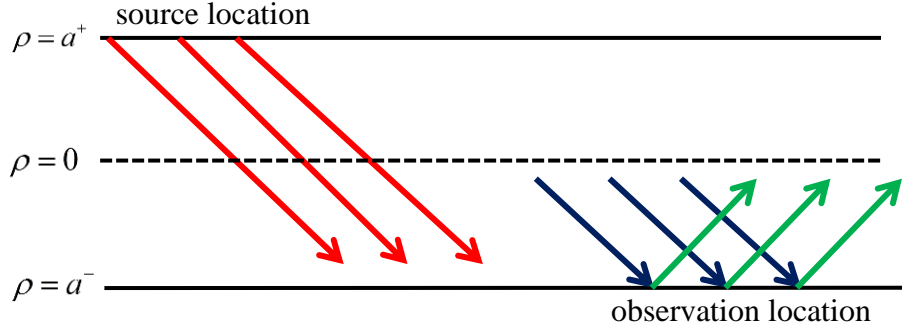

Figure 4.3.1: Diagram of a Geometrical Optics representation of the cylindrical harmonics Green's function of Eq. (4.2.2) for $\rho < \rho'$. The red arrows represent the outgoing fields from the source (i.e. $H_m^{(2)}(\beta_\rho\rho')$), the green arrows (i.e. $H_m^{(1)}(\beta_\rho\rho)$) and blue arrows (i.e. $H_m^{(2)}(\beta_\rho\rho)$) are correspondingly the incoming fields and the outgoing fields at the observation point. The sum of the incoming and outgoing fields at the observation point gives the total fields (i.e. $J_m(\beta_\rho\rho)$). Although the source and observation location are shown to be separated, they do not have to be so.

A pictorial description of this Green's function for $\rho < \rho'$ is represented in Fig. 4.3.1. The outgoing fields

from the source are propagated to the observation point and these fields undergo a phase shift of $e^{-jm(\phi-\phi')}$ in the ϕ

direction and $e^{-j\beta_z(z-z')}$ in the **z** direction. To get the total fields at the observation point, these individual fields are

summed up over all propagating wave vectors, β_z and modes, m. Replacing $J_m(\beta_\rho\rho)$ in Eq. (4.2.2) by $H_m^{(1)}(\beta_\rho\rho)$

and $H_m^{(2)}(\beta_\rho\rho)$ respectively gives the incoming and outgoing field portions at the observation point. For $\rho > \rho'$,

the total fields from the source is propagated to the observation point, and only the outgoing fields at the observation

point is summed up over all propagating wave vectors. For $\rho = \rho'$, either of these two forms of the Green's
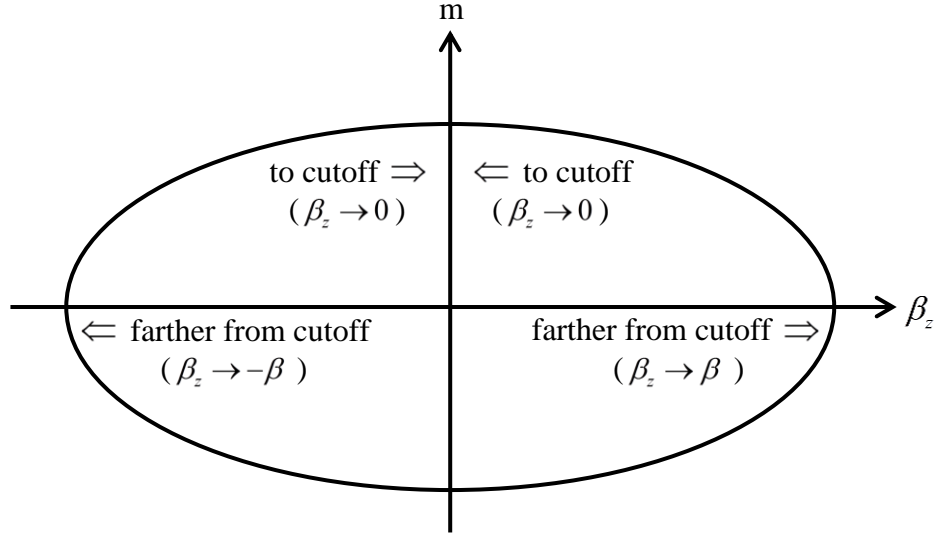
function is applicable.

Figure 4.3.2: The domain of the cylindrical harmonics Green's function of Eq. (4.2.2) in the cylindrical spectrum. The right side plane represents fields propagating in the +**z** direction, and the left side plane is for fields propagating in the −**z** direction. The upper plane represents the rotating mode in the CCW direction $(e^{-jm\phi})$, and the lower plane is for counter-rotating modes in the CCW direction $(e^{+jm\phi})$. Note: the y-axis is discrete and the x-axis is continuous.

Special consideration must be taken when evaluating the Green's Function because it is only well defined in a certain region of the cylindrical spectrum, as displayed in Fig. 4.3.2. To avoid the Green's function from blowing up to infinity, β_z must be purely real and nonzero, i.e. evanescent fields are not considered. All of the TE modes (and/or TM modes) above cutoff must be excluded from the computational domain. For example, in the TE$_{02}$ mode waveguide of Table 2.2.1, only modes TE$_{11}$ to TE$_{54}$ (TM modes are excluded) should be included. These restrictions are expressed mathematically as $\mathrm{Im}(\beta_z) = 0$ and $|m| \leq \sqrt{\beta^2 - \beta_z^2}\, a$ (the latter equation is necessary because not all modes of an azimuthal index propagates, e.g. from the previous example, TE$_{15,1}$ propagates but not TE$_{15,2}$). Correspondingly, only a portion of cylindrical spectrum needs to be evaluated, and it is called the spectral mask [26] (or transfer function [20]). At most, the spectral mask is elliptically-shaped (Fig. 4.3.2), but depending on the perturbations and launcher design, this spectral mask can be shrunk to reduce the computation time and resources.

4.4 Efficient implementation of the ISC

There are numerous methods that can be employed to further reduce the time and computational evaluation of the ISC integrals. The first is by truncating the z limits in the source domain. Depending on the application, L_{source} can be reduced to L or 2L. In each iteration the source fields are redefined; the amplitude and phase of the source fields are stitched to the amplitude and phase of the launcher fields so that there are no discontinuities at the source and launcher interface at z = 0. This extra computation step per iteration enables the computational domain to be lessened by at least a factor of two (sometimes even up to a factor of 4) compared to the methods used by scalar field propagation methods. For back propagation, the same method is utilized although the requirements can be relaxed. For example, the target function for back propagation is usually a fundamental mode Gaussian beam (where the field magnitude is nearly zero at the launcher and source interface) so the source and launcher fields do not have to be stitched. Therefore in back propagation, it is only necessary to multiply the target function with a constant phase shift per iteration, so that the back propagated target function adds up correctly between successive iterations.

A windowing function is defined in the z direction only to reduce the Gibbs ringing of the fields at the start and end of the entire computational domain. The windowing function should be flat throughout the domain and then drops smoothly to zero at the edges. For this research, the form of the windowing function used is

$$w(z) = \exp\left\{-\left[\kappa\left(\frac{z}{L_{tot}} - \frac{1}{2}\right)\right]^{2N}\right\}$$

(4.4.1)

where L_{tot} is the total length in z, κ is a positive variable and N is a positive integer. The higher the value of N, the flatter the function becomes and the faster it drops to zero at the edges. As N approaches infinity, the window function becomes a square function. Examples of window functions and their spectra are shown in Fig. 4.4.1. The ideal window function is a constant window of infinite length and its spectrum is a delta function, however, practical window functions have spectrums of finite widths. Multiplication of the fields and the window function is equivalent to convolving the spectrum of the fields (the cylindrical spectrum) and the spectrum of the window function. A delta function spectrum picks out the peaks of the spectrum of the fields without interfering, mixing or smearing the

different peaks. Having a window function spectrum with finite widths spreads the peaks of the field spectrum (especially peaks that are very close to each other) and can lead to distortion in the spectrum and potentially the wrong field solutions. This effect is a necessary sacrifice and can be mitigated by choosing the right window function. As illustrated by the spectrum in Fig. 4.4.1, the upper part of the spectrum is a very good approximation to a delta function, however, the lower part spreads the spectrum by a moderate amount. Because the lower part of the spectrum is in the -15 dB and lower range, the spectrum spreading is attenuated and is not a concern. In some cases (e.g. when the peaks of the field spectrum are comparable in magnitude to one another, and they are very closely situated) this form of window function will not work.
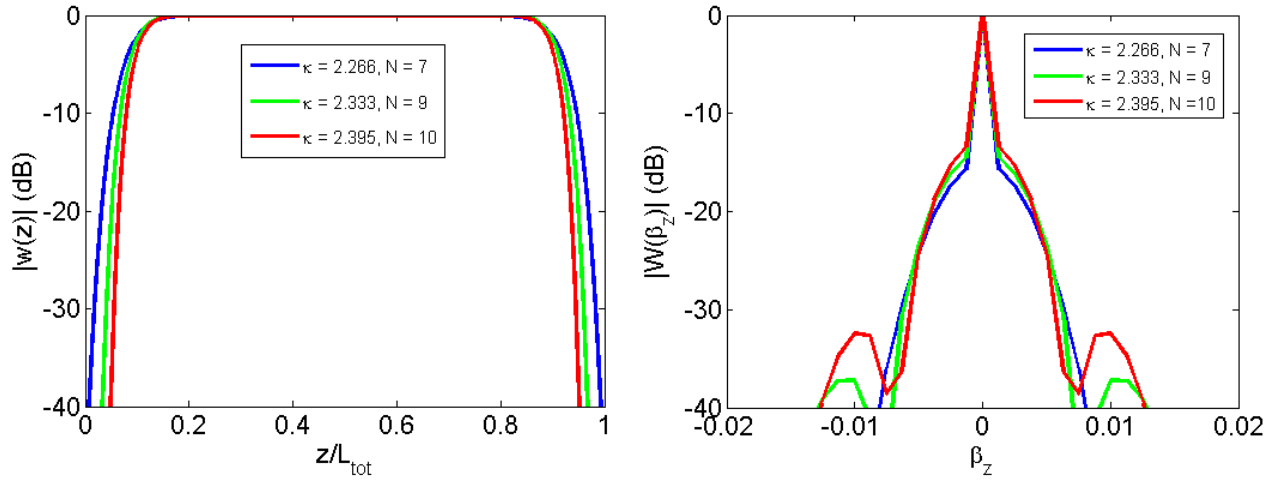

Figure 4.4.1: Example of window functions (left) and their spectrum (right) for different κ and N values.

The beauty of the ISC is that it can implemented using FFTs. Following the TIFFT method developed by Liao [19], the radial term can be expanded in terms of a Taylor series. The accuracy of the series expansion can be increased by using multiple expansion points. Rewriting the spectrum components in Eqs. (4.2.4g) and (4.2.4h) in a Taylor series expansion gives

$$A_m(\beta_z) = \sum_{k=0}^{K} \frac{\beta_\rho^{\ k}}{k!} H_m^{(2)}(\beta_\rho \rho_o)^{(k)} \int_{-\infty}^{\infty} \int_{0}^{2\pi} \frac{\left(n_\phi H_z - n_z H_\phi\right)}{|n_\rho|} (\rho'-\rho_o)^k e^{jm\phi'} e^{j\beta_z z'} d\phi' dz' \qquad (4.4.2a)$$

$$B_m(\beta_z) = \sum_{k=0}^{K} \frac{\beta_\rho^{k+1}}{k!} H_m^{(2)}(\beta_\rho \rho_o)^{(k+1)} \int_{-\infty}^{\infty} \int_0^{2\pi} \frac{\rho'(n_\rho H_z - n_z H_\rho)}{|n_\rho|} (\rho' - \rho_o)^k e^{jm\phi'} e^{j\beta_z z'} d\phi' dz'. \qquad (4.4.2b)$$

The same method can be extended to the fields, for example the H_z component of Eq. (4.2.4a) can be rewritten as

$$H_z(\mathbf{r}) = \frac{j}{2\pi\eta\beta} \sum_{s=0}^{S} \sum_{k=0}^{K} \frac{(\rho - \rho_s)^k}{k!} \int_{-\infty}^{\infty} \sum_{m=-\infty}^{\infty} a_m(\beta_z) \beta_z^{k+2} J_m(\beta_\rho \rho_s)^{(k)} e^{-jm\phi} e^{-j\beta_z z} d\beta_z. \qquad (4.4.3)$$

The rest of the field expressions will not be shown. The k variable represents the number of terms in the Taylor series expansion, and the s parameter indicates the number of expansion points in ρ used. The k superscript indicates derivative of the kth order (e.g. $H_m^{(2)}(\beta_\rho \rho_o)^{(k)} = \frac{\partial^{(k)}}{\partial(\beta_\rho \rho_o)^{(k)}} H_m^{(2)}(\beta_\rho \rho_o)$). Note that the spectral components in Eqs. (4.4.2a) and (4.4.2b) can only have one expansion point in the radial direction, ρ_o, because ρ_o is part of the integrand. The field equations (such as Eq. (4.4.3)) can be expanded into multiple expansion points because the ρ_s terms can be pulled out of the integrand. To get more accurate fields solutions, the number of Taylor terms required, K, and the number of radial expansion points, S, should be increased. The most computationally expensive part of the ISC is the Bessel function evaluation in the Green's function, however, this computation needs to be only done once at the start, and other Bessel functions identities (e.g. Eq. (2.2.1)) can be exploited to reduce the number of Bessel function evaluations.

The field components from the ISC implementation of the $TE_{22,6}$ launcher described in Fig. 4.1.1 is presented in Fig. 4.4.2. As expected, multiple iterations of the windowing function have broadened the spectral widths of the TE modes. By design, this perturbation profile converts the $TE_{22,6}$ main mode into 4 adjacent satellite modes which are $TE_{25,5}$, $TE_{19,7}$, $TE_{21,6}$ and $TE_{23,6}$, and together all these 5 modes give a Gaussian shaped field on the output Brillouin zone (i.e. output aperture). The rest of the modes ($TE_{26,5}$, $TE_{20,7}$, $TE_{24,5}$ and $TE_{18,7}$) are parasitic modes; these modes are inevitable byproducts of the perturbation profile and they reduce the Gaussian profile of the output radiation.
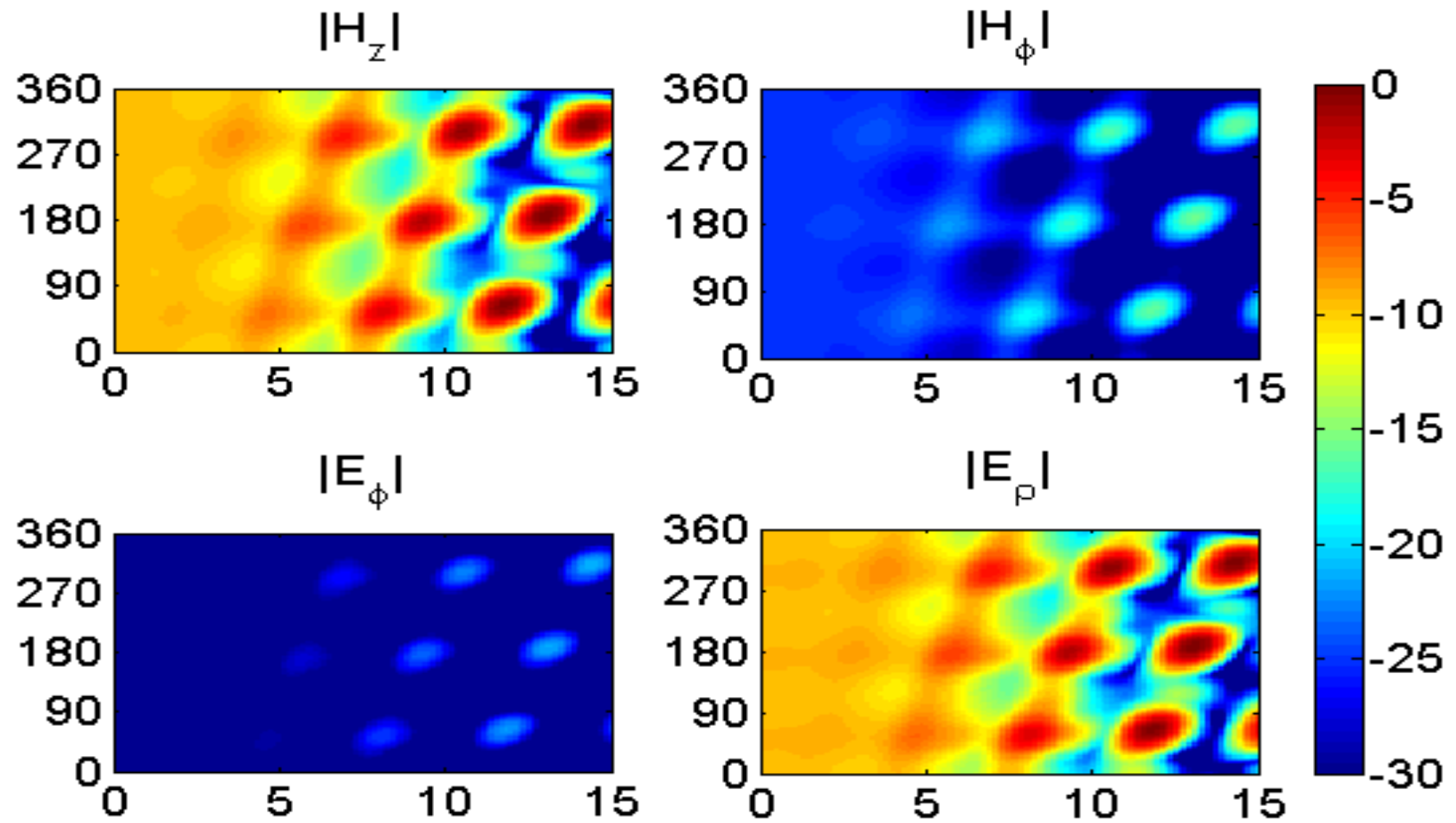
Figure 4.4.2: Field components of the TE$_{22,6}$ launcher (as described in Fig 4.1.1) obtained from the ISC method in log scale (dB). The launcher cut is not modeled here and the source fields are not shown. The $\left|H_\rho\right|$ and $\left|E_z\right|$ fields are not shown because they are smaller than -30 dB.
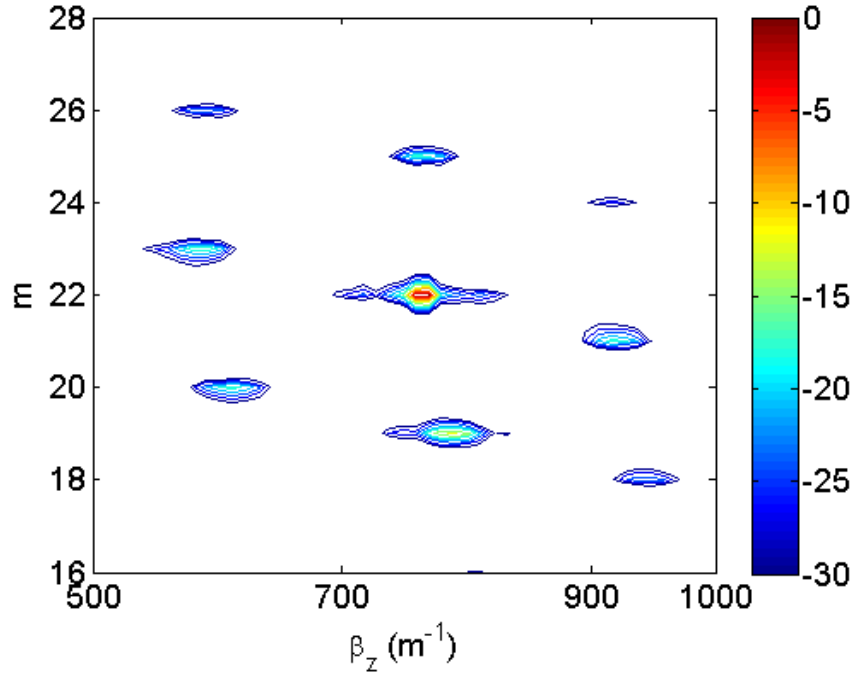
Figure 4.4.3: Contour Plots of the TE mode cylindrical spectrum, $|a_m(\beta_z)|$ of the TE$_{22,6}$ launcher (in dB) obtained from the ISC method.

Note that only the first order satellite and parasitic modes are shown as higher order modes are neglected because they are small (less than 30 dB). For this perturbation profile, only a square shaped spectral mask is required. Comparing the H_z components shows that both propagation methods (Fig. 4.1.1 vs. Fig. 4.4.2a) give slightly different results (especially in the number and magnitude of the side lobes), with the ISC giving the more accurate solution (more complete and rigorous analyses between these two methods are presented by Rock [20]).

Chapter 5: The Launcher Design Method

5.1 The launcher design method and algorithm

Figure 5.1.1 is a generic picture of a TE_{0n} launcher and the coordinate system that will be used throughout this thesis.
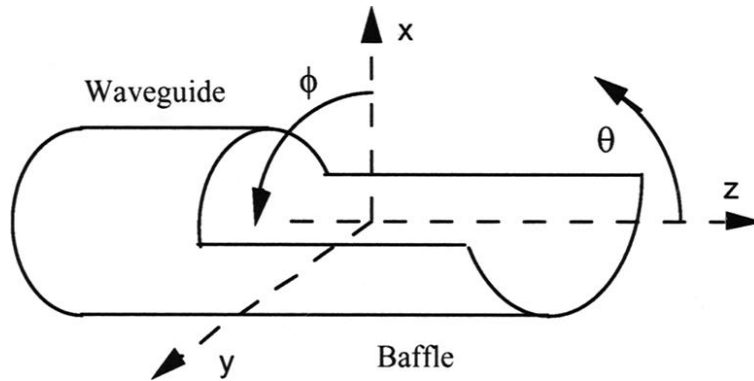

Figure 5.1.1: Generic picture of a TE_{0n} launcher with the corresponding coordinate system [42].

The objective of this launcher design method is to improve the radiation pattern of launchers (see Chapter 6) by adding perturbations to the launchers. The desired perturbed-wall launcher output radiation should be a linearly-polarized and collimated Gaussian beam (that can be fully captured by a simple system of mirrors) with minimal or no side lobes. The perturbations must be modest in size and smooth so that they are machinable and do not cause significant reflections. Additionally, it is also required that the cross-polarization remains negligible. Although it is highly desirable for the launcher output radiation to be a circular Gaussian beam, it is not a main requirement as an elliptical beam is easier and more efficiently corrected by a mirror system. An equally essential criterion is for reflections in the launcher to be small; however, no such quantification of this criterion will be attempted. The rigorous and analytical way of calculating reflections in waveguides is by the coupled-mode method, and this method is beyond the scope of this thesis. Nevertheless it can be qualitatively argued that by minimizing the edge diffraction losses (i.e. reducing the magnitude of the fields at the launcher edges), reflections at the launcher and air interface are also reduced. It can also be reasoned that having small, smooth and slowly varying perturbations will also decrease the amount of mode reflections inside the launcher.

This launcher design method is built on previous work [42]-[44]. Li first tried improving the output radiation pattern by using analytical type perturbations (e.g. a convex perturbation on the waveguide and a concave perturbation on the baffle) [42]. The results were an improvement but the output radiation was still not acceptable. Next Denisov *et al.* applied the Complement method (section 4.1) for a launcher with an OF of 1.38, and claims to have achieved a very high Gaussian beam output [27]. However this method does not work well for launchers with high OFs [43], such as this case. In this section, a new method will be presented.

The method and algorithm presented here are based on the theories and methods of previous chapters. In general, the Brillouin zones of the launcher will be treated as distinct mirror surfaces (from GO), and a K-S based mirror design algorithm will be used to shape the perturbations on each zone. Unlike previous launcher design methods [21] [23] [43], the ISC method will be used to propagate and model the fields in the launcher. All of these theories and methods are then combined and harmonized to produce the launcher design method. The complete flowchart of this method is presented in Fig. 5.1.2.

The launcher design method starts with defining and numbering the Brillouin zones on the launcher (based on the launcher length, frequency and incident mode), the starting source fields, u_i (e.g. TE_{02} for this case), the target Gaussian beam, G_s (on the launcher output aperture) and the maximum size of the perturbation, $\left| \Delta \rho \right|_{max}$. The perturbations are calculated for the last Brillouin zone (the zone closest to the output aperture) first; G_s is back propagated and u_i is forward propagated to this zone, and the phase difference between the incoming and outgoing E_ϕ part of these two fields are converted to perturbations (the phase difference must be unwrapped if necessary). This step is reiterated for the next zone (the penultimate zone closest to the output aperture) and then it is repeated for the rest of the zones. The whole process can be iterated again if $\left| \Delta \rho \right|_{max}$ has not been achieved. If at any point during the process the output radiation pattern is deemed acceptable, then the process can be stopped (this rarely happens). Next the perturbations are filtered with a Gaussian function to smooth the discontinuities at the borders of the different zones and also to remove any rapidly-varying or high-frequency perturbations. A better output radiation pattern is observed when the filtering is done at the end of the design stage instead of between successive zones. Filtering the perturbations might or might not worsen the output radiation pattern. Finally the perturbations are then tapered at the beginning of the launcher.
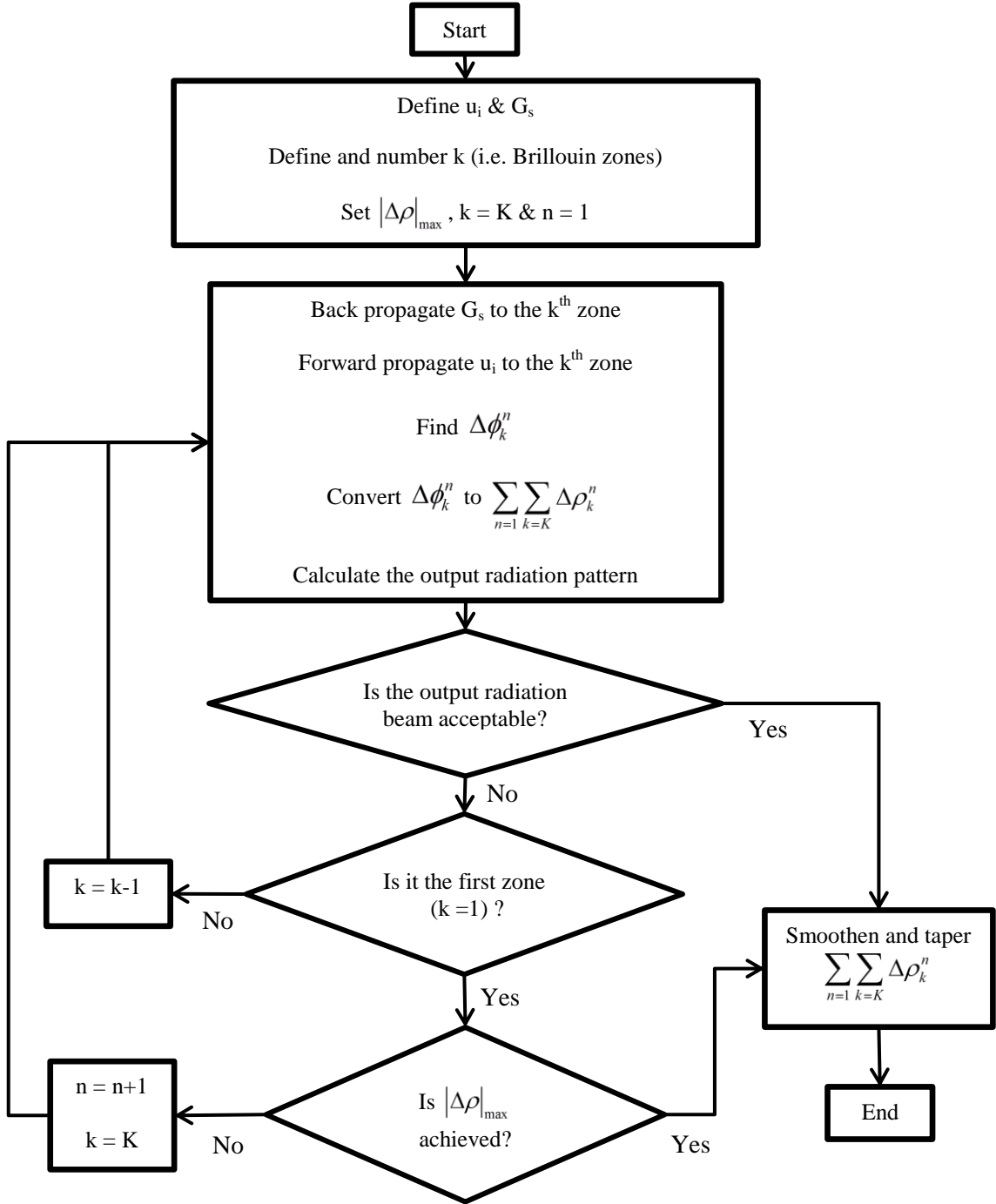
Figure 5.1.2: Flowchart for the launcher design method. The variable k (k = 1, 2, … K) indicates the Brillouin zone (with the K being the zone closest to the output aperture and 1 being the zone closest to the source) and n is the iteration index. G_s is the target Gaussian beam defined at the output aperture and u_i is the launcher source field.

There are a lot of complications and subjectivity in dealing with this launcher design method, and one of them is the evaluation of the launcher output radiation. It is tricky to evaluate the output radiation beam because of the problem with quantifying the side lobes. For example, a certain perturbation profile might give an output beam with a high Gaussian correlation (~98%) but the side lobes could be unacceptably large. The converse case is where the Gaussian correlation is low (~80%) but where the side lobes are small. For this dissertation, a good output result must have the following criteria: 1) the main lobe must contain a large amount of the total output power (> 90%), 2) the main lobe is collimated and can be fully captured by the proceeding mirror system, 3) the Gaussian content of the main lobe should be moderately high (> 90%), and 4) the side lobes should be small. These criteria are only evaluated by visual inspection.

5.2 Target Gaussian beam definition

An integral portion of this launcher design method is the choice of the target beam because it strongly influences the perturbation profile, and thus the output radiation pattern. Typically, the target beam is intended to be Gaussian. In circular waveguides or launchers, a Gaussian distribution on a Brillouin zone (or output aperture) is basically the combination of the right waveguide modes. In certain launcher design approaches (e.g. the $TE_{22,6}$ launcher in Chapter 4), the modal decomposition of this Gaussian distribution can be expressed analytically (e.g. up to 98% accurate for the $TE_{22,6}$ launcher [32]). Then analytical-type perturbations are applied to couple the incident mode to the required modes. However, this approach does not work for TE_{0n} type launchers or highly oversized launchers. Furthermore, obtaining the modal decomposition of an arbitrary Gaussian distribution on a Brillouin zone is not easy. The launcher design method developed in this report does not require an *a priori* knowledge of such modal information.

For this launcher design method, GO is used for the target Gaussian beam, G_s, definition at the half-cylinder output aperture (i.e. target Brillouin zone). G_s is formed at the output aperture by projecting a linearly polarized Gaussian beam (see Appendix A) that is tilted at the axial bounce angle of the launcher incident field, θ_b. The waist planes, $z_{0x'}$ and $z_{0z'}$, of G_s should be located at waveguide axis (i.e. G_s is a stigmatic beam, $z_{0x'} = z_{0y}$). To get G_s to align at the center of the output aperture, the waist planes of the Gaussian beam should be longitudinally located at the middle of the baffle. There are two competing factors that dictate the choice for the

waist values, $w_{0x'}$ and w_{0y}, of G_s. 1) The waists should be small enough so that the magnitude of G_s is as small as possible at the boundary of the output aperture (to minimize discontinuity at the launcher boundary). 2) The waists should be as large as possible to reduce beam divergence (i.e. beam divergence, Θ, is roughly proportional to the ratio of wavelength to waist value, λ / w_0). A strongly divergent launcher output radiation is highly undesirable and it may also complicate possible mirror system design. The first condition applies to all launchers, however, the second condition is more launcher specific (i.e. in some launchers, the possible choices for the waist values are all comparable to the wavelength, while in other launchers, the waist values can be chosen to be larger than the wavelength). The side view of the schematic diagram for this G_s definition together with the relevant coordinate system is pictured in Fig. 5.2.1.
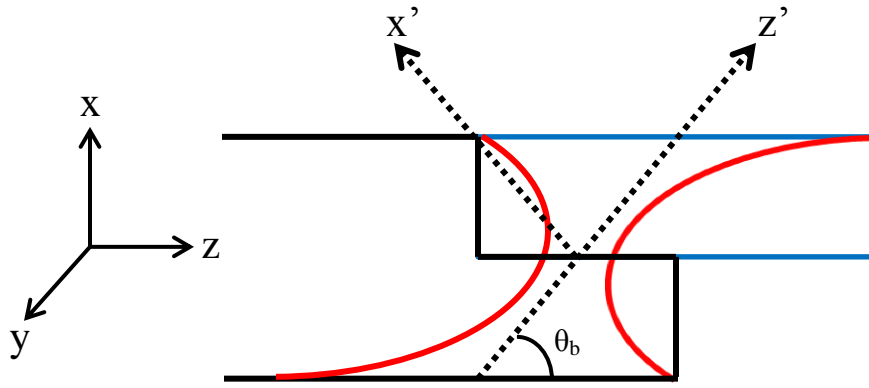

Figure 5.2.1: Side view of the schematic diagram for the target Gaussian beam, G_s, definition. The blue rectangle is the cross-section of the output aperture and the red lines are the arbitrary outlines of the tilted Gaussian beam. The dotted lines represent the new coordinate system of the tilted G_s.

When G_s is properly defined (as described in the previous paragraph and in Fig. 5.2.1), it should have the same propagation parameters (e.g. axial bounce angle, θ_b, and propagation constant, β_z) as the launcher incident beam, u_i. The cylindrical spectrum of G_s should be a distribution that peaks at the azimuthal index, m and also the propagation constant of u_i. Figure 5.2.2 is approximately what the cylindrical spectrum of G_s should look like when G_s is correctly defined. Another crucial factor that should be taken into account in the cylindrical spectrum domain is the spectral mask (Section 4.3 and Fig. 4.3.2). For G_s, large spatial waists have small spectral distributions, and vice versa. The more highly oversized the launcher is, the more probable for the spectral distribution of G_s to be cut-

off by the spectral mask. This is also a reason why the waists of G_s should be chosen to be as large as possible. For this launcher design method, the spectral mask is the limiting factor in the design of highly oversized launchers. In this dissertation, a launcher with a maximum OF of 2.66 has been successfully designed (section 6.4). If for example, a launcher with an OF of >4.00 is to be designed, this method will produce poor results.
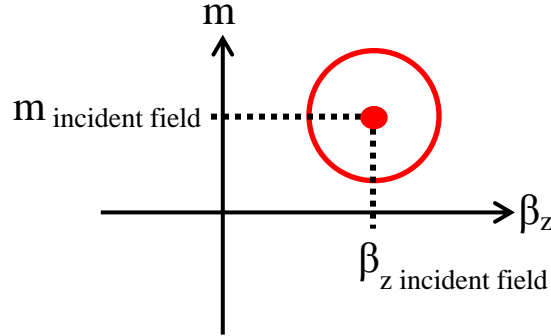

Figure 5.2.2: Cylindrical spectrum of G_s when it is correctly defined. The red dot represents the peak of the spectrum. The incident field refers to u_i, which is the launcher incident field.

The main problem with this launcher design method arises from back propagating G_s. Because G_s is not an eigenmode of the waveguide (it doesn't satisfy the boundary conditions on the waveguide walls), it can never truly propagate in a circular waveguide. At most, we can "force" G_s to propagate, but at some point during its propagation, this G_s beam is going to disperse and disintegrate into other propagating and/or evanescent modes. From experimenting with propagating G_s (of certain parameters) with the ISC, it can be seen that G_s loses its Gaussian shape and disintegrates rapidly after propagating beyond the first Brillouin zone. This problem is exacerbated the more divergent the G_s beam is. One way of mitigating this back propagation problem is by a reasonable and careful construction of G_s, as described in previous paragraphs. Although this back propagation method does not appear to be theoretically accurate, it has been used by other research groups and it will be shown in the proceeding sections that good to excellent results can still be achieved from this method.

It needs to be mentioned that a Gaussian beam is not the only viable option as the target beam. Any other well-defined Gaussian-like target beam can also be applied, although a Gaussian beam would be the best choice and also the most natural choice. A TE_{02} launcher with a target beam that is similar (but not the same) to a Gaussian beam has been designed and verified (using Surf3d) [43]. The results were acceptable, but using a target Gaussian

beam would have produced better results. Other launcher design methods that do not utilize a Gaussian beam (but similar to a Gaussian beam) as their target beam have also been developed, for example in the design of a 170 GHz $TE_{34,19}$ launcher [23]. A possible explanation for this could be because of the difficulty in defining a target Gaussian beam for the $TE_{34,19}$ mode. Defining a target Gaussian beam for the $TE_{34,19}$ mode involves more parameters (and more degrees of freedom for the combination of the parameters) compared to the TE_{02} mode.

5.3 Phase corrections and conversion to perturbations

The ISC allows for the phase corrections to be evaluated directly on the perturbed waveguide walls, and for the phase corrections to be calculated from the E_ϕ field instead of the H_z field (Chapter 4). The E_ϕ field is valued over H_z because ultimately the launcher output radiation is polarized in E_ϕ. Furthermore, the field expressions for E_ϕ and H_z are dissimilar (from Eq. (2.1.1)), so calculating phase corrections from the H_z field will not result in the best E_ϕ radiation pattern. This problem is compounded for launchers with high OFs. The equations and derivations in this section are adapted from a K-S based mirror design algorithm [20].
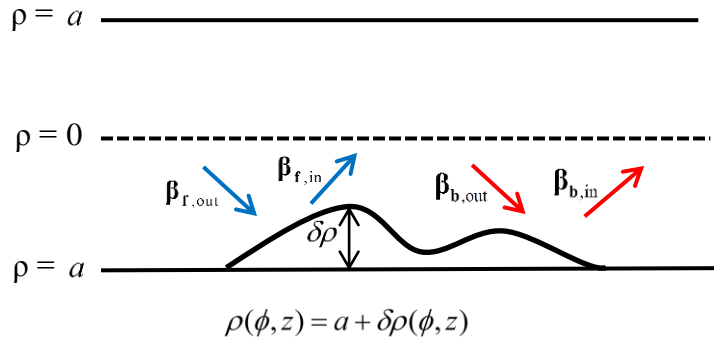

Figure 5.3.1: Diagram showing an arbitrary and exaggerated perturbation profile. $\boldsymbol{\beta_f}$ is the local wave vector of the forward propagating field, and $\boldsymbol{\beta_b}$ is the local wave vector for the back propagated field. The subscript in and out refers respectively to the incoming and outgoing parts of the wave vectors. This figure is not to scale and is adapted from a K-S based mirror surface correction equation [20].

Figure 5.3.1 illustrates an arbitrary perturbation profile together with the forward propagating and back propagated fields in a circular waveguide. Also, these fields can be separated into the incoming and outgoing parts. The surface of the smooth-wall launcher is represented by $\mathbf{r'}$, and the surface where the phase is to be determined is represented

by $\mathbf{r}$. Any scalar field can be separated into magnitude and phase, for example the E_ϕ field on the smooth-wall launcher can be described as

$$E_\phi(\mathbf{r'}) = | E_\phi(\mathbf{r'}) | \, e^{j\theta(\mathbf{r'})}. \tag{5.3.1}$$

Similarly, the E_ϕ field can be separated into the incoming, $E_{\phi,\text{in}}$, and outgoing parts, $E_{\phi,\text{out}}$. The eikonal approximation [34, pp. 116-135] relates the phase, θ, to the wave vector, $\mathbf{\beta}$ by

$$\mathbf{\beta}(\mathbf{r'}) \approx -\nabla\theta(\mathbf{r'}), \tag{5.3.2}$$

and the relative phases of the forward propagating and back propagated fields at $\mathbf{r}$ from the smooth-wall surface can be approximated as

$$\theta_{f/b}(\mathbf{r}) \approx -\mathbf{\beta_{f/b}}(\mathbf{r'}) \cdot (\mathbf{r} - \mathbf{r'}) + \phi_{f/b}(\mathbf{r'}), \tag{5.3.3}$$

where $\phi_{f/b}$ are the phases of the forward propagating and back propagated fields on the smooth-wall launcher. In this K-S algorithm adapted for circular waveguides, the phase difference between the incoming forward propagating fields and the outgoing back propagated fields is taken in each iteration and transformed to perturbations (until they converge), and this requirement is expressed as

$$\theta_f - \theta_b = (\mathbf{r} - \mathbf{r'}) \cdot (\mathbf{\beta_{f,\text{in}}} - \mathbf{\beta_{b,\text{out}}}) + (\phi_f - \phi_b) = C. \tag{5.3.4a}$$

Correspondingly, Eq. (5.3.4a) can also be substituted by

$$\theta_b - \theta_f = (\mathbf{r} - \mathbf{r'}) \cdot (\mathbf{\beta_{b,\text{in}}} - \mathbf{\beta_{f,\text{out}}}) + (\phi_b - \phi_f) = C. \tag{5.3.4b}$$

The difference between the original surface and the new surface (i.e. the perturbations) in Eq. (5.3.4) is represented by the vector $\mathbf{\delta r} = \mathbf{r} - \mathbf{r'}$, and C is just an arbitrary constant (that depends on how the perturbations are added in each iteration). The perturbations are assumed to be defined only in the radial component, i.e. $\mathbf{\delta r} = \delta\rho\hat{\mathbf{\rho}}$, $\delta\rho = \Delta\rho$ and $\delta\phi = \delta z = 0$. Now the perturbation profile, $\Delta\rho$ can be characterized as

$$\Delta\rho(\phi,z) = \frac{\phi_f(\phi,z) - \phi_b(\phi,z) - C}{(\boldsymbol{\beta}_{\mathbf{f},in}(\phi,z) - \boldsymbol{\beta}_{\mathbf{b},out}(\phi,z)).\hat{\boldsymbol{\rho}}}. \tag{5.3.5a}$$

The wave vectors in the denominator of Eq. (5.3.5a) are hard to evaluate, especially for fields inside circular waveguides. Ideally the wave vectors are calculated from the unwrapped phases of the fields using Eq. (5.3.2). For mirror designs, the fields are propagating in free space and determining their wave vectors is relatively straightforward. The difficulties in determining the wave vectors in waveguides come from, 1) the back propagated target Gaussian beam does not have a well-defined wave vector (section 5.2), 2) inaccurate phase information due to fields with low magnitude (i.e. problems with phase unwrapping on the waveguide walls, section 3.4), and 3) the possible presence of several wave vectors and the spectral spread of wave vectors, at the point of evaluation. Applying the GO theory of fields (Chapter 2) allows the wave vector to be approximated (to the first order) as rays propagating at the axial bounce angle, i.e. $\boldsymbol{\beta}_{\mathbf{f},in/out} = \boldsymbol{\beta}_{\mathbf{b},in/out} = \mp\beta_\rho\hat{\boldsymbol{\rho}} + \beta_z\hat{\mathbf{z}} = \mp\beta\sin\theta_b\hat{\boldsymbol{\rho}} + \beta\cos\theta_b\hat{\mathbf{z}}$. Finally, Eq. (5.3.5a) can be reduced to

$$\Delta\rho(\phi,z) = \frac{\phi_f(\phi,z) - \phi_b(\phi,z) - C}{2\beta\sin\theta_b}. \tag{5.3.5b}$$

Although Eq. (5.3.5b) employs approximations in the denominator, the resulting perturbation profile yields good to excellent output radiation patterns, as proven in the next section.

In practice, most perturbations must be scaled to fit within the design parameter of the maximum perturbation size. This is especially true for launchers with high OFs where the axial bounce angle, θ_b is small. For the PoM launcher design (Section 6.2), the approximated radial component of the wave vector is relatively small ($\beta_\rho = 5.05$ rad/cm). A phase shift of π radians in the radial direction requires an excessive perturbation size ($|\Delta\rho|$ = 0.62 cm or $|\Delta\rho|$ is 45% of the radius), hence requiring the perturbations to be scaled. Due to this restriction, the perturbations must be distributed over a few Brillouin zones, instead of being implemented on two or three Brillouin zone (section 3.3). The more Brillouin zones that are available (i.e. the longer the launcher), the smaller the perturbations can be, and the better the output radiation pattern will become.

The second problem with this launcher design method is related to the limitation of the K-S phase-correcting algorithm (Chapter 3). This algorithm only produces perturbations that maximize the coupling of the launcher output radiation pattern to the target Gaussian beam, without regard to minimizing the side lobes. As such, there are circumstances where the K-S algorithm results in a high-content output Gaussian beam but with side lobes that are huge and unacceptable. There is no direct control over the magnitude of the side lobes, however, numerical experimentation of this method shows a strong correlation between moderate sized perturbations and low side lobes.

5.4 Optimization of design and algorithmic parameters

There are numerous parameters involved in this method, and they need to be fine-tuned to get the best launcher results. For example, recall that GO was utilized in the target Gaussian beam, G_s, definition, and this only serves as a good initial first guess. Some G_s can be better expressed as waveguide modes than other G_s, and therefore would yield smaller and smoother perturbations, and also better launcher output radiation patterns. Table 5.4.1 is a list of the important parameters with some helpful guidelines for optimization. Apart from the Gaussian filter and spectral mask, the other parameters are optimized by trial and error. Unless listed in Table 5.4.1, all the other parameters have low to negligible effect on the launcher design method.

Table 5.4.1: List of Essential Parameters for the Launcher Design Method with Helpful Guidelines.

Parameter	Importance	Notes
Target Gaussian beam	High	Refer to Section 5.2. The most important parameters are the waists values. Also, usually the longitudinal location of the waist planes should be offset by a small amount (because of the spreading of the Gaussian beam).
Maximum perturbation size	High	For the launcher output radiation, large perturbations provide higher Gaussian content but may also give large side lobes. There is an optimal perturbation size that gives both a high Gaussian content and low side lobes. Furthermore, large perturbations could lead to significant mode reflections inside the launcher.
Gaussian filter	Moderate	Controls the smoothness of the perturbations. The more rapidly-varying the perturbations are, the more modes can be generated and the higher the Gaussian content of the output beam. However the output radiation pattern will worsen if the perturbations have too much high spatial frequency components (e.g. too sharp or discontinuous). This factor is also limited by the machinability of the fabrication process.
Spectral Mask	Moderate	Controls the number of modes included in the forward and back propagation calculation for the ISC. For the TE_{02} launcher design examples, modes with azimuthal variations larger than six ($m > 6$) and modes that are too far away from the incident TE_{02} mode that are undesirable are to be suppressed.
Waveguide and baffle length extension	Low to moderate	Extending the waveguide and/or baffle (that have perturbations) can further reduce edge diffraction losses and slightly improve the quality of the main lobe of the output radiation pattern.

Chapter 6: Highly Oversized TE$_{02}$ Launcher Designs

In this chapter, the design of two types of highly oversized launchers will be presented. The first launcher is the proof-of-method (PoM) launcher (2.49 OF), and the second launcher is the HSX launcher (2.66 OF). The details for these two launchers are presented in Table 2.2.1. Typically highly oversized launchers are located external to the gyrotron and the launcher lengths are not restricted.

6.1 The smooth-wall PoM launcher

The PoM launcher was the first launcher designed using the launcher design method. The TE$_{02}$ mode and the 60 GHz frequency were chosen because these were the parameters of General Atomics' (GA) gyrotrons (200 kW) for the DIII-D tokamak system in San Diego. Furthermore, the QOMC measurements lab in UW Madison has the equipment for testing the PoM launcher at 60 GHz if this launcher were to be built. The launchers in GA's gyrotrons were waveguide mode converters.

In this section, the far-field radiation pattern from the smooth-wall PoM launcher is investigated using Surf3d. The losses or inefficiencies in this far-field radiation pattern will be identified and analyzed, and will be compared with the radiation pattern from the perturbed-wall launcher in a later section. Figures 6.1.1 and 6.1.2 show respectively the far-field patterns of the co-polarized $\left|E_\phi\right|$ field and cross-polarized $\left|E_\theta\right|$ field of the smooth-wall PoM launcher from Surf3d in log scale. Although the cross-polarization is not zero, it is small (< -17.9 dB) and is considered negligible. (Note that the cross-polarization is slightly asymmetrical. Ideally it should not be and this is attributed to computational inaccuracies of Surf3d). There are several problems with the far-field co-polarization:

1) The biggest problem is with the main lobe. The main lobe is double-peaked (not Gaussian shaped), the percentage of the power in the main lobe is low (79.4%), and the azimuthal spread is too large (more than 180°). If a set of focusing and phase-correcting mirrors are to be utilized following the launcher, a large amount of output power cannot be captured and is lost. Moreover, it is difficult for any kind of mirror system to convert this double-peaked main lobe into a good Gaussian beam output.
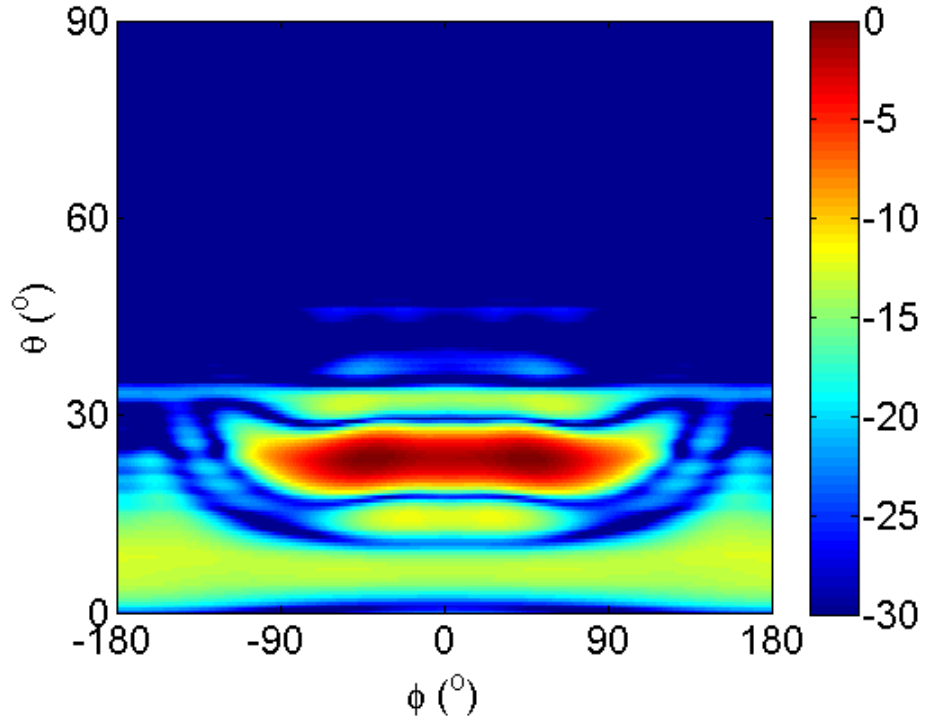
Figure 6.1.1: The far-field pattern of $|E_\phi|$ (co-polarization) of the smooth-wall PoM launcher (in dB) obtained from Surf3d.
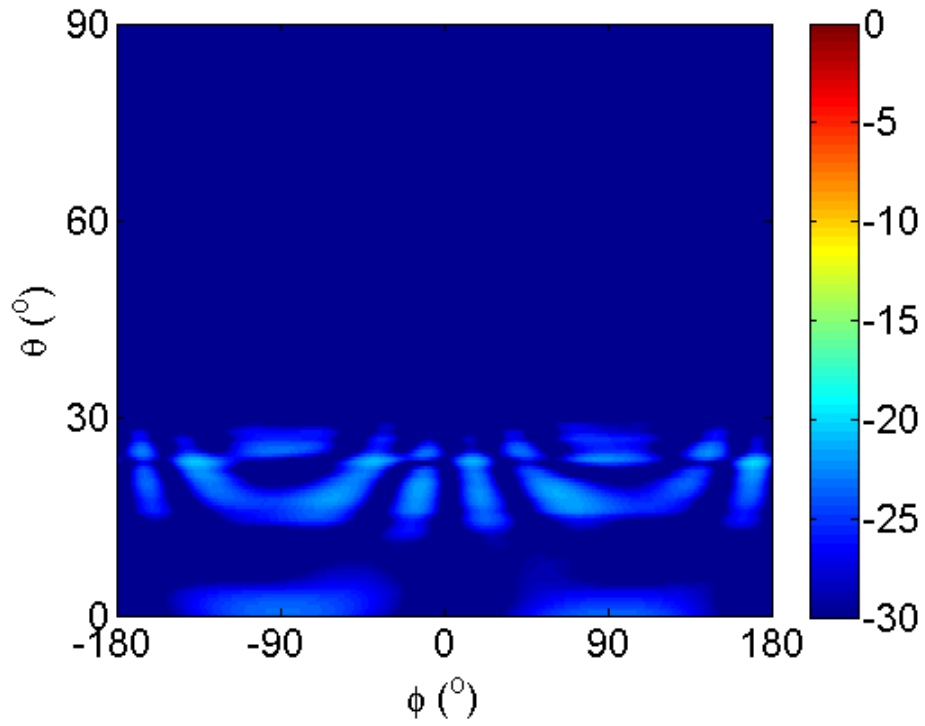

Figure 6.1.2: The far-field pattern of $|E_\theta|$ (cross-polarization) of the smooth-wall PoM launcher (in dB) obtained from Surf3d.

2) There are major edge diffraction losses. Because the magnitude of the fields hitting the launcher walls are nearly constant everywhere (from a GO view), a lot of the fields will be unwantedly diffracted by the launcher cut and are lost.

3) The side lobes are substantial and they come from the smooth-wall launcher radiation itself and from edge diffraction. These large side lobes can't be captured or converted by most mirror systems and are also lost.

Perturbations will be applied (produced by the launcher design method) to the PoM launcher to solve or mitigate all of the problems listed above.

6.2 Results and discussion for the perturbed-wall PoM launcher

Numerous launchers with different parameters were designed and the launcher with the best output radiation pattern was selected. The parameters of the launcher were then further carefully optimized to get the best radiation pattern. The final PoM launcher design is presented in this section.

Table 6.2.1: Summary of the Far-field Comparison between the PoM Launchers.

Launcher	Co-polarization (E_ϕ)					Cross-polarization (E_θ)	
	Polar Exit Angle	Power in Main Lobe	Directivity, D_ϕ	10 dB Angular Spread		$\|E_\theta\|_{max}$	Total Power
				Azimuthal, $\Delta\phi$	Polar, $\Delta\theta$		
Smooth-wall	23.5°	79.38%	21.5 dBi	208.4°	8.5°	-20.0 dB	0.09%
Perturbed-wall	23.5°	99.67%	23.5 dBi	91.2°	14.3°	-18.6 dB	0.28%

Far-field radiation patterns are useful in evaluating the performance of launchers. Figures 6.2.1 and 6.2.2 display the far-field patterns of the perturbed-wall launcher from Surf3d in log scale, and the differences (with Figs. 6.1.1 and 6.1.2) are summarized in Table 6.2.1. Adding perturbations to the launcher has led to major improvements in the output radiation pattern. The main lobe is now Gaussian shaped and contains nearly all of the output power. Equally important is that the azimuthal spread of the main lobe is shrunk by more than half. The polar spread is larger, but still small enough so as to not pose a problem for the proceeding mirror system. Additionally, the side lobes are dramatically mitigated, with a maximum peak of approximately -22 dB. The combined improvement in the main lobe and reduction of side lobes lead to an increase of the directivity of the co-polarization, D_ϕ, by 2 dB.

Although the cross-polarization has risen, it is still insignificantly minor. The polar exit angles of the launchers are the same, and they correspond squarely with the TE_{02} mode axial bounce angle of 23.65^o.

Apart from this PoM launcher, other perturbed-wall launcher designs have shown that the polar spread, $\Delta\theta$, of the co-polarization of the far-field is almost always larger compared to the smooth-wall case (Sections 6.4 and 7.2), and this effect could be undesirable. A better illustration of this effect is provided in Figs. 6.2.3 and 6.2.4, which display the side view of the fields emanating from the smooth-wall and perturbed-wall launchers respectively. The smooth-wall launcher has a smaller far-field main lobe polar spread because a lot of the side lobes deviate away from the main lobe, and are therefore lost. From Fig. 6.2.2, the perturbations have steered some of the side lobes towards the main lobe, resulting in a more collimated and focused main lobe. In the far-field, this consequence translates to a wider polar spread for the main lobe. Numerous algorithmic and design parameters (in the launcher design method) have been tried for this PoM launcher (and also for the ADS and HSX launchers) in order to obtain a reduction in the far-field polar spread, but no such reductions ensued. It turns out that this increase in the far-field polar spread is not a limitation of the launcher design algorithm, but instead is a fundamental limit.

In aperture antennae, there is a qualitative theory that states that the far-field radiation pattern is the Fourier transform of the field pattern at the antenna aperture. For QOMC launchers, the cylindrical output aperture can be thought of as the equivalent antenna aperture. To further simplify the analysis, only a horizontal line along the $x = $ radius at the $y = 0$ plane of the output aperture is considered (refer to Fig. 5.1.1). From GO, the field distribution along this horizontal line from a smooth-wall launcher is constant, and this would translate to a sinc function along the polar coordinates in the far-field. A sinc function has many large and undesirable side lobes, and this effect is visible by just looking at the $\phi = 0^o$ cross-section of Fig. 6.1.1. However, the main lobe of the sinc function can be rather narrow in this direction. For the perturbed-wall launcher, the field function across the horizontal line along the output aperture is Gaussian, which means that its far-field radiation pattern (across the polar coordinates) is also a Gaussian function, as can be seen in the $\phi = 0^o$ cross-section of Fig. 6.2.1. Although the far-field polar spread is larger, there are no side lobes in a Gaussian distribution. To get the narrowest polar spread together with the smallest side lobes in the far-field, a Gaussian field distribution is the best option at the antenna aperture.
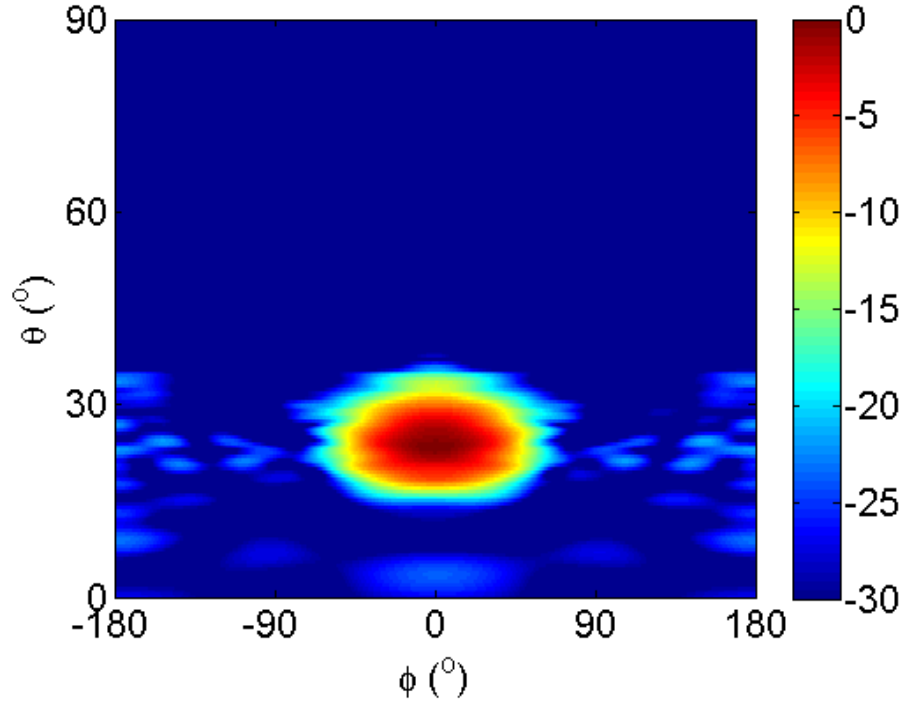
Figure 6.2.1: The far-field pattern of $|E_\phi|$ (co-polarization) of the perturbed-wall PoM launcher (in dB) obtained from Surf3d.
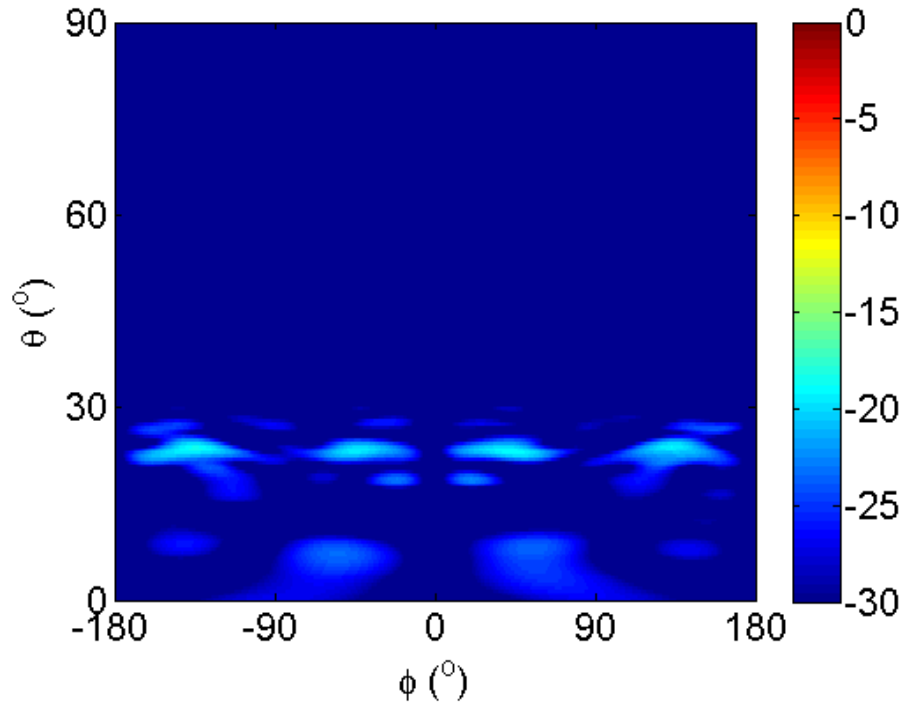

Figure 6.2.2: The far-field pattern of $|E_\theta|$ (cross-polarization) of the perturbed-wall PoM launcher (in dB) obtained from Surf3d.
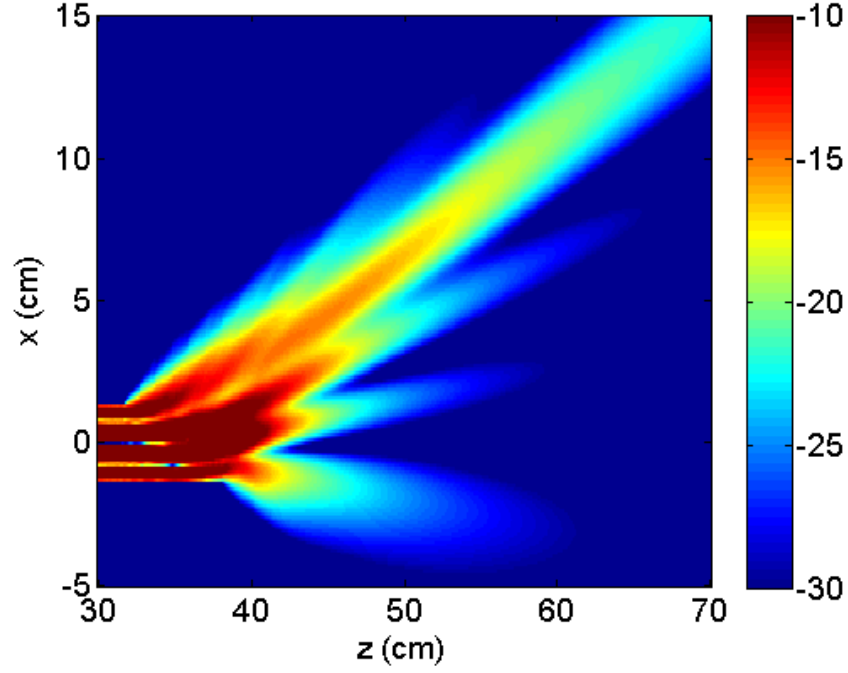
Figure 6.2.3: The side view of the fields ($\left| E_y \right|$) radiating from the smooth-wall PoM launcher (in dB) obtained from Surf3d. The scale for the magnitude of the fields is tuned to accentuate the side lobes.
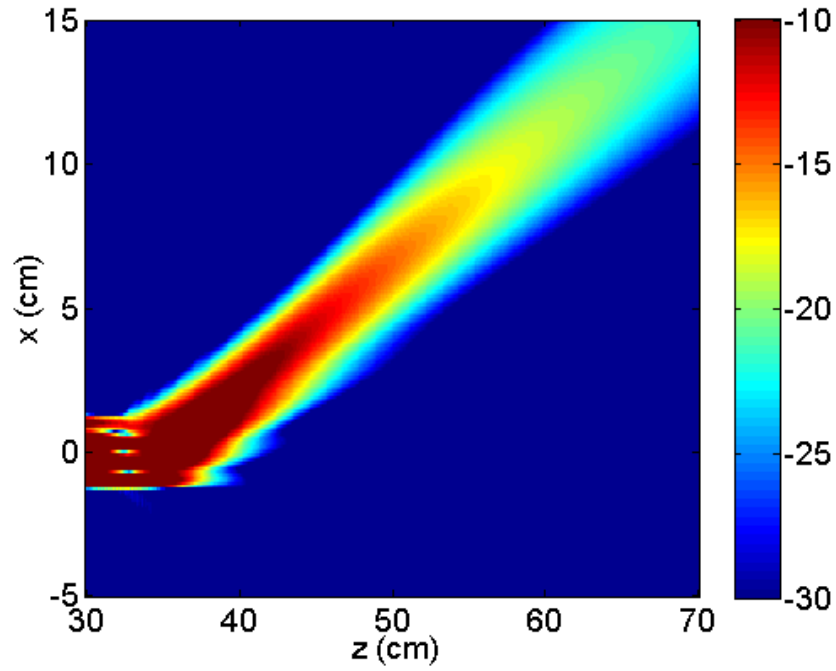

Figure 6.2.4: The side view of the fields ($\left| E_y \right|$) radiating from the perturbed-wall PoM launcher (in dB) obtained from Surf3d. The scale for the magnitude of the fields is tuned to accentuate the side lobes.

In practice the mirror system and gyrotron windows are located in the radiating near-field region of the launcher (the far-field distance for this TE_{02} launcher is approximately 2 meters). Figures 6.2.5 and 6.2.6 display all field components at the output aperture and after the launcher cut obtained from Surf3d simulations and from calculations respectively. The correlation coefficients with these two figures are presented in Table 6.2.2 (an explanation for the differences in these correlation values are discussed in Section 7.1). As predicted from theory (section 2.1), E_ϕ and H_ρ, and E_ρ and H_ϕ share the same radiation pattern. For this high OF, H_ρ is now the largest **H** field component, instead of H_z. The resultant E_ϕ field at the output aperture has a complex scalar correlation, c_{cs} of 95.7% to an astigmatic and elliptical Gaussian beam of waist values of 2.78cm and 1.04 cm, and exit angle of 23.42°. Furthermore, the side lobes for the main E_ϕ field and the rest of the fields are small. The cross-polarized E_z field is small (less than -32 dB). For this reason, the complex scalar correlation is the better benchmark compared to the complex vector correlation. The E_z component of a Gaussian beam (with waists of 1.39 cm and 0.52 cm and projected at 23.42°) on the cylindrical output aperture is relatively large, with a maximum magnitude of -19.3 dB. Since the E_z field of this Gaussian beam is the unwanted cross-polarization, including it in assessing the performance of a launcher (i.e. by taking the complex vector correlation) would artificially lower the Gaussian content. (Note: this case only applies to launchers that have small axial bounce angles or polar exit angles). Figure 6.2.7 shows the cylindrical scan of the $\left|E_\phi\right|$ component at a radius of 4 cm, and this plot proves that it is possible to design a practical mirror that can fully capture the main E_ϕ beam in the radiating near-field.

Table 6.2.2: Correlation Coefficients Between the Results from Surf3d (Fig. 6.2.3) and From Those Calculated Using the ISC Method (Fig. 6.2.4). Note that the E_z field is omitted (also omitted from the **E** field) because it is too small to be reliable.

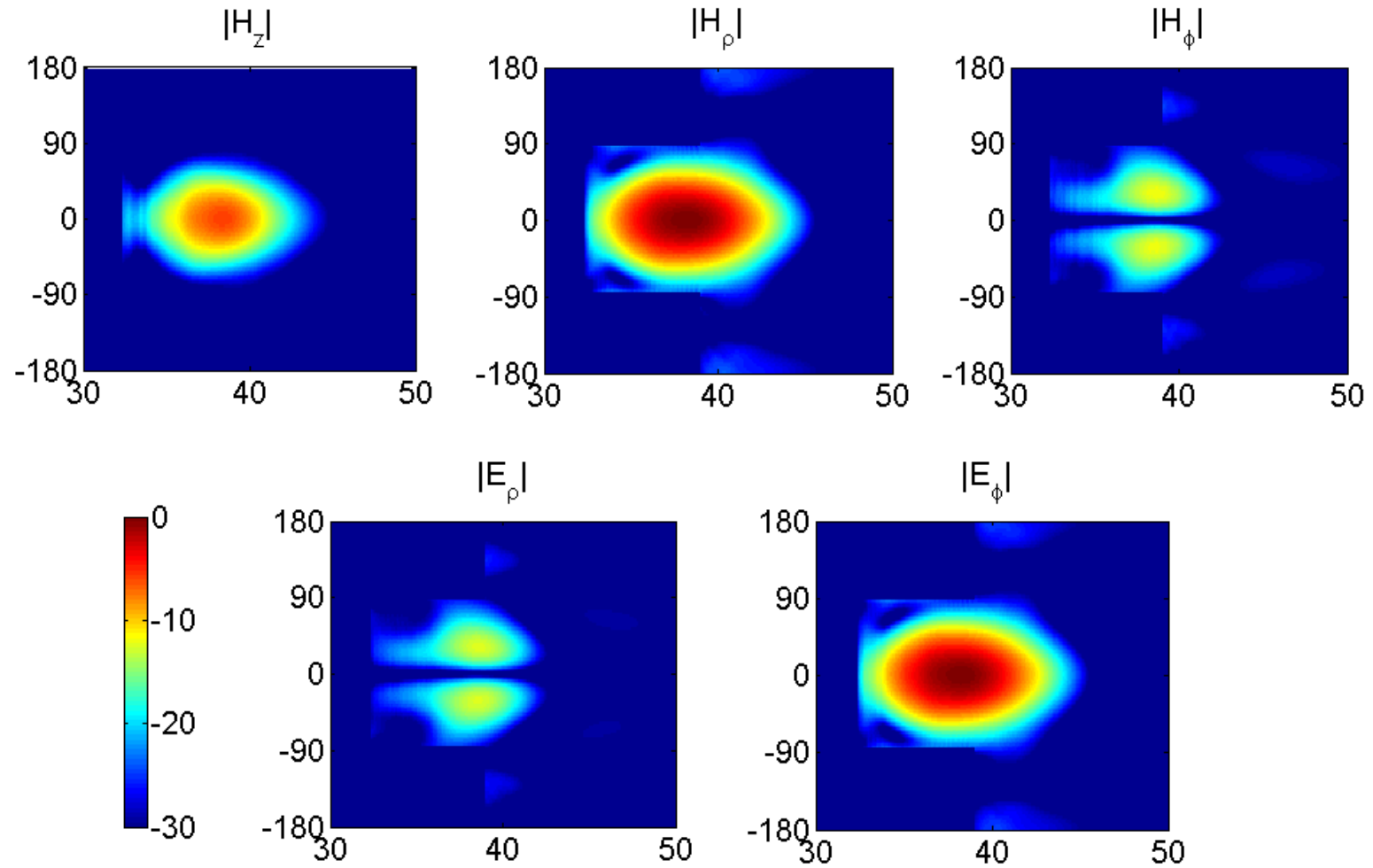| Complex scalar coupling, c_{cs}					Complex vector coupling, c_{cv}	
H_ρ	H_ϕ	H_z	E_ρ	E_ϕ	**H**	**E**
95.83 %	74.39 %	96.13%	75.53 %	96.11 %	94.80 %	94.96 %

Figure 6.2.5: All field components at the output aperture and after the launcher cut (in dB) from Surf3d. (Fields on the launcher walls are blanked out because Surf3d does not give accurate values there). The vertical axes are ϕ (^{o}) and the horizontal axes are z (cm). The $\left|E_z\right|$ field is not shown because it is negligible ($\left|E_z\right| < $ -30 dB).
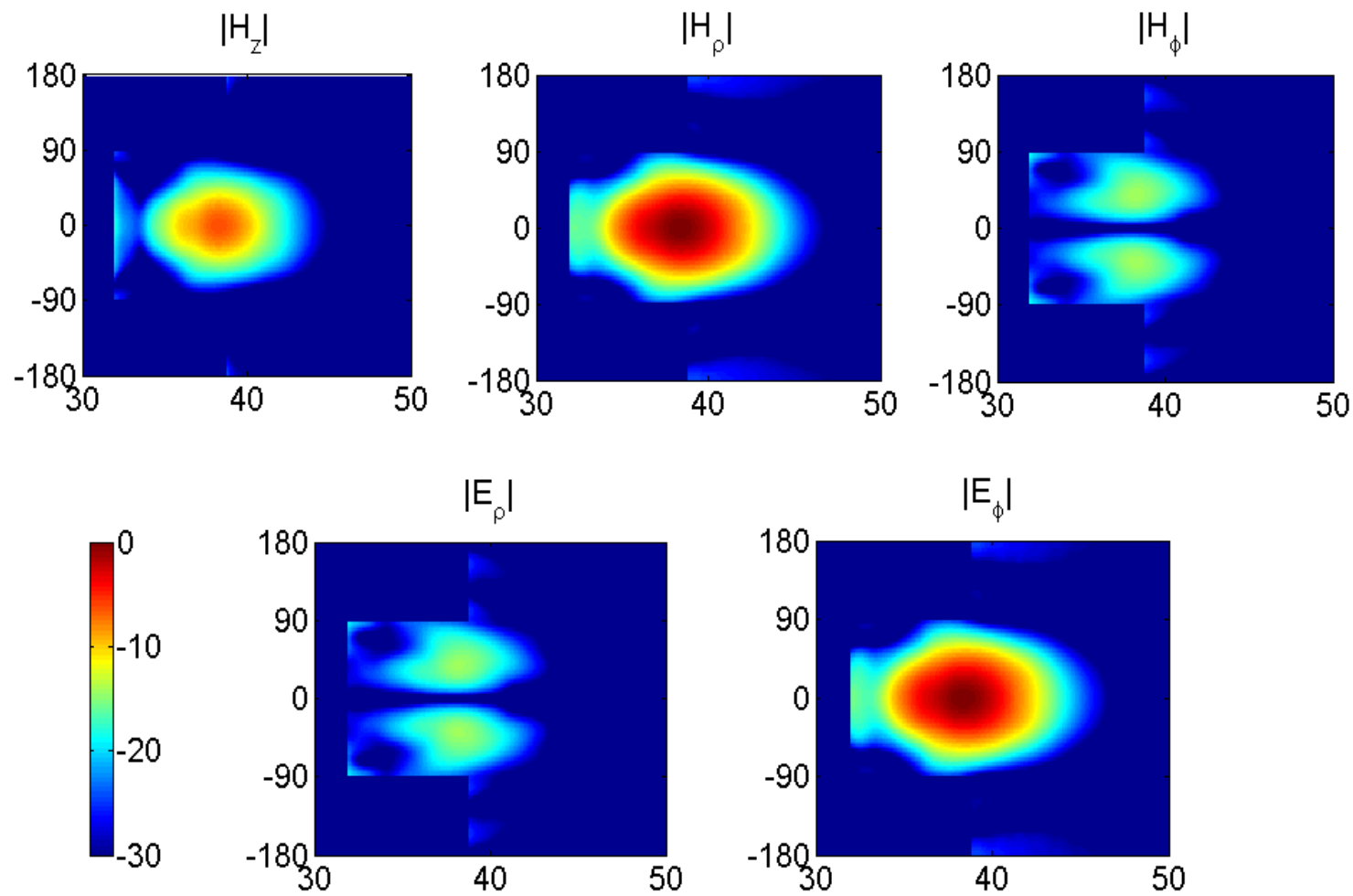
Figure 6.2.6: All field components at the output aperture and after the launcher cut (in dB) from calculation. (Fields on the launcher walls are blanked out for comparison purpose with the previous figure). The vertical axes are ϕ (°) and the horizontal axes are z (cm).

This perturbed-wall TE_{02} launcher is comprised of 5 ½ Brillouin zones. Although, this might seem like a lot, it is not as most launchers (like the $TE_{22,6}$ launcher in Chapter 4) have the equivalent of more than 7 Brillouin zones. Essentially a uniformly distributed source field (on the "source Brillouin zone") needs to be shaped into a Gaussian beam with minimal side lobes at the output aperture, all the while being limited by the size and shape restrictions of the perturbation profile. Figure 6.2.8 traces the evolution of the outgoing E_ϕ field as the field traverses the launcher. The E_ϕ field is examined here because the beam is shaped only by E_ϕ (not the total $\mathbf{E}$ field). Also, just the outgoing E_ϕ field is plotted because it is comparable everywhere (i.e. the incoming E_ϕ field is zero at the output aperture and nonzero on the launcher). It can be seen that the field is gradually transformed by each Brillouin zone from a constant field to a Gaussian shaped one at the output aperture. The beam evolution can be described as the following: 1) in zones 1 and 2, the field around the edges is slightly reduced by 3 to 4 dB. 2) In zones 3 and 4, the edge fields are further reduced by another 5 to 6 dB, and now the field in the center is starting to get concentrated. 3) In zone 5, there is a noticeable main lobe with a long tail at the center of the zone, and the edge fields are again decreased, reaching the -7 to -20 dB levels. 4) In the last zone a rough Gaussian beam is formed at the center and the edge fields are now lowered to a maximum of -13 dB (at the $\phi = 0^\circ$ location of the waveguide) down to -30 dB. Most of the beam shaping takes place at the later Brillouin zones, and this is due to how the phase corrections were performed (which is from the last zone to the first zone). Figure 6.2.9 exhibits the total $|\mathbf{H}|$ fields on the waveguide walls. This figure verifies that one of the stated design objectives of decreasing the fields on the launcher edge (to reduce edge diffraction) has been accomplished. The $|\mathbf{H}|$ field value on the launcher edge has been reduced to roughly -6.80 dB ($\phi = 0^\circ$ at the end of the waveguide) to -17.9 dB ($\phi = 95^\circ$ at the end of the baffle). A similar figure to Fig. 6.2.9 showing the total $|\mathbf{E}|$ field on the waveguide walls would be misleading because for TE_{0n} modes, all incident $\mathbf{E}$ components on the waveguide walls are zero. Calculating the $\mathbf{E}$ field from the $\mathbf{H}$ field on the waveguide walls using modal impedances is difficult since there are many modes present, and the modal composition varies by location.
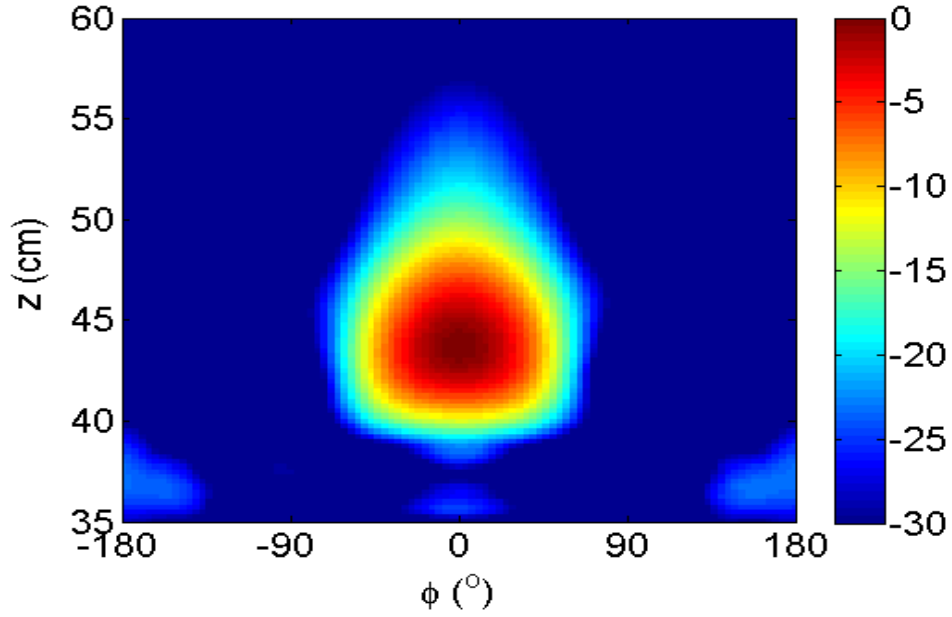
Figure 6.2.7: $|E_\phi|$ (in dB) radiated from the perturbed-wall launcher on a cylindrical surface of radius of 4 cm from the waveguide axis from Surf3d.
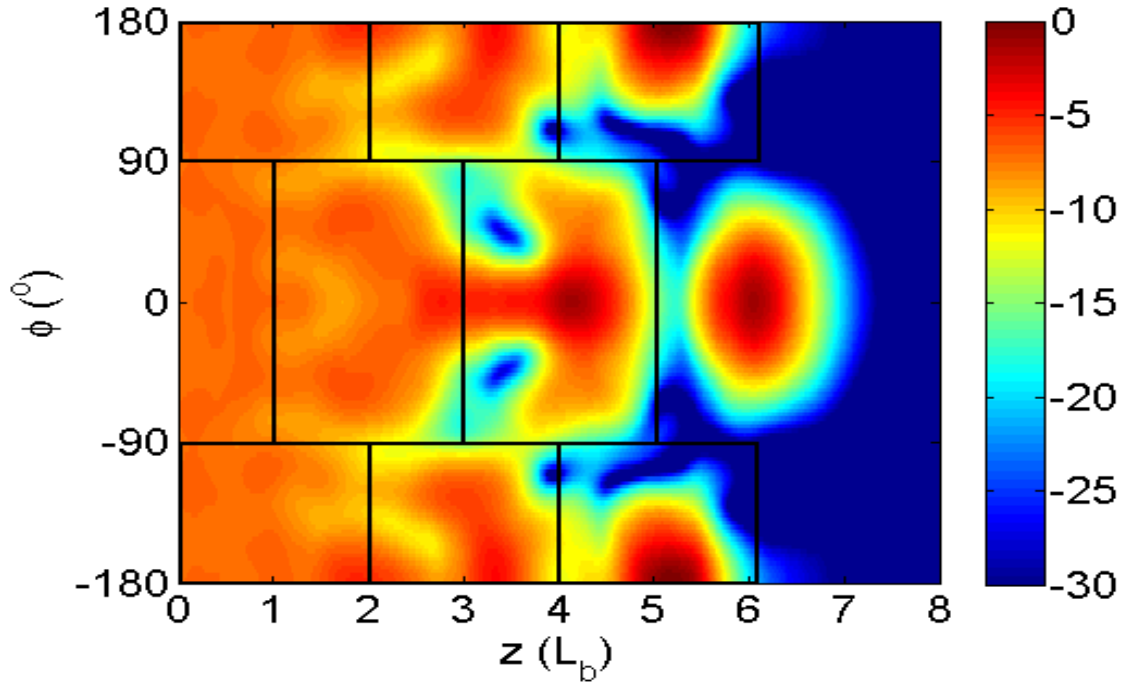

Figure 6.2.8: Magnitude of the outgoing E_ϕ field (in dB) on the perturbed-wall (with marked Brillouin zones) and output aperture from calculation. The horizontal axis is labeled in terms of the bounce length, L_b to aid in visualizing the Brillouin zones. Zones are numbered from left to right (1 to 6), starting with the half zone at the center, followed by the upper and lower second zone.
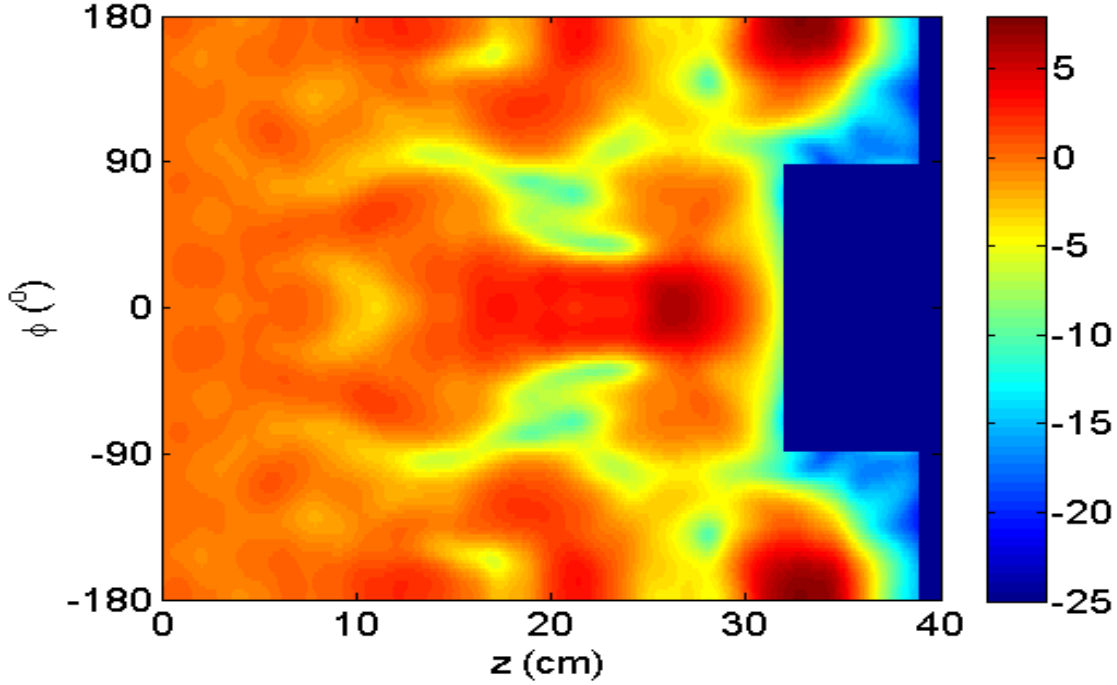
Figure 6.2.9: The $|\mathbf{H}|$ fields on the perturbed launcher walls (in dB) from calculation. The incident TE_{02} $|\mathbf{H}|$ field on the waveguide wall is set to 0 dB. Only the fields on the perturbed launcher walls are shown, the rest are blanked out.

The modal composition of the launcher could prove instructive, for example in the calculation of Ohmic losses. Figure 6.2.10 displays the cylindrical spectrum of the TE modes propagating inside the perturbed-wall launcher. The TE_{02} incident mode has no variation in the azimuthal direction, therefore equal amplitude counter-rotating modes are needed (for $m \neq 0$) to create the Gaussian distribution in the ϕ direction. This can be seen in the horizontal plane symmetry across the m = 0 index in Fig. 6.2.7. The list of main modes present in the launcher is TE_{02}, $TE_{\pm 22}$ and $TE_{\pm 13}$. The rest of the modes are $TE_{\pm 12}$, $TE_{\pm 32}$, TE_{01}, $TE_{\pm 41}$, $TE_{\pm 51}$ and $TE_{\pm 61}$. The ISC can only give the total spectral composition across the whole launcher (not on a single Brillouin zone), so further mathematical analyses must be done to determine which modes are important (i.e. contribute to the Gaussian distribution) and which modes are parasitic (i.e. reduce the Gaussian distribution). Most of these modes have radial wave numbers, β_ρ, that are close to the incident TE_{02} mode. Theoretically, mode to mode coupling is easier achieved when the differences in the radial wave number of the modes are small. As per the way the spectral mask was setup, no high order azimuthal modes (m >6) were excited.
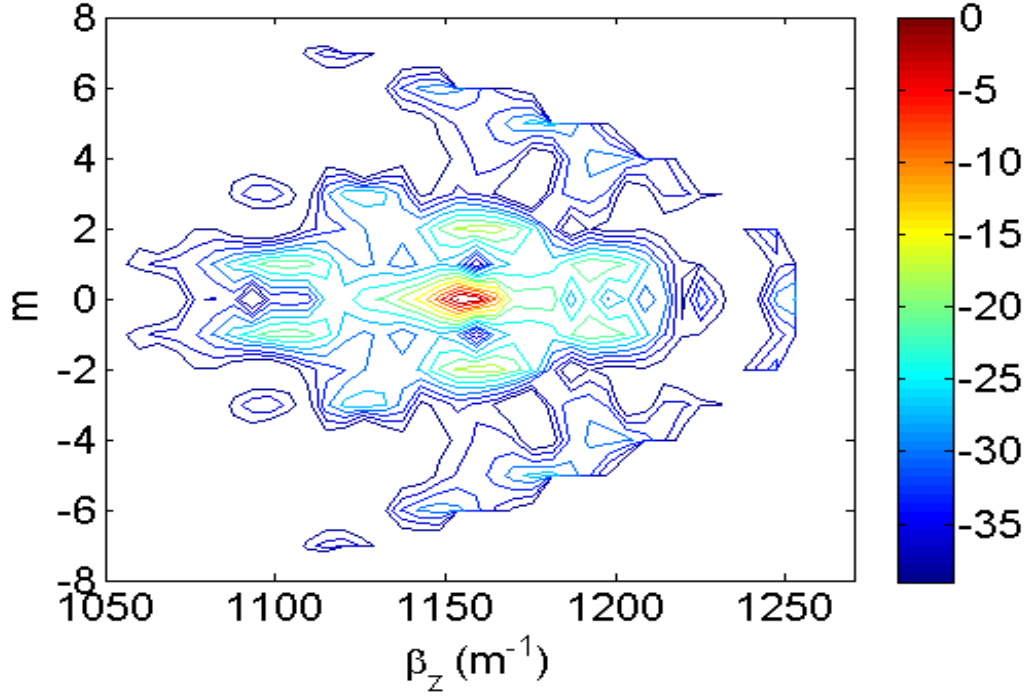
Figure 6.2.10: Contour plots of the TE mode cylindrical spectrum, $|a_m(\beta_z)|$ of the perturbed wall TE$_{02}$ launcher (in dB) from calculation.
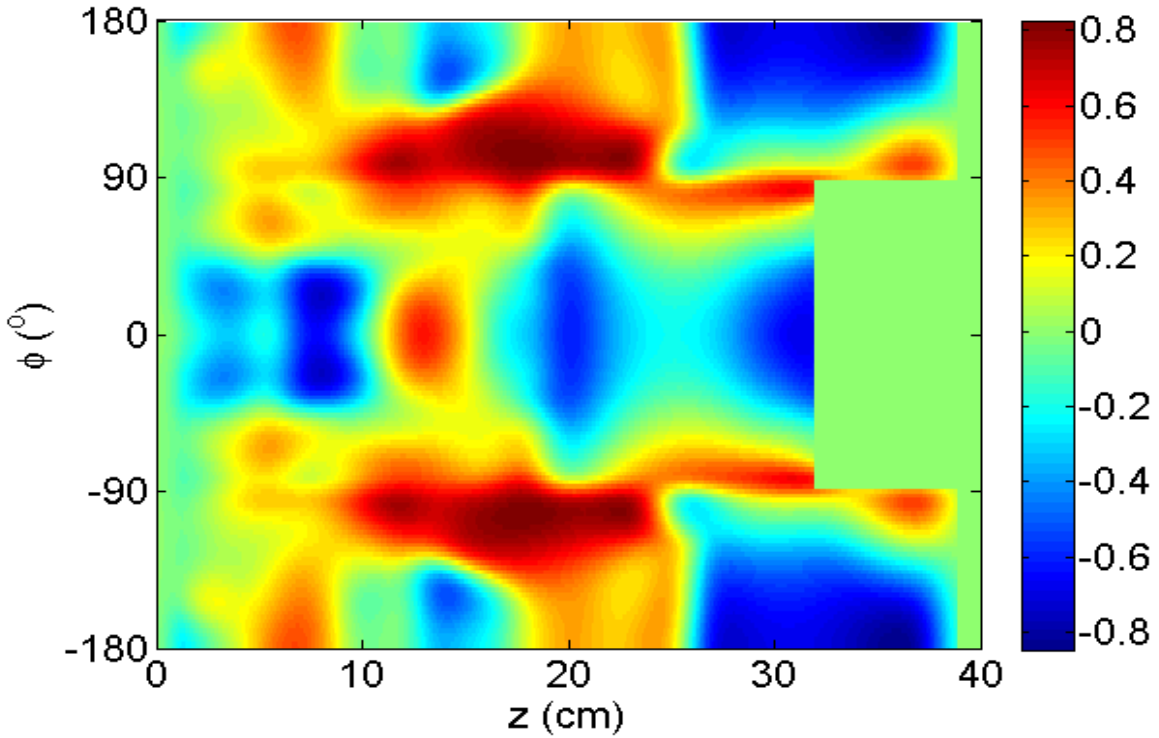

Figure 6.2.11: Perturbation profile, $\Delta\rho(\phi, z)$ (in mm) of the PoM launcher. Positive values mean the perturbations increase the radius and negative values decrease the radius. The initial radius is 1.39 cm.

The perturbation profile of the launcher is presented in Fig. 6.2.11. The exact launcher length is 38.85 cm (the waveguide and baffle length extension were optimized) and the maximum perturbation size, $|\Delta\rho|_{max}$, is 0.84 mm (6.1% of the radius). The perturbations cannot be expressed analytically (i.e. they are numerical in nature), and their smoothness is controlled indirectly by the parameters of a low-pass Gaussian spatial filter. This perturbation profile is smooth and has no sharp edges or discontinuities to make the perturbations machinable.

Up to this point, no non-idealities were factored into the perturbed-wall PoM launcher output radiation pattern. Two of these crucial non-idealities are the fabrication process tolerances and the gyrotron output frequency drift. Typical fabrication tolerances for launchers are in the range of 0.5 μm to 1 μm. The perturbed-wall PoM launcher and other launchers simulated throughout this dissertation neglect this fabrication tolerance requirement; the perturbation profile is modeled to more significant figures than the fabrication tolerance. Furthermore, the perturbation profile was designed and optimized for only a single-frequency operation, and it is not uncommon for the gyrotron output frequency to fluctuate throughout its operation. For gigahertz-range gyrotrons, a frequency drift in the hundreds of megahertz is possible. One way of modeling these two non-idealities is to simulate the launcher at different operating frequencies. Apart from directly modeling the gyrotron output frequency drift, changing the launcher operating frequency also indirectly models the fabrication tolerances to some extent. Recall from GO that for a fixed radius waveguide, changing the launcher operating frequency changes the axial bounce angle (θ_b) and the bounce length (L_b) of the incident mode; the rays propagating and reflecting off the perturbations are now tilted by an offset axial bounce angle $(\Delta\theta_b)$ and shifted in the axial direction by an offset bounce length (ΔL_b), resulting in poorer output radiation beam patterns. For longer launchers (i.e. launchers that are several Brillouin zones long and not in terms of the absolute launcher length), the effects of these offset tilts and lengths would accumulate, leading to worse off results.

Figures 6.2.12 and 6.2.13 show the far-field co-polarization patterns from Surf3d of the perturbed-wall PoM launcher operating at frequencies of 57 GHz and 63 GHz respectively, and these figures are meant to represent the effects of the non-idealities (i.e. fabrication tolerances and gyrotron output frequency drift) on the launcher performance. From GO, for a fixed radius waveguide, a ±5% change in the operating frequency (i.e. a ±3 GHz frequency difference from the original 60 GHz launcher operating frequency) is equivalent to an offset axial bounce

angle $(\Delta\theta_b)$ of $\pm1.25^o$ (or $\pm5.28\%$ of θ_b) and an offset bounce length (ΔL_b) of ±0.792 cm (or $\pm6.25\%$ of L_b). The

far-field co-polarization values of Figs. 6.2.12 and 6.2.13 are summarized and presented in Table 6.2.3.

Table 6.2.3: Summary of the Far-field Co-polarization Values of the Perturbed-wall PoM Launcher at Different Operating Frequencies.

Operating Frequency (GHz)	Power in Main Lobe	10 dB Angular Spread		Polar Exit Angle
		Azimuthal, $\Delta\phi$	Polar, $\Delta\theta$	
57	$> 99.5\%$	94.3^o	14.9^o	24.8^o
60	$> 99.5\%$	91.2^o	14.3^o	23.5^o
63	$> 99.5\%$	87.7^o	15.7^o	22.3^o

Figures 6.2.12 and 6.2.13, and Table 6.2.3 all show that the output radiation pattern is only slightly affected

by the change in operating frequency. At 57 GHz and 63 GHz, nearly all of the power is still in the main lobe, and

the side lobes remain small. As predicted by GO, the main lobe is slightly shifted and distorted in the polar direction

when the operating frequency is changed. From Fig. 6.2.12, the main lobe is shifted downwards in the polar

direction, and this is because the axial bounce angle has reduced. Similarly for Fig. 6.2.13, the main lobe is shifted

upwards in the polar direction due to the increase in the axial bounce angle. The change in the polar exit angle does

not appear to agree with GO (e.g. at 57 GHz, the bounce angle is reduced but the polar exit angle is increased), but

this is not a cause for concern because this polar exit angle value is not well defined when the peak of the main lobe

is rather flat, as they are in these cases. The other parameters (e.g. azimuthal and polar angular spread) at the 57 GHz

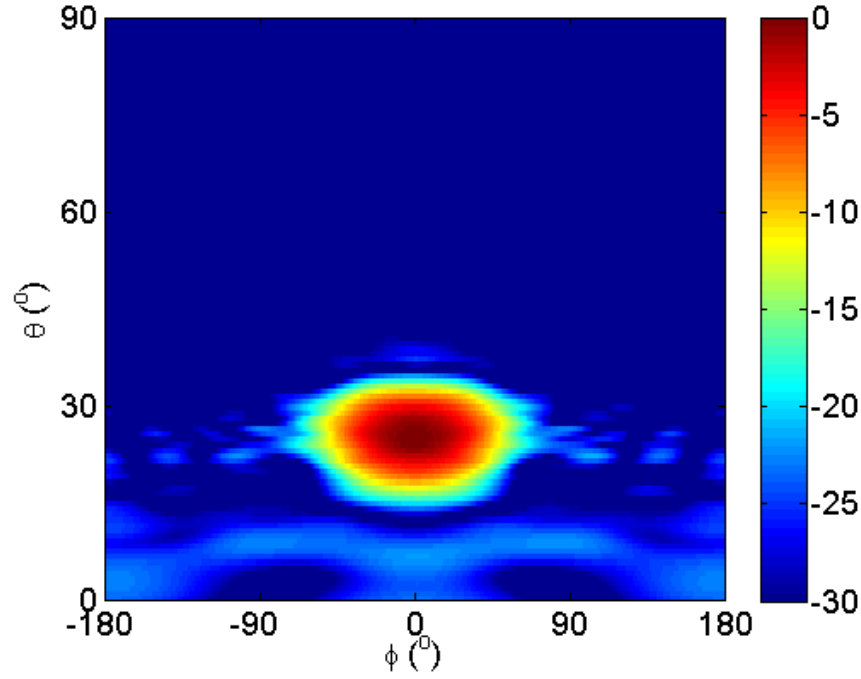and 63 GHz operating frequencies are still considered good.

Figure 6.2.12: The far-field pattern of $|E_\phi|$ (co-polarization) of the perturbed-wall PoM launcher operating at 57 GHz (in dB) obtained from Surf3d.
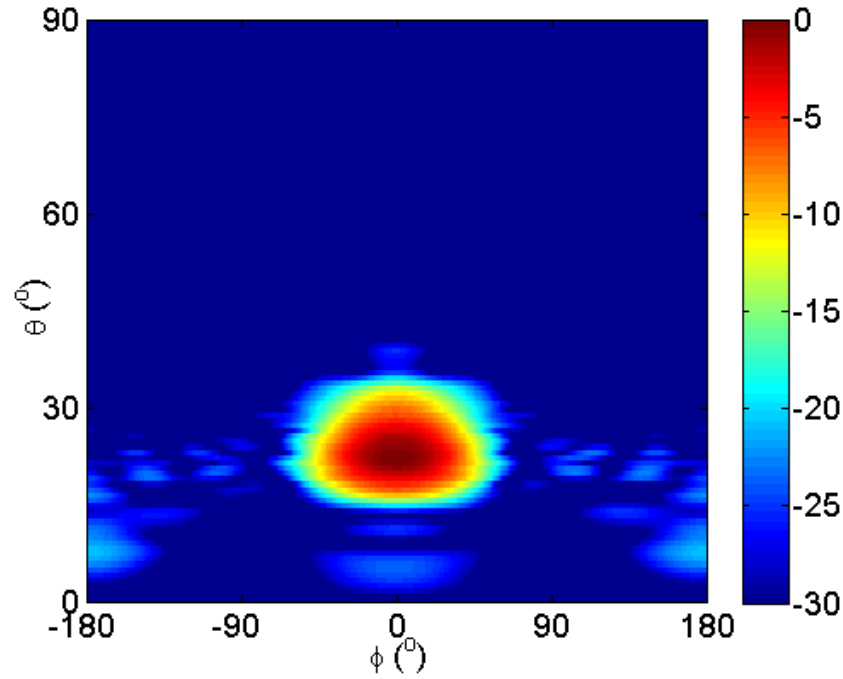

Figure 6.2.13: The far-field pattern of $|E_\phi|$ (co-polarization) of the perturbed-wall PoM launcher operating at 63 GHz (in dB) obtained from Surf3d.

6.3 The perturbed-wall PoM launcher mirror system

A two-mirror system was designed for this perturbed-wall PoM launcher by Ben Rock [20] [28]. These roughly toroidal mirrors transform the elliptical Gaussian beam from the launcher into a circular Gaussian beam for input into a 6.35 cm diameter corrugated waveguide. These mirrors also have perturbations that improve the quality of the output circular Gaussian beam. The side view of the co-polarization of this whole system, $\left|E_y\right|$ along the center symmetry plane is displayed in Fig. 6.3.2. The total output of the co-polarization of the whole system, $\left|E_x{'}\right|$ on a tilted plane is presented in Fig. 6.3.1, with a complex scalar Gaussian coupling (to $E_x{'}$), c_{cs} of 99% and a complex vector Gaussian coupling (to $\mathbf{E}$), c_{cv} of 98.3%.
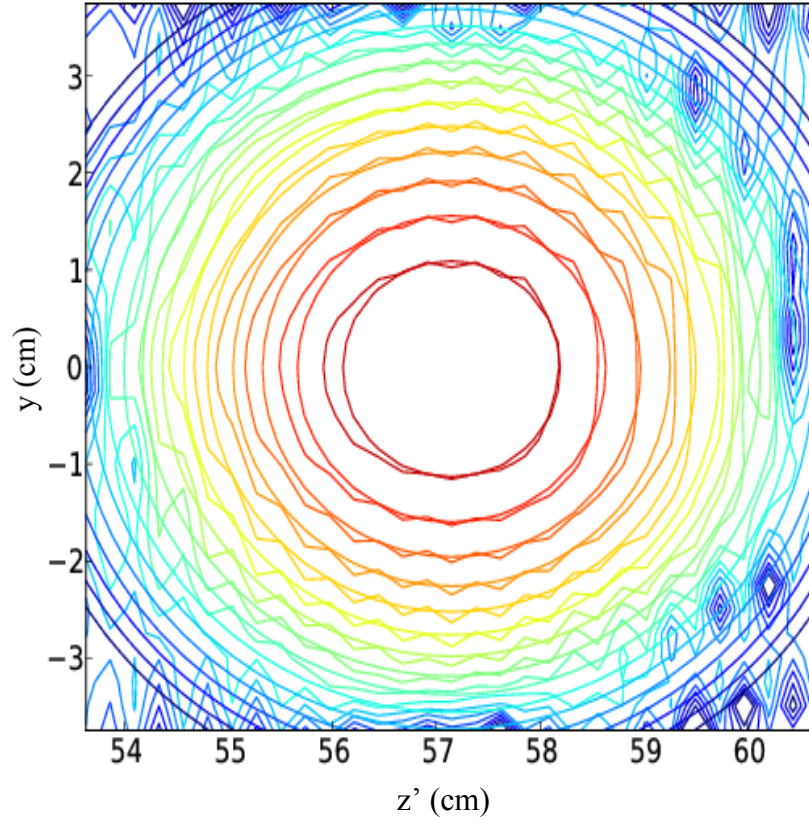

Figure 6.3.1: Contour plots of the output co-polarization $\left(\left|E_x{'}\right|\right)$ of the total system from Surf3d. The contours are in -3 dB increments. The plot is on a tilted planar surface (y and z' coordinate system) where the beam propagation is normal to it. The ideal target circular Gaussian beam is overlaid on the same surface.
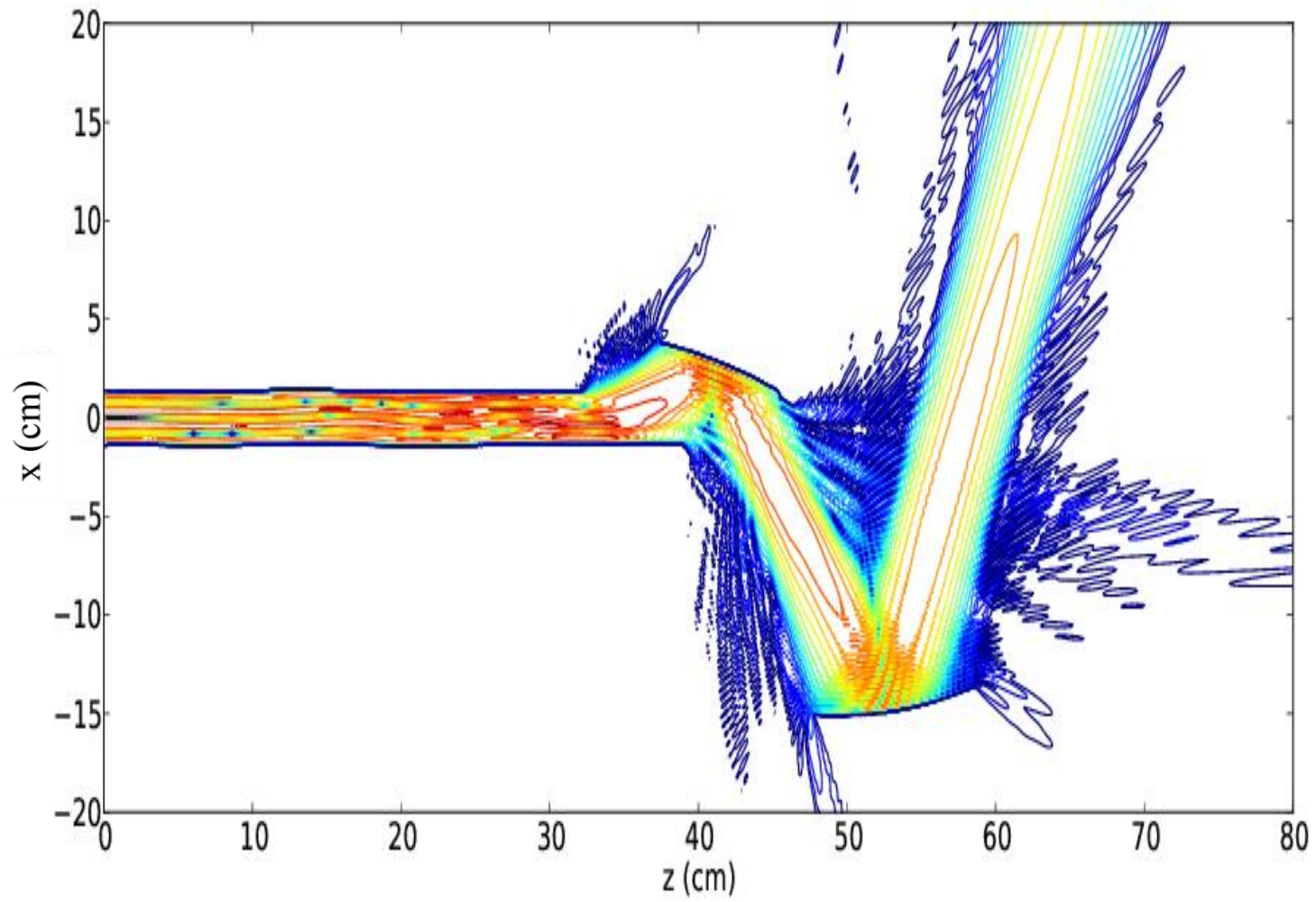
Figure 6.3.2: Contour plots of the side view $\left(\left|E_y\right|\right)$ of the whole system along the center symmetry xz plane from Surf3d. The contours are in -3dB increments.

6.4 Results and discussion for the perturbed-wall HSX launcher

The method described in this thesis can improve the output of the launcher used by HSX at UW Madison. Power is generated by a gyrotron, and a transmission line (which consists of a TE_{02} QOMC system, circular waveguides, corrugated waveguides and miter bends) connects the gyrotron window to the HSX window. The QOMC is considered as part of the transmission line only for this HSX system; typically this is not the convention. HSX is currently connected to two different gyrotrons through two different transmission lines; these two gyrotrons differ only in the amount of power level produced. For the first gyrotron and transmission line, 160 kW of maximum power is estimated at the gyrotron window, but only 100 kW is measured at the HSX window [13]. For the second gyrotron and transmission line, 70 kW of power is measured at the gyrotron window, and only 45 kW is measured at the HSX window [13]. The second transmission line has less loss because it is shorter and has fewer bends. More about this HSX transmission line is covered in the next section. A lot of the power is lost through the transmission line, and most of that power loss is projected to be from the QOMC system. One way of reducing this power loss is by designing a new perturbed-wall TE_{02} launcher to replace the current smooth-wall launcher.

There are some inherent problems with designing a new perturbed-wall launcher for the HSX transmission line. Although this HSX launcher is located externally, the large bounce length of this launcher (L_b = 15.62 cm) necessitates that the launcher length be small to moderate in terms of Brillouin zones (the rest of the launcher parameters is listed in Table 2.2.1). A launcher that is too long (in absolute length) might be prohibitively expensive. Furthermore, the fact that this launcher is more oversized (2.66 OF) than the PoM launcher also makes its design more difficult.

A new perturbed-wall HSX launcher was designed, with a length of 62.49 cm (corresponding to three and a half Brillouin zones) with a maximum perturbation size of 12.82% of the radius. Figures 6.4.1 and 6.4.2 show the co-polarization of the far-field from the smooth-wall and perturbed-wall launcher respectively, and the differences are listed in Table 6.4.1. (the side lobes attached to the main lobe, as in Fig. 6.4.2, are excluded from the main lobe calculation). The far-field of the smooth-wall launcher shares similar problems as the smooth-wall PoM launcher (Section 6.1) and will not be restated again. The perturbed-wall launcher does not radiate a good Gaussian beam with minimal side lobes because the launcher length is not long enough. As displayed in Table 6.2.1, the polar exit
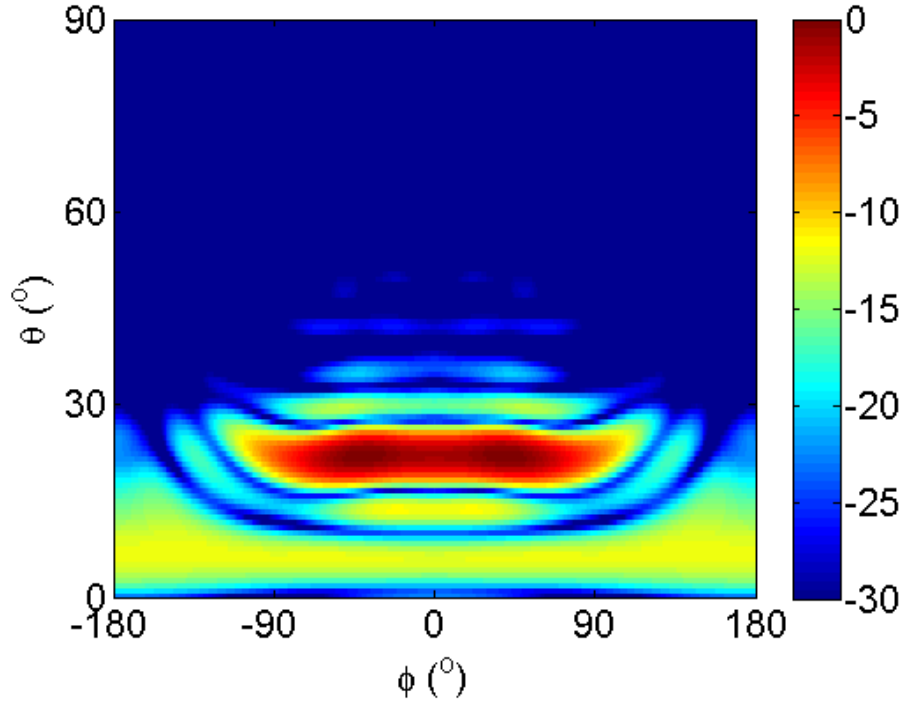
Figure 6.4.1: The far-field pattern of $\left|E_\phi\right|$ (co-polarization) of the current smooth-wall HSX launcher (in dB) obtained from Surf3d.
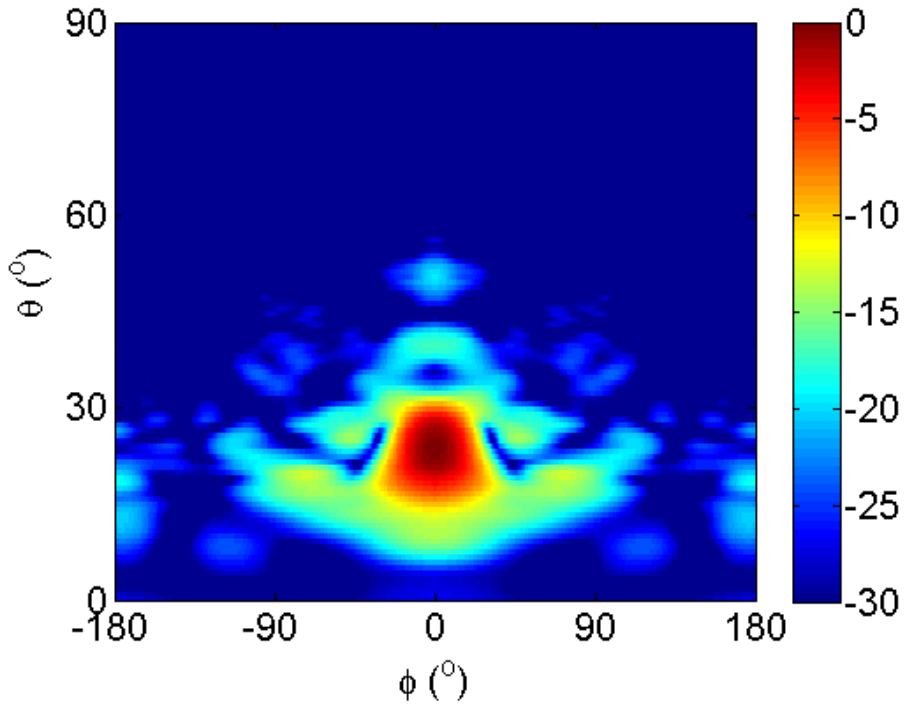

Figure 6.4.2: The far-field pattern of $\left|E_\phi\right|$ (co-polarization) of the perturbed-wall launcher (in dB) for possible use in HSX obtained from Surf3d.

Table 6.4.1: Summary of the Far-field Comparison between the HSX Launchers.

Launcher	Co-polarization (E_ϕ)					Cross-polarization (E_θ)	
	Polar Exit Angle	Power in Main Lobe	Directivity, D_ϕ	10 dB Angular Spread		$\lvert E_\theta \rvert_{max}$	Total Power
				Azimuthal, $\Delta\phi$	Polar, $\Delta\theta$		
Smooth-wall	23.1°	77.53%	21.4 dBi	205.8°	9.1°	-21.4 dB	< 0.01%
Perturbed-wall	24.0°	87.61%	24.4 dBi	63.14°	16.5°	-20.6 dB	< 0.01%

angle changes slightly when perturbations are added. This should not be a cause of concern because the polar exit angle is simply taken as the polar angle of the main lobe maximum/maxima. This value is not well defined when the spread of the peak of the main lobe is rather flat (more than 5° from Fig. 6.4.2). The perturbations have improved the percent of power in the main lobe by 10%, and the directivity is also boosted by 3 dB. The azimuthal angular spread is lowered to less than half, but the polar spread is increased by roughly 8°. The cross-polarization values remain negligibly low. The perturbation profile is shown in Fig. 6.4.3, and the near-field cylindrical scans of the perturbed-wall launcher at the output aperture and after the launcher cut is displayed in Fig. 6.4.4.
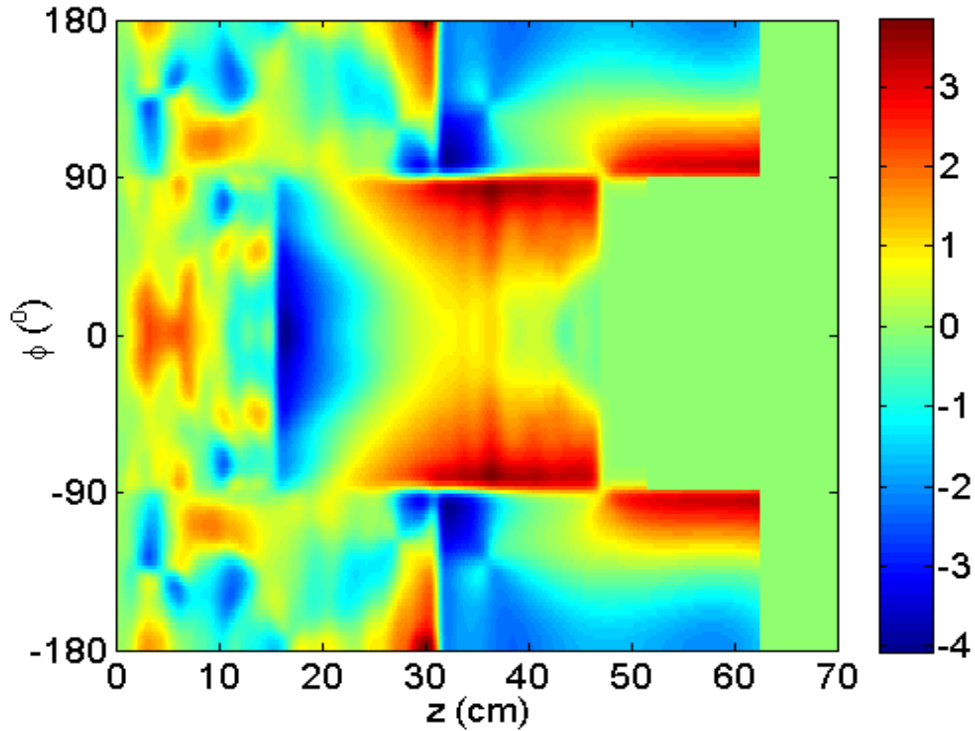

Figure 6.4.3: Perturbation profile, $\Delta\rho(\phi, z)$ (in mm) of the HSX launcher. Positive values mean the perturbations increase the radius and negative values decrease the radius. The initial radius is 3.175 cm.
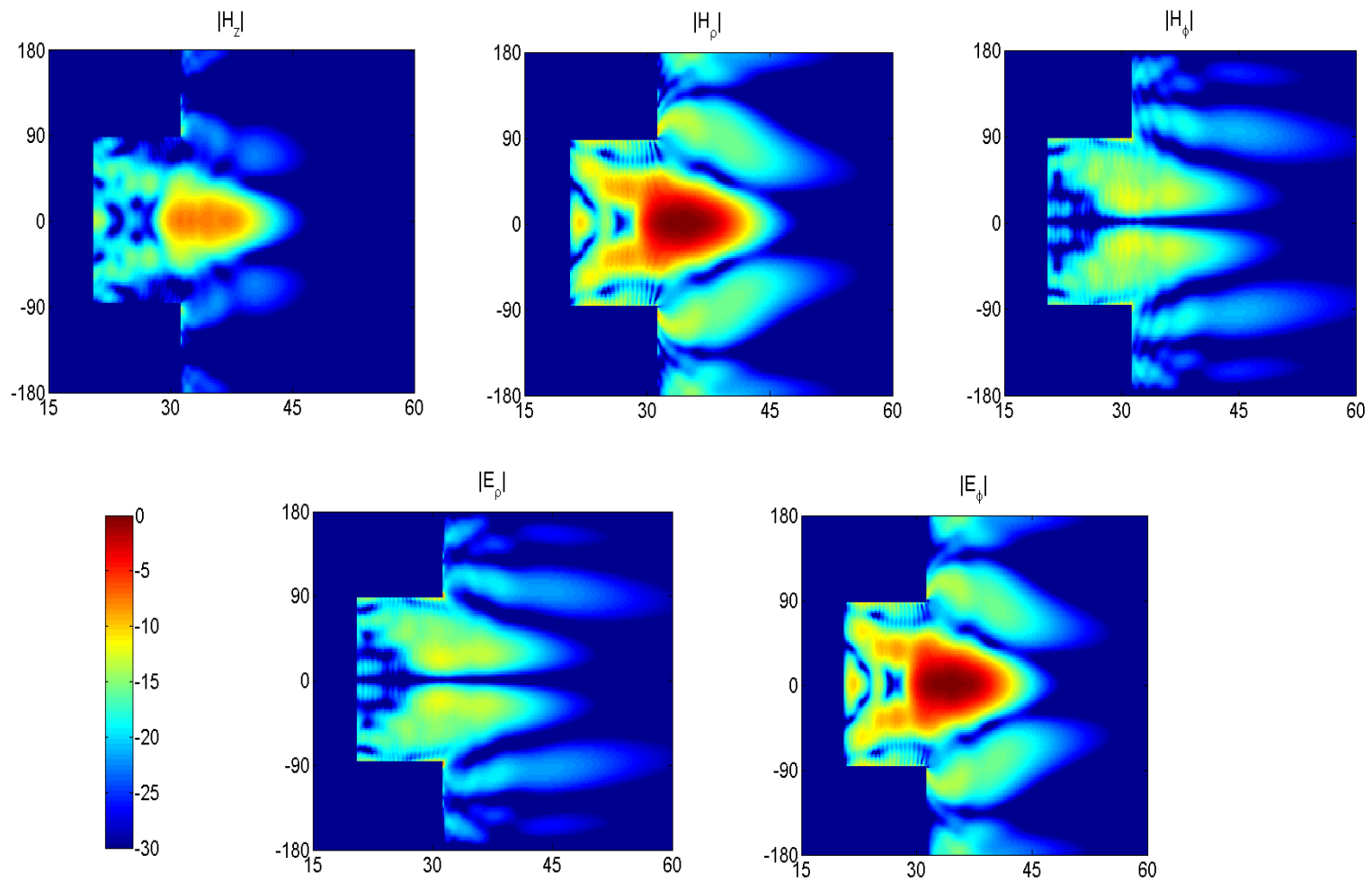
Figure 6.4.4: All field components at the output aperture and after the launcher cut (in dB) for the perturbed-wall HSX launcher obtained from Surf3d. (Fields on the launcher walls are blanked out because Surf3d does not give accurate values there). The vertical axes are ϕ (°) and the horizontal axes are z (cm).

The $\left| E_z \right|$ field is not shown because it is negligible ($\left| E_z \right| < $ -30 dB).

6.5 The HSX transmission line

A schematic diagram of the first HSX transmission line is displayed in Fig. 6.5.1. For now, the transmission line is only modeled past the parabolic mirror for both the smooth-wall and perturbed-wall launchers using Surf3d, and these simulations were done by Eric Buscarino. In future simulations, there are plans to partially model the system up to the entrance of the dual-mode waveguide. The parabolic mirror was designed using GO, and it was estimated that the total power efficiency of the Vlasov mode converter subsystem is 83% [13]. This subsystem also functions to filter out the gyrotron spurious modes because these modes have different beam propagation parameters.
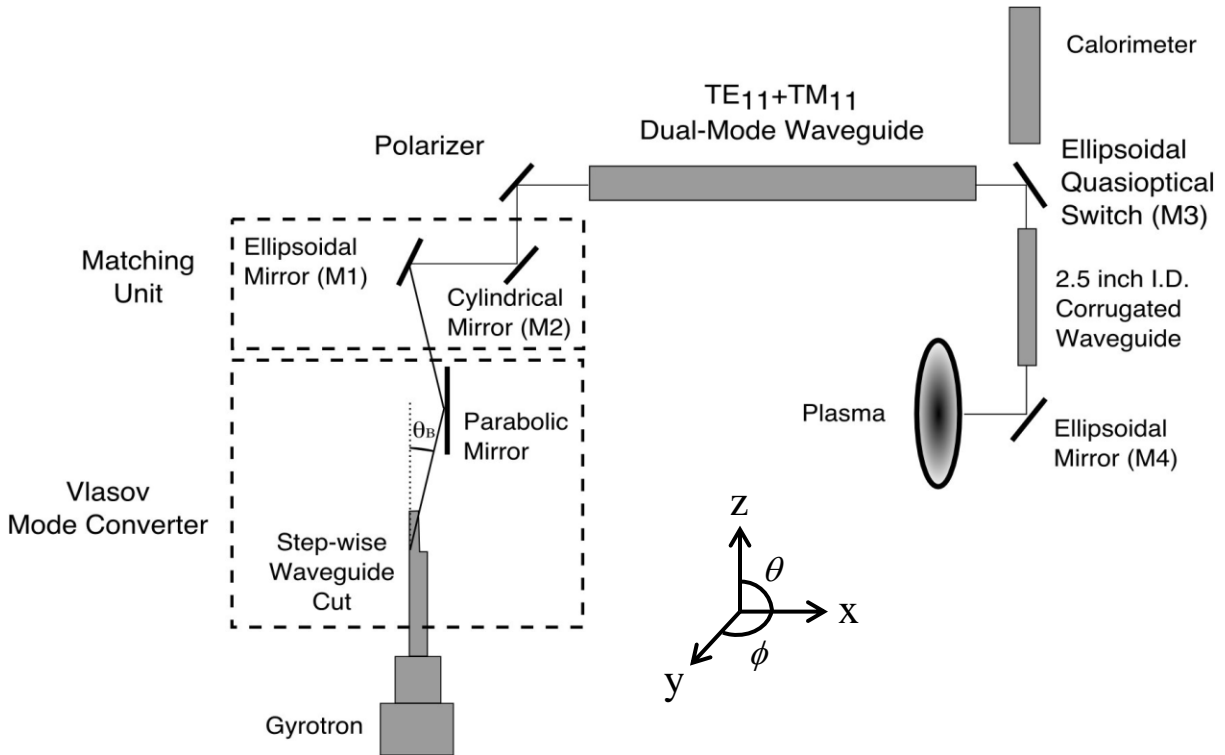

Figure 6.5.1: Schematic diagram of the first HSX transmission line [13].

Figures 6.5.2 and 6.5.3 show the co-polarization of the far-field pattern from the parabolic reflector following the smooth-wall and perturbed-wall HSX launcher respectively. A summary of some of these far-field values is provided in Table 6.5.1. The parabolic reflector focusses the beam in the ϕ direction and this effect can be seen by the reduction of the azimuthal angular spread, from 205.8^o to 101.0^o for the smooth-wall launcher, and from 63.14^o to 41.0^o for the perturbed-wall launcher. This focusing effect also increases the directivity of the radiation pattern, by 4.3 dB for the smooth-wall launcher and 1.4 dB for the perturbed-wall launcher. A better picture of the
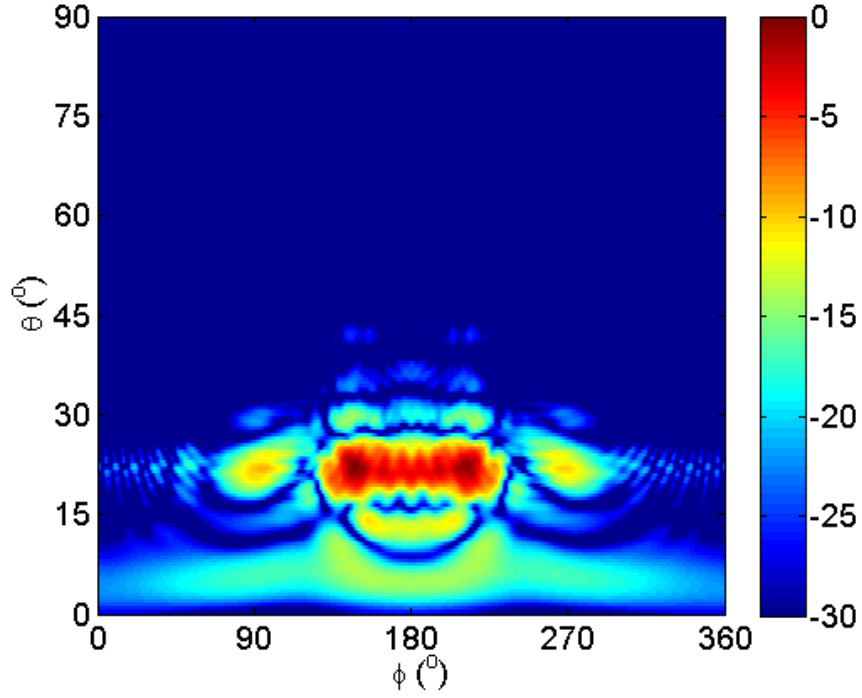
Figure 6.5.2: The far-field pattern of $|E_\phi|$ (co-polarization) from the parabolic reflector following the smooth-wall HSX launcher (in dB) obtained from Surf3d.
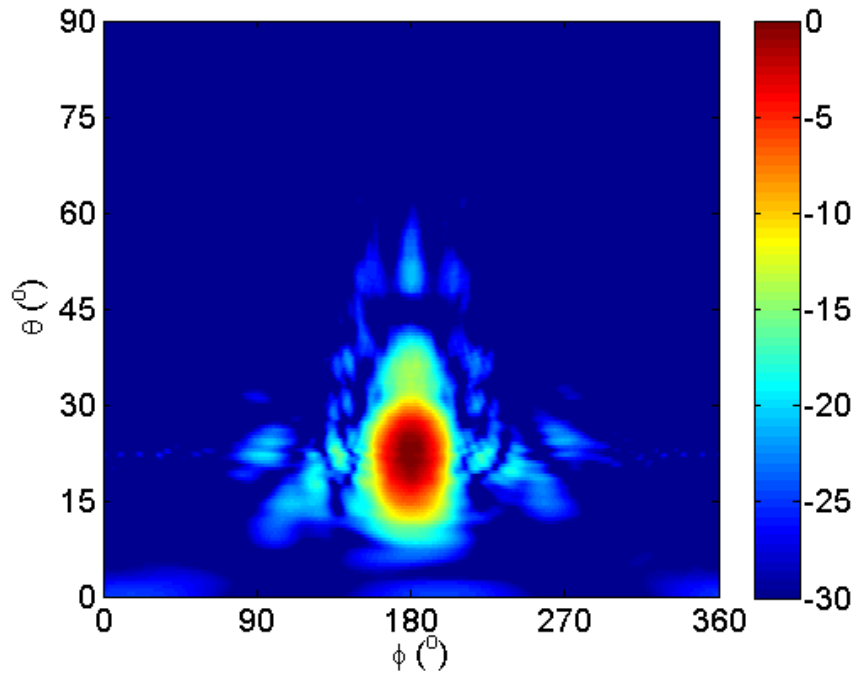

Figure 6.5.3: The far-field pattern of $|E_\phi|$ (co-polarization) from the parabolic reflector following the perturbed-wall HSX launcher (in dB) obtained from Surf3d.

improvement in the radiation pattern of the perturbed-wall over the smooth-wall HSX launcher is provided in the percent of power in the main lobe value (Table 6.4.1 vs. Table 6.5.1). For the smooth-wall launcher, this value actually goes down from 77.53% to 73.44% because although the parabolic reflector is large, there is still a portion of the main lobe (in the ϕ direction) that misses this mirror. This problem is not shared by the perturbed-wall launcher, in fact the percent of power in the main lobe has increased. This is due to, 1) the main lobe is fully captured by the parabolic reflector, and 2) the spread of the main lobe (and some of the side lobes attached to it) has been shrunk, focusing more power into the main lobe (Figs. 6.4.2 and 6.5.3). The side view of the launcher and parabolic reflector for the smooth-wall and perturbed-wall launchers is respectively displayed in Figs 6.5.4 and 6.5.5.

Table 6.5.1: Summary of Some Far-field Co-polarization (E_ϕ) Values from the Parabolic Reflector Following the Launchers.

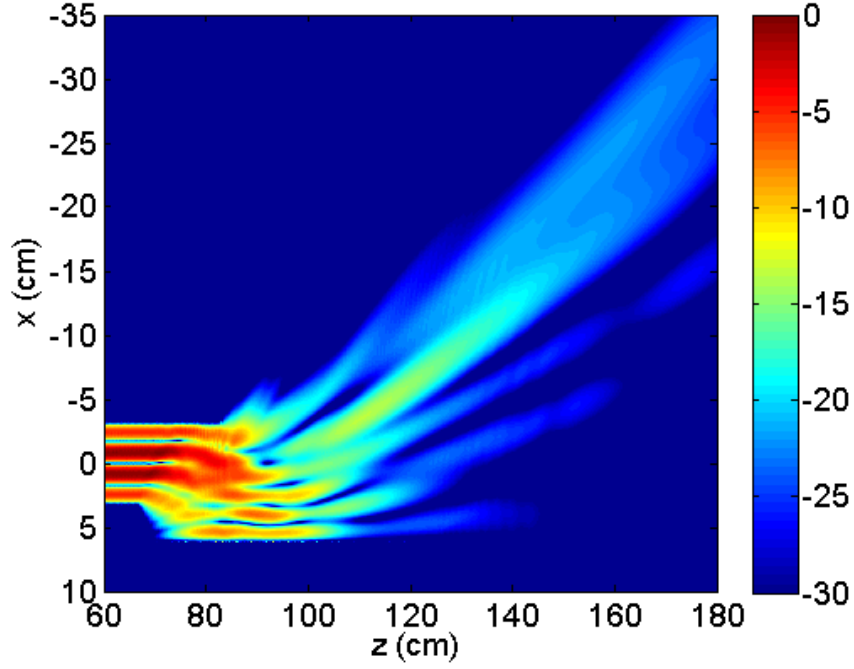| Launcher	Power in Main Lobe	Directivity, D_ϕ	10 dB Angular Spread	
			Azimuthal, $\Delta\phi$	Polar, $\Delta\theta$
Smooth-wall	73.44%	25.7 dBi	101.0$^{\text{o}}$	8.5$^{\text{o}}$
Perturbed-wall	94.84%	25.9 dBi	41.0$^{\text{o}}$	17.5$^{\text{o}}$

Figure 6.5.4: Side view $\left(\left|E_y\right|\right)$ of the smooth-wall launcher and parabolic reflector along the center symmetry xz plane (in dB) obtained from Surf3d.
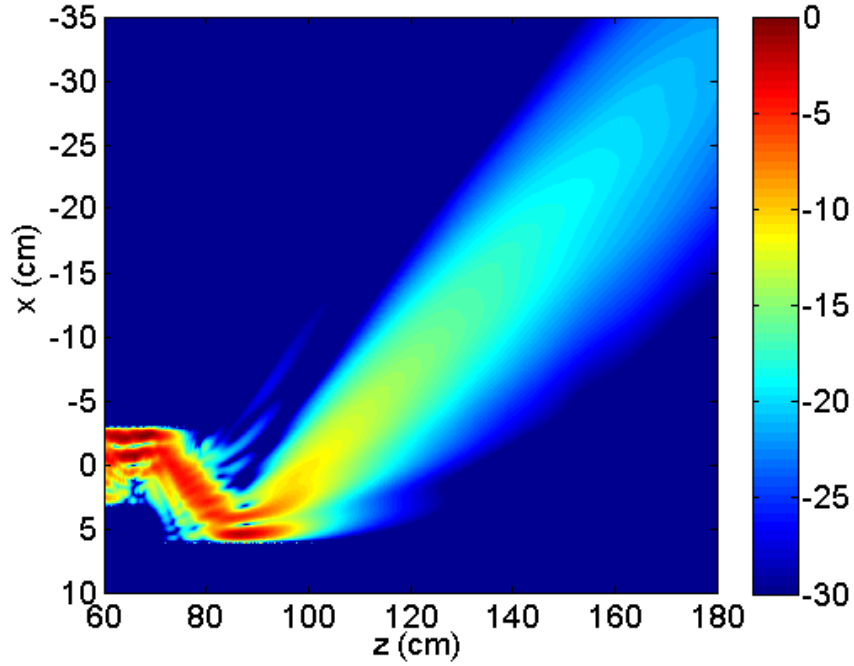

Figure 6.5.5: Side view $\left(\left|E_y\right|\right)$ of the perturbed-wall launcher and parabolic reflector along the center symmetry xz plane (in dB) obtained from Surf3d.

Chapter 7: A Compact TE$_{02}$ Launcher Design

The design of compact perturbed-wall launchers will be explored in this chapter. Launchers are typically comprised of the equivalent of five or more Brillouin zones so that a reasonable Gaussian beam (with low side lobes) output radiation pattern can be achieved. In certain circumstances, such as spatial restrictions, fabrication limitations or financial constraints, launchers are limited to one to three Brillouin zones (or even less) in length, and these types of launchers will be called short/compact launchers. In principle, a compact launcher is defined only as a launcher that is relatively short in terms of Brillouin zones, and not in terms of the absolute launcher length, L, or the wavelength, λ, or the guide wavelength, λ_g. These launchers will definitely not produce the best output radiation pattern (high Gaussian content and low side lobes) because of its short length, however, its output radiation pattern would still be an improvement over the smooth-wall launcher. A compact perturbed-wall TE$_{02}$ launcher was designed for a gyrotron in an ADS for a group at the University of California - Davis. Because this is a compact gyrotron, there is only a limited amount of internal space to house the launcher and mirror system. This ADS launcher has a radius of 0.55 cm and operates at 94 GHz (1.54 OF), and its length is limited to only 3.9 cm, corresponding to two and a half Brillouin zones (see Table 2.2.1).

7.1 Field calculation at the output aperture and after the launcher cut

In general, the ISC method can only accurately model the fields on the launcher walls [20] [40] and not at the output aperture or after the launcher cut. For this research, modeling the output aperture and regions after the launcher cut is done by simply setting the window function to zero at these areas. Other launcher design or analysis methods follow the same approach [21] [23] [26]. This approach is roughly akin to including only the outgoing field component, and excluding the incoming field component in the field calculation at these locations. It is only an approximation (not an exact equivalence), and under certain circumstances, it proves to be highly accurate. Without going into too much detail, one way to fully and accurately calculate the fields at the output aperture and after the launcher cut is by employing direct point-to-point numerical integration techniques instead of relying on FFTs.

The ISC method can accurately calculate the fields at the output aperture and after the launcher cut when the magnitude of the fields at the launcher boundaries are small (approximately -15 dB), so as to minimize the field discontinuity at the launcher boundary. This stipulation is met in well-designed launchers (that produce good Gaussian beams with minimal side lobes) like the PoM launcher, but not in smooth-wall or short/compact perturbed-wall launchers because the magnitude of the fields at the launcher boundary is still relatively high. A clear example of this can be seen by comparing the radiation pattern of a smooth-wall launcher from the ISC method and a different method, like Surf3d. Figures 7.1.2 and 7.1.3 display the field patterns at the output aperture and after the launcher cut for a smooth-wall launcher using Surf3d and the ISC method respectively. Diffraction at the launcher edge is neglected because both methods do not model diffraction. Both figures look similar, but they are definitely not the same. Just comparing the co-polarization (E_ϕ) patterns of both Figs. 7.1.2 and 7.1.3, it can be seen that:

1) For the main lobe, both plots show a roughly constant distribution across the output aperture (i.e. output Brillouin zone), which is consistent with GO. The Surf3d simulation shows a two-bump pattern in the main lobe, and the ISC calculation faintly shows a similar occurrence. The left bump in the Surf3d plot also stretches longer in the ϕ direction, up to the launcher edge. This approach of zero-setting the window function to model the cut in the ISC method renders the field values near the launcher edge to be less accurate, as seen in the ISC plot where the maximum field value (0 dB) does not occur at the launcher boundary. As stated earlier, this problem only occurs when the field values at the launcher boundaries are not small.

2) For the side lobes, both plots also show a large side lobe at the $\phi = 180^\circ$ position of the baffle, with the Surf3d plot showing a higher and more spread out side lobe distribution. Furthermore, the side lobes in the Surf3d plot extend much farther in the longitudinal, z , direction. The way the incident field is sourced in the ISC method, fields would not extend longer than one bounce length, L_b ,(approximately) from the launcher in the longitudinal direction, and this is confirmed by the ISC plot.

Other researchers claim that this approach of modeling the cut is accurate for smooth-wall launchers [21], but as can be seen in Figs 7.1.2 and 7.1.3, it is not so. However, this approach does prove useful in getting a general overall picture of how the radiation pattern from a smooth-wall launcher should look like, despite its limitations. The far-field co-polarization pattern of this smooth-wall launcher is shown in Fig. 7.1.1, and it shares similar problems (e.g. too large of a polar spread and not enough power in the main lobe) as the smooth-wall PoM launcher (Section 6.1).
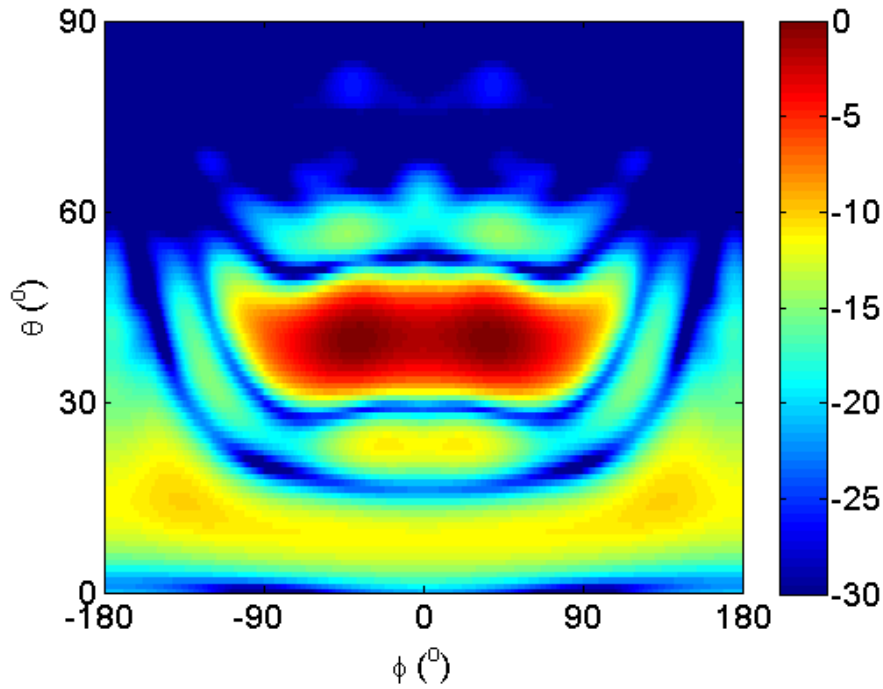

Figure 7.1.1: The far-field pattern of $\left|E_\phi\right|$ (co-polarization) of the smooth-wall ADS launcher (in dB) obtained from Surf3d.

Figure 7.1.2: Magnitude of the field components from the smooth-wall ADS launcher at the launcher output aperture and after the launcher cut (in dB) from Surf3d. (Fields on the launcher walls [and a few cells away] are blanked out because Surf3d does not give accurate values there). The vertical axes are ϕ (^{o}) and the horizontal axes are z (cm). The $\left| E_z \right|$ is not shown because it is small (less than -30 dB).
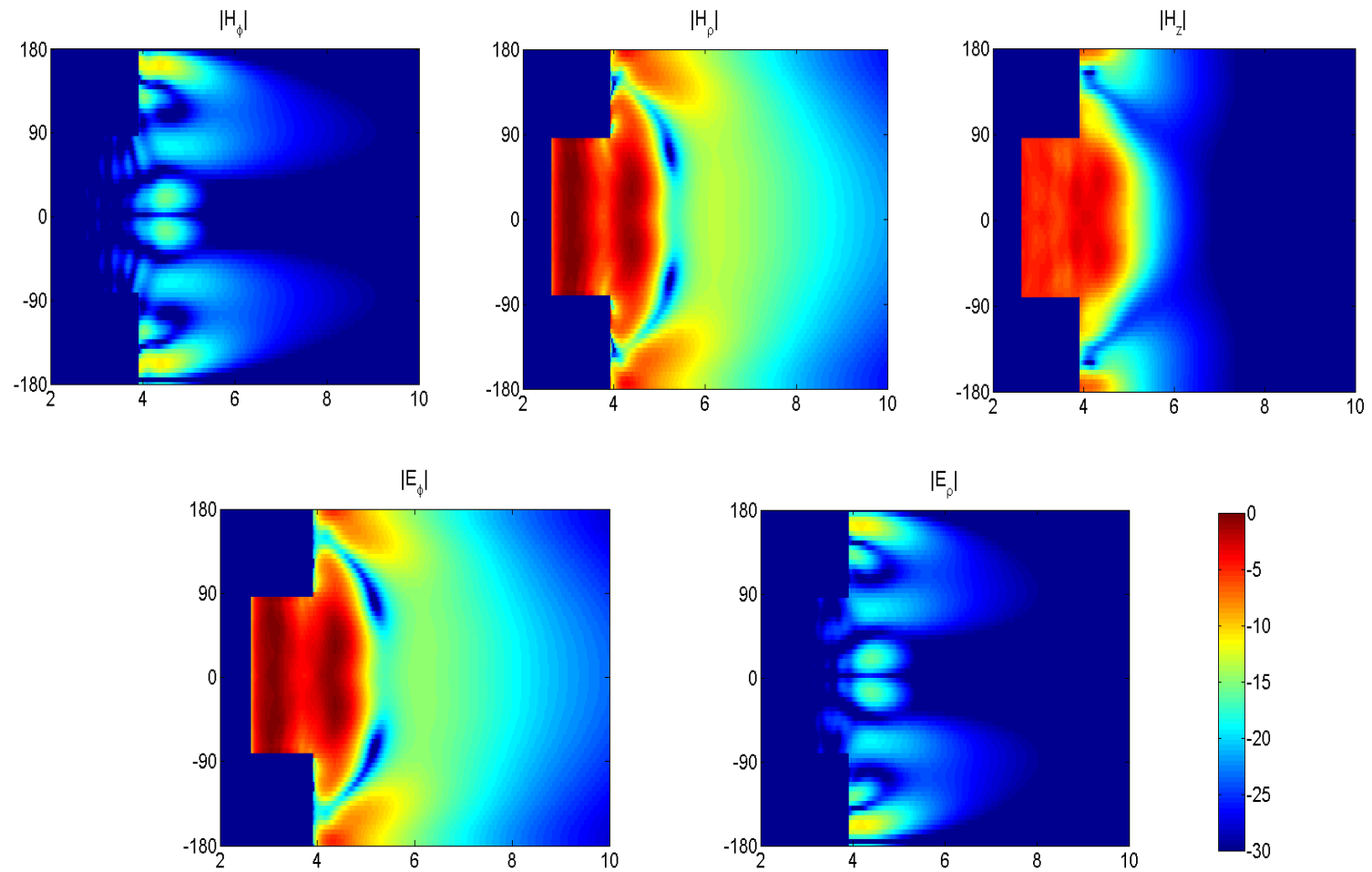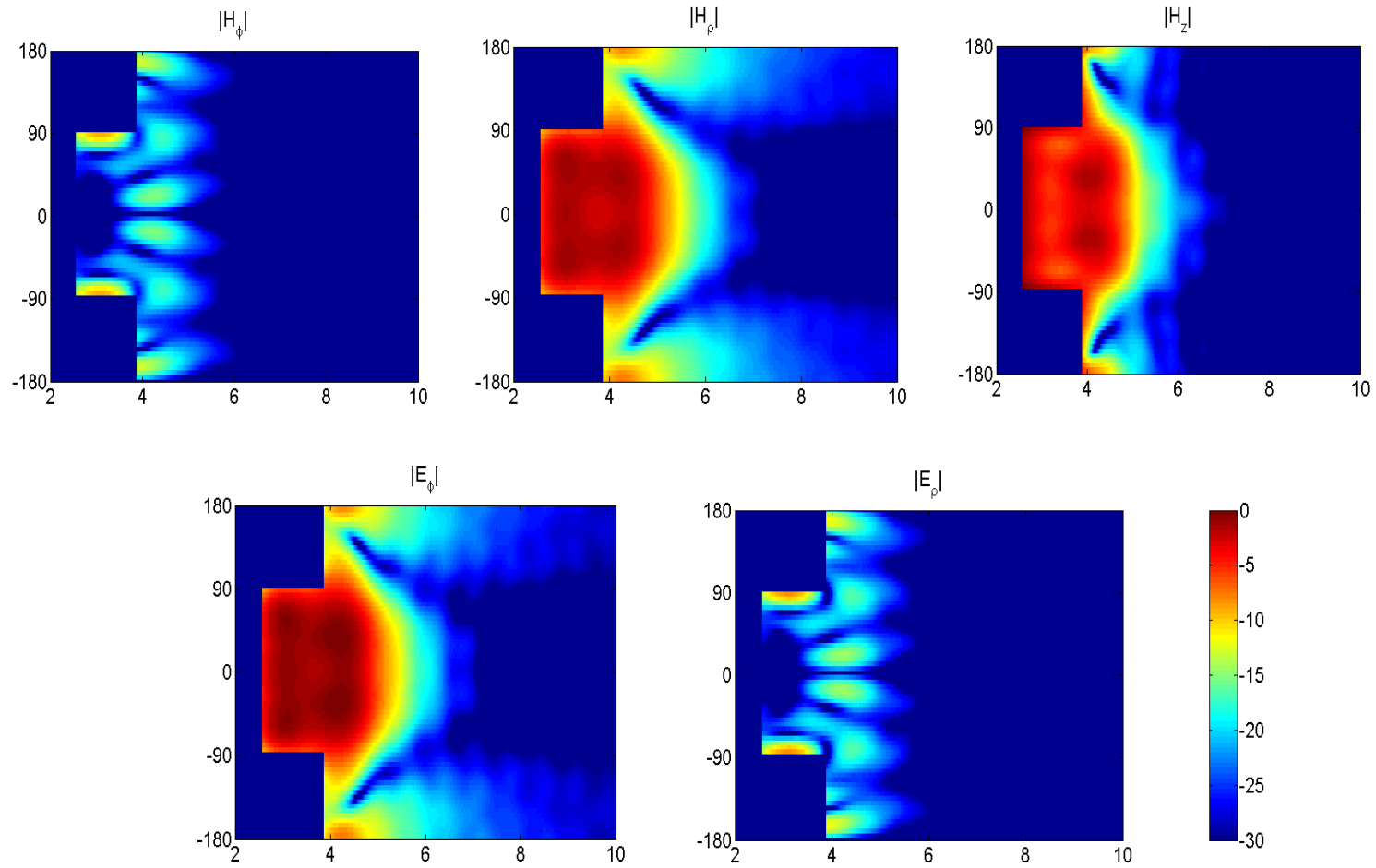
Figure 7.1.3: Magnitude of the field components from the smooth-wall ADS launcher at the launcher output aperture and after the launcher cut (in dB) from calculation. (Fields on the launcher walls are blanked out for comparison purposes with Fig. 7.1.2). The vertical axes are ϕ (^{o}) and the horizontal axes are z (cm).

7.2 Results and discussion for the perturbed-wall ADS launcher

Numerous algorithmic and design parameters were optimized to obtain the best perturbation profile for the 3.9 cm long ADS launcher. The field patterns at the output aperture and after the launcher cut from both Surf3d and the ISC calculation are illustrated in Figs. 7.2.2 and 7.2.3, and the far-field co-polarization pattern is shown in Fig. 7.2.1. Comparing between the co-polarization (E_ϕ) of the near-field scans (Figs. 7.2.2 and 7.2.3), some differences in the main lobe, and in the side lobes are observed. The Surf3d plot shows a two-bump pattern in the main lobe, and the ISC calculation has only one main lobe. The left bump in the two-bump main lobe pattern from Surf3d occurs at the $\phi = 0^\circ$ location at the launcher edge, and as reasoned earlier, this method of modeling the output aperture and after the launcher cut for the ISC method doesn't give accurate results when field values at the launcher edges are not small, as is the case for this launcher. For the side lobes, the Surf3d simulation shows more and higher magnitude side lobes than the ISC calculation.
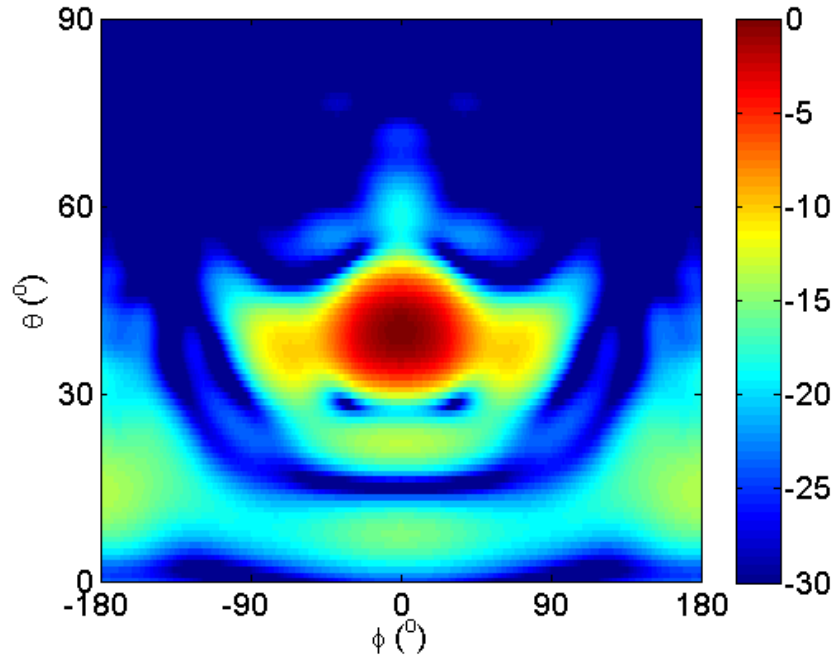

Figure 7.2.1: The far-field pattern of $\left| E_\phi \right|$ (co-polarization) of the perturbed-wall ADS launcher (in dB) obtained from Surf3d.

Figure 7.2.2: Magnitude of the field components from the perturbed-wall ADS launcher at the launcher output aperture and after the launcher cut (in dB) from Surf3d. (Fields on the launcher walls [and a few cells away] are blanked out because Surf3d does not give accurate values there). The vertical axes are ϕ (^{o}) and the horizontal axes are z (cm). The $\left| E_z \right|$ is not shown because it is small (less than -30 dB).
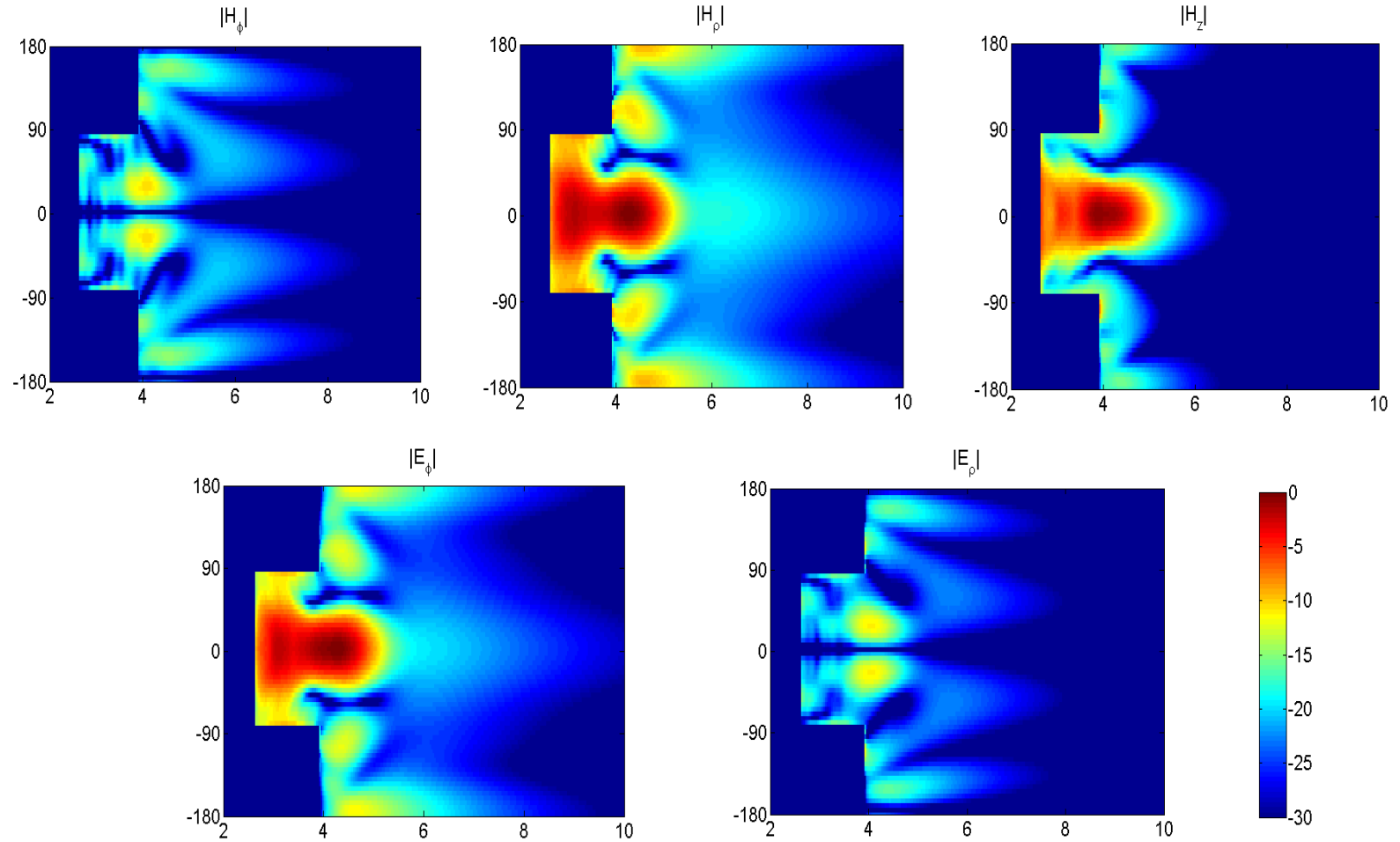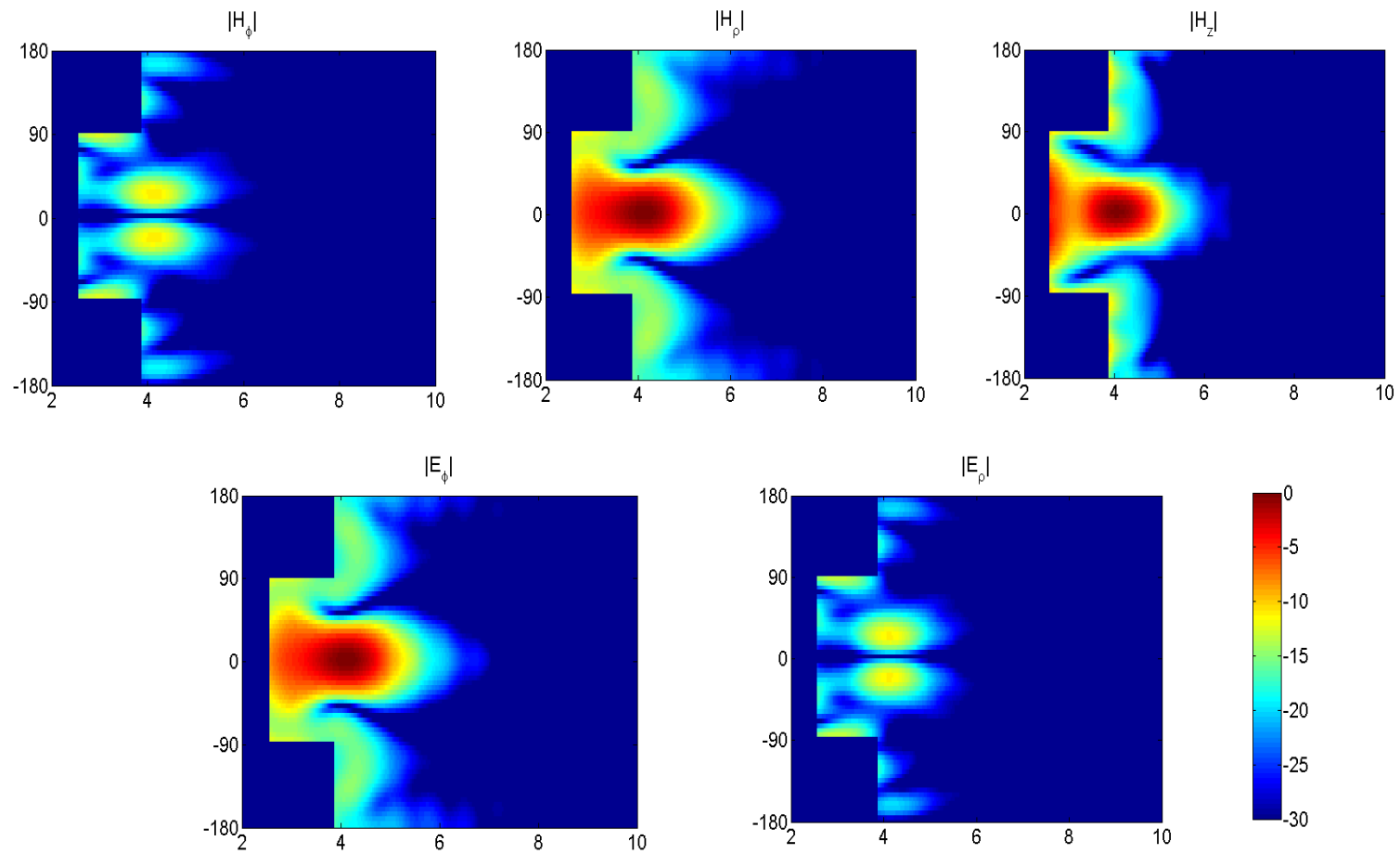
Figure 7.2.3: Magnitude of the field components from the perturbed-wall ADS launcher at the launcher output aperture and after the launcher cut (in dB) from calculation. (Fields on the launcher walls are blanked out for comparison purposes with Fig. 7.2.2). The vertical axes are ϕ (^{o}) and the horizontal axes are z (cm)

Contrasting the co-polarized far-field of the smooth-wall (Fig. 7.1.1) and perturbed-wall ADS launcher (Fig. 7.2.1), it's clear that the perturbations have improved the radiation pattern. At most, only the power in the main lobe can be collected by a conventional mirror system. Typically, side lobes have different (free space) propagation directions, and will therefore be unrecoverable by the following mirror system. Table 7.2.1 summarizes the far-field parameters of these two launchers (note that the two lateral side lobes attached to the main lobe in Fig. 7.2.1 is not considered as part of the main lobe). The application of perturbations has increased the power in the main lobe. Although Table 7.2.1 suggests an improvement of only 1.43% in the main lobe power (over the smooth-wall launcher), in reality, this percentage of power increase is misleading. The amount of power that truly counts is the amount of power in the main lobe that reaches the output window of the ADS, preferably in the form of a Gaussian beam. The percent of power in the main lobe that can actually be transferred to the output window of the ADS depends on several factors such as the quality of the main lobe, and the number and sizes of the mirrors. In this compact gyrotron, there is only place for a single mirror. For the smooth-wall ADS launcher, it is estimated that only 60 to 80 % of the power in the main lobe can be transmitted to the output window of the ADS because, 1) the main lobe is double-peaked (i.e. difficult for a single mirror to shape a double-peaked main lobe into a Gaussian beam), 2) the large azimuthal angular spread of the main lobe (in the far-field), 3) the size and shape restrictions imposed on the single mirror (i.e. the compact gyrotron has limited internal space), and 4) the size of the output window. For the perturbed-wall ADS launcher, it is estimated that more than 99% of the main lobe power can be transmitted to the output window of the ADS because its main lobe is more Gaussian and is significantly smaller in the azimuthal direction. In totality, the perturbed-wall ADS launcher is estimated to deliver approximately 20% to 33% more power to the output window compared to the smooth-wall ADS launcher. An exact quantification is difficult to calculate because these two different ADS launchers would require two different mirrors

For the perturbed-wall ADS launcher, the directivity of the main lobe is boosted by 3 dB, the azimuthal spread is shrunk by nearly half, and the rise in the polar spread is less than 1°. The polar spread increase is small because the magnitude of the field distribution along the z axis on the output aperture at the $\phi = 0^\circ$ line (i.e. the $\left| E_\phi \right|$ plot in Fig. 7.2.2) does not change greatly (compared to the smooth-wall case in Fig. 7.1.2). Recall from Section 6.2 that the far-field polar spread is the Fourier Transform of the near-field distribution along the z axis on the output aperture. Low shape reduction in this near-field distribution translates to a small increase in the far-field polar

spread. The cross-polarization changes remain negligible. The perturbation profile for the perturbed-wall ADS launcher is displayed in Fig. 7.2.4, and the maximum perturbation size, $|\Delta\rho|_{max}$, is only 9.13 % of the radius.

Table 7.2.1: Summary of the Far-field Parameters between the ADS Launchers.

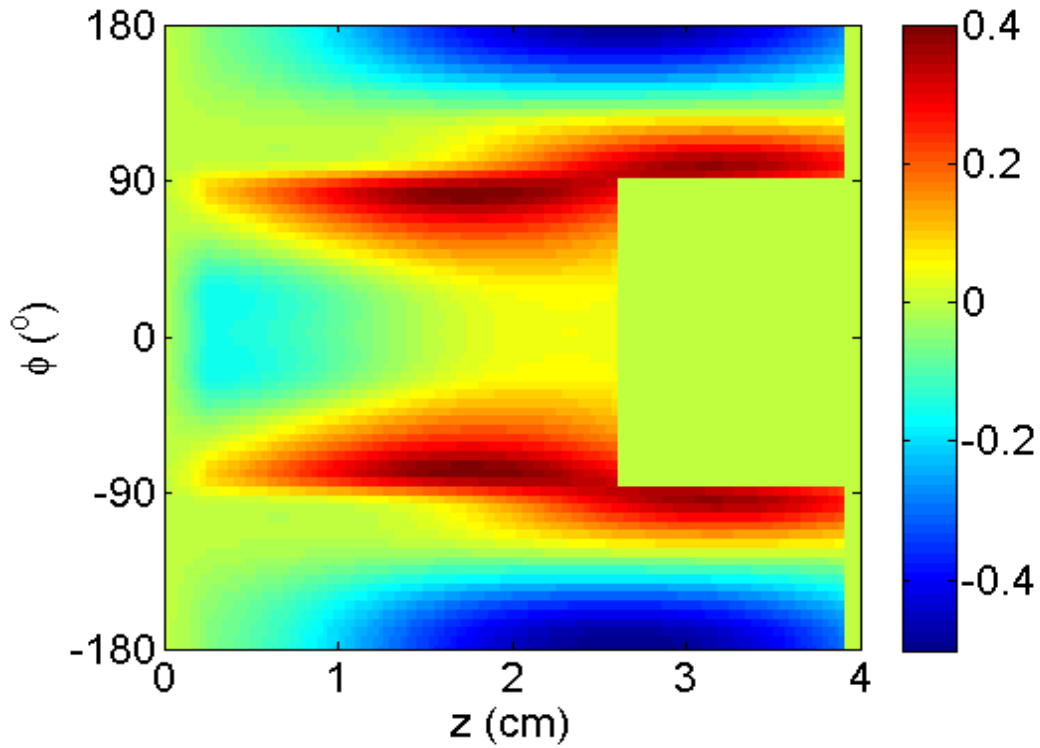| Launcher | Co-polarization (E_ϕ) | | | | | Cross-polarization (E_θ) | |
| | Polar Exit Angle | Power in Main Lobe | Directivity, D_ϕ | 10 dB Angular Spread | | | |
				Azimuthal, $\Delta\phi$	Polar, $\Delta\theta$	$|E_\theta|_{max}$	Total Power
Smooth-wall	40.2°	75.18%	16.0 dBi	203.0°	18.2°	-21.0 dB	< 0.01%
Perturbed-wall	40.2°	76.61%	19.0 dBi	106.3°	19.1°	-19.2 dB	0.45%

Figure 7.2.4: Perturbation profile, $\Delta\rho(\phi, z)$ (in mm) of the ADS launcher. Positive values mean the perturbations increase the radius and negative values decrease the radius. The initial radius is 0.55 cm.

7.3 The ADS mirror system

A single unperturbed toroidal mirror was designed by Ben Rock for this perturbed-wall ADS launcher, and the side view of this whole QOMC system is illustrated in Fig. 7.3.1. The circular output window for this compact ADS gyrotron would be located on the $x = -9$ cm plane (and centered at the $y = 0$ cm and $z = 6$ cm point), with a diameter of 4 cm. Figure 7.3.2 displays the contour plot of the $\left| E_y \right|$ field at this output plane. Most of the main lobe will pass through the circular window, except for a portion of the nose. The nose is an unavoidable high magnitude side lobe that is radiated by the perturbed-wall launcher, and it is not possible to steer it into the circular output window using the toroidal mirror. The nose can be eliminated if a longer launcher is used. The value of the field hitting the sides of the circular window is approximately -15 to -27 dB (excluding the nose), so field reflections at the boundary of the circular output window are expected to be small. The cross-polarized fields are small; the E_z field is 14 dB lower than the E_y value, and the E_x field is even lower.
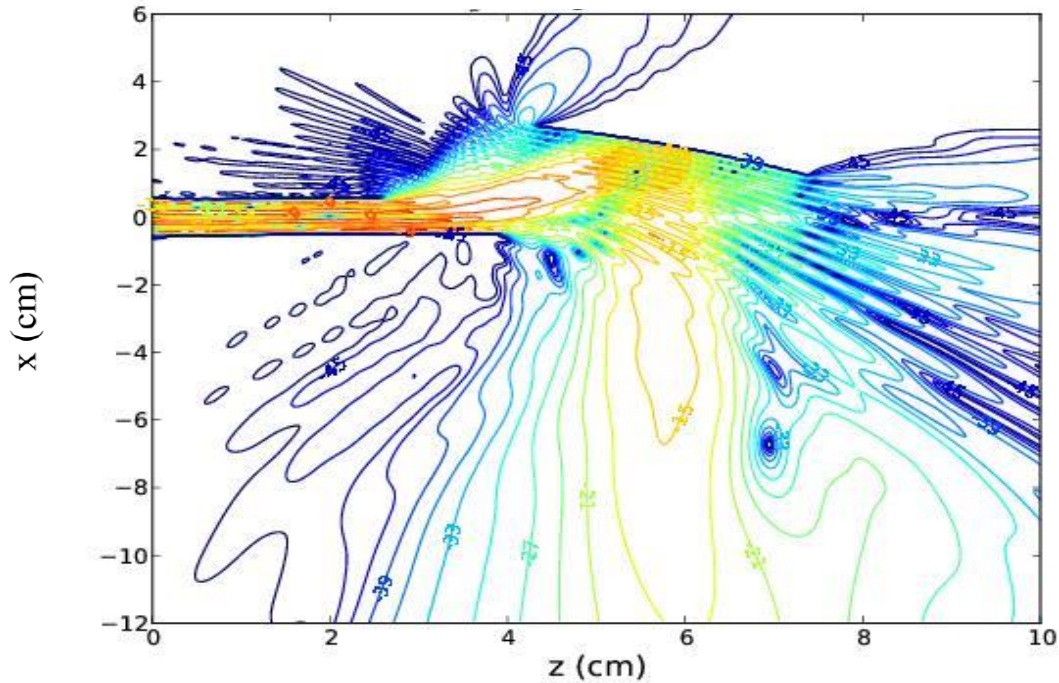

Figure 7.3.1: Contour plots of the side view of the fields ($\left| E_y \right|$) of the whole system along the center symmetry xz plane obtained from Surf3d. The contours are in 3 dB increments.
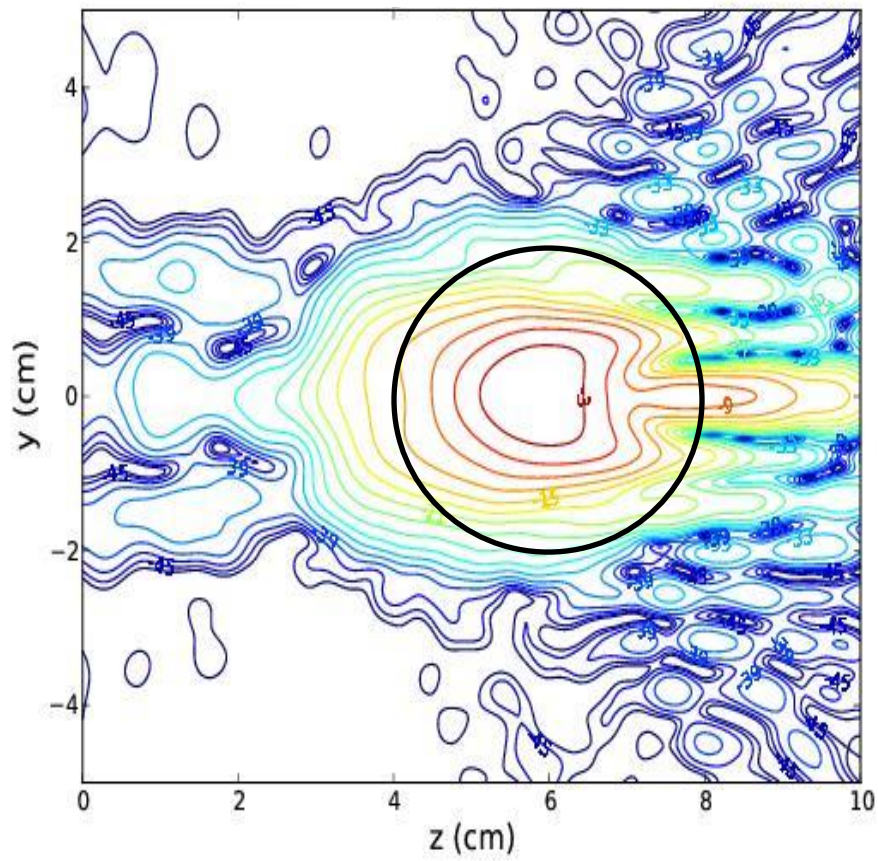
Figure 7.3.2: Contour plots of the $|E_x|$ field at the $x = -9$ cm output plane obtained from Surf3d. The contours are in 3 dB increments. The black circle is the output window.

Chapter 8: Summary, Conclusions and Suggestions for Future Investigations

For this dissertation, a new method for the design of any perturbed-wall TE_{0n} launcher that is not too highly oversized has been developed and analyzed in detail. This design method is a fusion of three types of theory, methods or algorithms. The K-S method is the optimization method, the ISC algorithm is used for fast and accurate field propagation inside a waveguide, and the GO theory bridges everything together. The ISC is the key in enabling this launcher design method to work for highly oversized launchers.

Three distinct perturbed-wall launchers that cover a wide range of OFs and frequency were designed using this launcher design method. Algorithmic and design parameters for all three launchers were optimized to obtain the best results. The first two launchers, the PoM and HSX launchers, are highly oversized external launchers while the last launcher, the ADS launcher, is a compact internal launcher. In general, highly oversized launchers have been difficult to design in the past, and this new launcher design method is a large improvement over previous launcher design methods that do not work well for highly oversized launchers.

Good to excellent results have been achieved, and all launcher design objectives are met for all three launchers. The resulting launcher output radiation patterns are a huge improvement over the smooth-wall launchers. For the perturbed-wall PoM launcher, in the near-field, the main lobe has a high Gaussian content with low side lobes, and the fields on the launcher edges are reduced so as to mitigate edge diffraction losses. In the far-field, the main lobe of the co-polarization contains nearly all of the radiated power. These improvements are true too for the HSX and ADS launchers, but to a lesser extent because the launcher lengths are inadequately long to obtain the best output radiation results. The perturbed-wall HSX launcher is relatively moderate in length to prove that some minimum level of improvement in the output radiation pattern is possible, and the launcher length can always be increased later to get better results. The perturbed-wall internal compact ADS launcher is relatively short in length due to the length restriction imposed by the compact gyrotron that houses it, and its output radiation pattern improvements over the smooth-wall launcher is modest. Additionally for the perturbed-wall PoM launcher, the modal composition and field shaping evolution on the launcher surface were described. Each designed perturbation profile in all three launchers is smooth and small so they are all machinable. All of the radiation patterns were independently verified using Surf3d.

The corresponding mirror system for each launcher was also analyzed in order to fully evaluate the performance of the complete QOMC system. The mirror system functions to collect and shape the main lobe of the output radiation pattern from the perturbed-wall launchers into as close a circular TEM_{00} mode as possible. The PoM mirror system is composed of two toroidal mirrors, and the total QOMC system output for this launcher is a highly Gaussian beam. In the internal gyrotron of the ADS, only a single toroidal mirror was used, and the result at the gyrotron output window is not a fully Gaussian beam. For the HSX mirror system, a comparison study of the radiation pattern after the first parabolic mirror between the smooth-wall and perturbed-wall HSX launchers was done. All field analyses were conducted using Surf3d.

There are several issues and problems related to this launcher design method, and they can be grouped into two categories, the first one being computational or algorithmic limitations. Most of the large number of algorithmic and design parameters are only optimized manually one parameter at a time, and this step can be a laborious and time-consuming process. Once these optimized parameters are known, the launcher synthesis process is relatively quick to implement, ranging from minutes to a few hours, depending on the computational size. The usage of FFTs in the ISC method has three main drawbacks, being 1) the perturbation profile can only have a maximum density of 10 points/wavelength, 2) field accuracy at the output aperture and after the launcher cut can be inadequate, depending on certain circumstances, and 3) limits the OF of launchers that can be designed using this launcher design method. The K-S optimization method only allows for indirect control over the output radiation pattern side lobes through the choice of the maximum perturbation size. With correct and careful implementation, all of these computational issues can be contained to obtain the best launcher perturbation profile. The second category of problems is physical limitations. The reduction of side lobes in the perturbed-wall launcher output radiation pattern necessitates that the far-field polar spread of the main lobe to be larger compared to the smooth-wall launcher case. The back propagated target Gaussian beam is not a waveguide eigenmode, and therefore cannot truly propagate in a waveguide, but certain computational steps can be taken to circumvent this problem.

There are multiple fronts of follow-up work that can be pursued for this research. One of them is to conduct further analysis of the launcher, for example using coupled-mode theory to analyze the modal evolution and field reflection due to the perturbation profile. Some other electromagnetics simulation software, such as Computer Simulation Technology (CST) can be utilized to calculate the field and modal reflections at the launcher start and

also at the launcher cut. The second avenue for continued research could include improving certain parts of the launcher design method. A more accurate way of modeling the fields at the launcher output aperture and after the launcher cut can be explored. Other sophisticated optimization methods that could lead to the global optimum solution, such as a genetic algorithm or simulated annealing, could also be looked into as potential upgrades over the current K-S phase-correcting algorithm. Lastly, this launcher design method could be extended to design other related electromagnetic antennas or devices. The clearest example would be adding perturbations to circular waveguide or horn antennas to change the directivity and/or reduce the side lobes of the far-field radiation pattern. Another example would be to generalize this launcher design method to incorporate more complex launchers, such as Communications and Power Industries' (CPI) VGT-8117 launcher, which is a tapered $TE_{20,9}$ rotating mode launcher operating at 117.5 GHz.

It is hoped that the research presented in this dissertation will be useful to not only the gyrotron research community, but also to the broader scientific community and engineering profession.

Appendix A

Review of Gaussian Beams

A Gaussian beam is a transverse electromagnetic (TEM_{mn}) mode, and it is an exact solution to the paraxial Helmholtz equation. For a Gaussian beam propagating in the $+\mathbf{z}$ direction, the paraxial Helmholtz equation is

$$\frac{\partial^2 u_{mn}}{\partial x^2} + \frac{\partial^2 u_{mn}}{\partial y^2} - 2j\beta \frac{\partial u_{mn}}{\partial z} = 0, \tag{A.1}$$

where β is the propagation constant of the beam. The Gaussian beam can be expressed as a family of general solutions

$$u_{mn}(x, y, z) = u_{m,x}(x, z)u_{n,y}(y, z), \tag{A.2}$$

where

$$u_{m,x}(x, z) = \left(\frac{2}{\pi}\right)^{1/8} \frac{1}{\sqrt{2^m w_x m!}} H_m\left(\frac{\sqrt{2}x}{w_x}\right) e^{-j\frac{\beta z_x - \phi_x}{2}} e^{-x^2 \frac{j\beta}{2q_x}},$$

$$u_{n,y}(y, z) = \left(\frac{2}{\pi}\right)^{1/8} \frac{1}{\sqrt{2^n w_y n!}} H_n\left(\frac{\sqrt{2}y}{w_y}\right) e^{-j\frac{\beta z_y - \phi_y}{2}} e^{-y^2 \frac{j\beta}{2q_y}}. \tag{A.3}$$

The functions $H_{m/n}$ are the Hermite polynomials of order m or n. The Hermite polynomials can be written explicitly as

$$H_m(x) = m! \sum_{\xi=0}^{\lfloor m/2 \rfloor} \frac{(-1)^\xi}{\xi!(m - 2\xi)!} (2x)^{m-2\xi}, \tag{A.4}$$

and the first five Hermite polynomials are

$$
\begin{aligned}
H_0(x) &= 1 \\
H_1(x) &= 2x \\
H_2(x) &= 4x^2 - 2 \\
H_3(x) &= 8x^3 - 12x \\
H_4(x) &= 16x^4 - 48x^2 + 12.
\end{aligned}
\tag{A.5}
$$

The other parameters are defined as

$$
z_x = z - z_{0x} \ , \ \mathbf{z}_y = z - z_{0y}
$$

$$
z_{R_x} = \frac{\beta w_{0x}^2}{2} \ , \ \mathbf{z}_{R_y} = \frac{\beta w_{0y}^2}{2}
$$

$$
w_x^2 = w_{0x}^2 \left(1 + \left(\frac{z_x}{z_{R_x}}\right)^2\right) \ , \ w_y^2 = w_{0y}^2 \left(1 + \left(\frac{z_y}{z_{R_y}}\right)^2\right)
$$

$$
R_x = z_x \left(1 + \left(\frac{z_{R_x}}{z_x}\right)^2\right) \ , \ R_y = z_y \left(1 + \left(\frac{z_{R_y}}{z_y}\right)^2\right)
\tag{A.6}
$$

$$
\phi_x = (1 + 2m)\tan^{-1}\left(\frac{z_x}{z_{R_x}}\right) \ , \ \phi_y = (1 + 2n)\tan^{-1}\left(\frac{z_y}{z_{R_y}}\right)
$$

$$
\frac{1}{q_x} = \frac{1}{R_x} - j\frac{2}{\beta w_x^2} \ , \ \frac{1}{q_y} = \frac{1}{R_y} - j\frac{2}{\beta w_y^2},
$$

where the z_0's are the location of the waist planes, w_0's are the waist values at the waist planes, w's are the beam waist values to the 1 Np points, the R's are the radii of curvature of the beams' wavefronts, z_R's are called the Rayleigh ranges and ϕ's are extra phase components called the Guoy phase shifts. From this point onwards, the following analysis will focus solely on the fundamental TEM$_{00}$ mode, u_{00}. A circular Gaussian beam has $w_{0x} = w_{0y}$ (but not necessarily $z_{0x} = z_{0y}$), and an astigmatic Gaussian beam has different waist planes ($z_{0x} \neq z_{0y}$). Figure A.1 displays some of these parameters on a two-dimensional Gaussian beam cross-section.
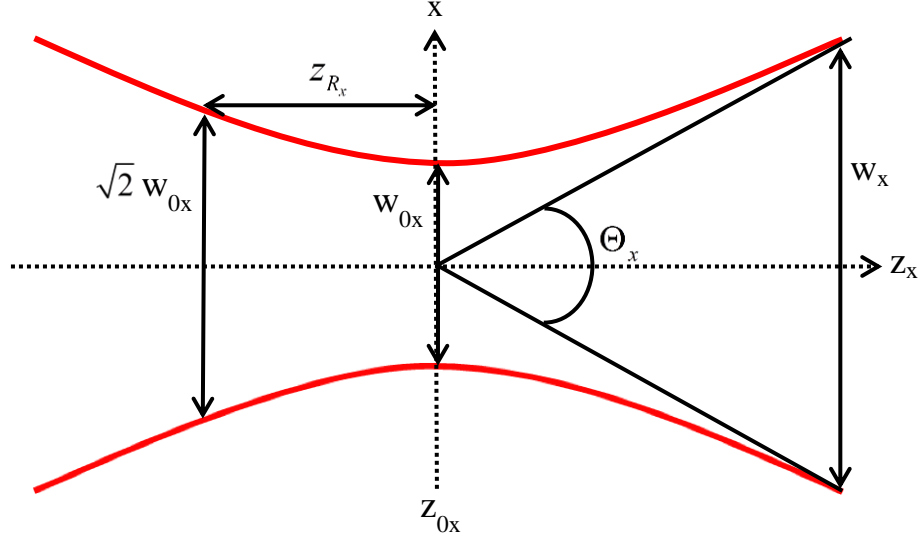
Figure A.1: Illustration of some Gaussian beam parameters on the x-z plane. The red lines are the 1 Np points below the axis value.

The total angular spread of the Gaussian beam far away from the waist can be approximated as

$$\Theta_x \approx \frac{\lambda}{\pi w_{0x}}, \ \Theta_y \approx \frac{\lambda}{\pi w_{0y}}, \tag{A.7}$$

but this only applies to beams with waist values larger than λ / π. For a magnetic vector potential defined as

$$\mathbf{A} = u_{00}(x, y, z)\hat{\mathbf{x}}, \tag{A.8}$$

the magnetic field can be approximated as

$$\mathbf{H} = -\frac{j\beta}{\mu_o}\left(u_{00}\hat{\mathbf{y}} - \frac{j}{\beta}\frac{\partial u_{00}}{\partial y}\hat{\mathbf{z}}\right), \tag{A.9}$$

where the $\dfrac{\partial u_{00}}{\partial z}$ term of the **y** component is small compared to βu_{00}, and it is ignored. The electric field can be approximated as

$$\mathbf{E} = -j\omega\left(u_{00}\hat{\mathbf{x}} - \frac{j}{\beta}\frac{\partial u_{00}}{\partial x}\hat{\mathbf{z}}\right),\tag{A.10}$$

and the $\dfrac{\partial^2 u_{00}}{\partial x^2}$ and $\dfrac{\partial^2 u_{00}}{\partial x \partial y}$ terms are approximated as zero. These field approximations are good only for the case

where the waist values are larger than λ/π [45, pp.113-116].

Appendix B

Correlation Coefficients

Commonly used figures of merit for evaluating the Gaussian TEM_{00} content of radiation patterns are the coupling coefficients. Three types of coupling coefficients are used throughout this report and in literature. For two vector functions **A** and **B**, the complex vector coupling coefficient is defined as

$$c_{cv} = \frac{\left| \iint_S (\mathbf{A} \cdot \mathbf{B}^*) \, dS \right|^2}{\left(\iint_S |\mathbf{A}|^2 \, dS \right) \left(\iint_S |\mathbf{B}|^2 \, dS \right)}, \tag{B.1}$$

where the integral is taken over a cross-section on a smooth surface. If only a particular field component is of interest, for instance the **x** component, then the complex scalar coupling coefficient can be defined as

$$c_{cs} = \frac{\left| \iint_S (A_x \cdot B_x^*) \, dS \right|^2}{\left(\iint_S |A_x|^2 \, dS \right) \left(\iint_S |B_x|^2 \, dS \right)}. \tag{B.2}$$

Another type of coupling coefficient is the amplitude coupling coefficient which is

$$c_a = \frac{\left| \iint_S (A_x B_x) \, dS \right|^2}{\left(\iint_S |A_x|^2 \, dS \right) \left(\iint_S |B_x|^2 \, dS \right)}, \tag{B.3}$$

and here only the amplitude information is included (the phase information is ignored).

Appendix C

Derivation of the Green's function Used in the ISC

There are many forms of Green's function that can be used for cylindrical coordinate systems. As stated in Section 4.3, the Green's function used in the ISC method in Eq. (4.2.2) is chosen because this form enables the whole ISC method to be calculated using FFTs.

For a cylindrical coordinate system, the Green's function, $G(\mathbf{r},\mathbf{r'})$, should satisfy the following partial differential equation

$$\nabla^2 G(\mathbf{r},\mathbf{r'}) + \beta^2 G(\mathbf{r},\mathbf{r'}) = \frac{1}{\rho}\delta(\rho - \rho')\delta(\phi - \phi')\delta(z - z'), \tag{C.1}$$

where $\mathbf{r}$ is the observation vector, $\mathbf{r'}$ is the source vector and β is the propagation constant. The delta function in Eq. (C.1) is expressed for no ρ, ϕ and z source dependence. Since the ϕ and z domains are unrestricted, i.e. $0 \le \phi \le 2\pi$ and $-\infty < z < +\infty$, the Green's function can be rewritten as an infinite Fourier series of

$$G(\mathbf{r},\mathbf{r'}) = \frac{1}{(2\pi)^2}\int_{-\infty}^{+\infty}\sum_{m=-\infty}^{+\infty} g_m(\rho,\rho')e^{-jm(\phi-\phi')}e^{-j\beta_z(z-z')}d\beta_z, \tag{C.2}$$

whose eigenvalues in ϕ and z satisfy the periodicity requirements, and $\beta^2 = \beta_\rho^2 + \beta_z^2$. From Eq. (C.2), the Green's function has now been reduced to $g_m(\rho,\rho')$, which is only a function of ρ. Plugging in Eq. (C.2) into Eq. (C.1) and then applying orthogonality conditions, Eq. (C.1) reduces to

$$\frac{1}{\rho}\frac{\partial}{\partial\rho}\left(\rho\frac{\partial g_m}{\partial\rho}\right) + \left(\beta_\rho^2 - \frac{m^2}{p^2}\right)g_m = \frac{1}{\rho}\delta(\rho - \rho'). \tag{C.3}$$

Without going into too much detail, Eq. (C.3) can be converted to a one-dimensional Sturm-Liouville type differential equation [30, pp. 897-902] where the solution is known. The homogeneous solutions to the differential equation of Eq. (C.3) can be written as

$$g_m^{(1)}(\rho,\rho') = A_m J_m(\beta_\rho\rho) + B_m Y_m(\beta_\rho\rho) \text{ for } \rho < \rho'$$

$$g_m^{(2)}(\rho,\rho') = C_m H_m^{(1)}(\beta_\rho\rho) + D_m H_m^{(2)}(\beta_\rho\rho) \text{ for } \rho > \rho',$$

(C.4)

where A_m, B_m, C_m and D_m are constants. For $\rho < \rho'$, the fields must be finite everywhere including at $\rho = 0$, so $B_m = 0$. In the $\rho > \rho'$ region, for $e^{j\omega t}$ time variations, only the radially outgoing field component is taken into account, resulting in $C_m = 0$ (i.e. the radially incoming field component is set to zero to exclude any field contributions from all other sources in the $\rho > \rho'$ region). The general solution to this form of Sturm-Liouville differential equation [30, pp. 860-865] is

$$g_m(\rho,\rho') = \frac{g_m^{(2)}(\rho',\rho)g_m^{(1)}(\rho,\rho')}{\rho' W(\rho')} \text{ for } \rho < \rho'$$

(C.5a)

$$g_m(\rho,\rho') = \frac{g_m^{(1)}(\rho',\rho)g_m^{(2)}(\rho,\rho')}{\rho' W(\rho')} \text{ for } \rho > \rho'$$

(C.5b)

where $W(\rho')$ is known as a Wronskian. The Wronskian for Bessel functions can be expressed as [30, pp. 902]

$$W(\rho') = \frac{2}{j\pi\rho'} A_m D_m.$$

(C.6)

Finally, combining Eqs. (C.6), (C.5) and (C.4) back into Eq. (C.2) gives Eq. (4.2.2) which is restated below

$$G(\mathbf{r},\mathbf{r}') = \frac{j}{8\pi} \int_{-\infty}^{\infty} \sum_{m=-\infty}^{\infty} J_m(\beta_\rho\rho) H_m^{(2)}(\beta_\rho\rho') e^{-jm(\phi-\phi')} e^{-j\beta_z(z-z')} d\beta_z \text{ for } \rho < \rho'$$

$$G(\mathbf{r},\mathbf{r}') = \frac{j}{8\pi} \int_{-\infty}^{\infty} \sum_{m=-\infty}^{\infty} J_m(\beta_\rho\rho') H_m^{(2)}(\beta_\rho\rho) e^{-jm(\phi-\phi')} e^{-j\beta_z(z-z')} d\beta_z \text{ for } \rho > \rho'.$$

(C.7)

At $\rho = \rho'$, both forms of the Green's function can be used since the derivation of Eq. (C.5) enforces that the solution is continuous at $\rho = \rho'$.

Appendix D

Investigation of the Effects of Spurious Modes

The assumption thus far is that the gyrotron cavity and uptaper generate only a pure single incident main mode, however, gyrotrons do generate several other unwanted modes called spurious modes. Sometimes these spurious modes have deleterious effects on the gyrotron operation and typically it is difficult for the mode converter to capture these spurious modes and convert them into usable power (i.e. the TEM_{00} or HE_{11} mode). For well-designed gyrotrons, these spurious modes are small and can be neglected. Gyrotron spurious modes can be roughly divided into two categories, 1) spurious modes generated by the complex electron beam, magnetic field and microwave interaction in the gyrotron cavity, and 2) spurious modes caused by uptapers and/or downtapers in the field pathway inside the gyrotron. Normally the first category has different frequencies than the main gyrotron output mode. The second type has the same frequency as the gyrotron output mode, and they also share certain similar modal symmetry characteristics as the gyrotron output mode, i.e. a TE_{0n} gyrotron would have other TE_{0n} spurious modes. For the 28 GHz HSX launcher, it is estimated that the first type of spurious modes are TE_{22} and TE_{32}, and the second type of spurious modes are TE_{01} and TE_{03}. For the TE_{22} and TE_{32} spurious modes, their frequencies, polarizations (i.e. rotating or stationary), amplitudes, and phases and rotational tilts at the start of the launcher (with respect to the main gyrotron output mode) are all unknown. For the TE_{01} and TE_{03} spurious modes, these are stationary modes, and only the amplitude and phases (at the start of the launcher) are unknown. It can be estimated that the sum of all spurious modes constitutes less than 10% of the total gyrotron output power for the HSX gyrotron [12].

For the launcher design method in Chapter 5, the launcher is only designed for one main gyrotron output mode, with the spurious modes ignored. Incorporating the spurious modes into the launcher design method to produce a better multi-modal launcher output radiation pattern is not expected to work for TE_{02} launchers, because of the highly different waveguide parameters of these spurious modes. Nonetheless, there is a way of minimizing the magnitude of the main lobes of spurious modes (which are now considered as side lobes of the system), and it is by optimizing the phases of these spurious modes (i.e. the phase relative to the main gyrotron output mode) at the start of the launcher. Changing this phase value might or might not be practical, but analyzing their impacts could shed some light on the effects of spurious modes in the output radiation pattern.

In this Appendix, the output of the perturbed-wall HSX launcher described in Section 6.5 will be studied for the spurious TE_{01} and TE_{03} modes individually. Figures D.1 and D.2 show respectively the far-field radiation pattern for a 5% TE_{01} and TE_{03} spurious mode power level with the main TE_{02} mode. The TE_{01} side lobe (which is a main lobe of the TE_{01} spurious mode, but is now considered a side lobe of the TE_{02} launcher because it is undesirable) has a smaller axial bounce angle than the TE_{02} mode, so this side lobe is located below the TE_{02} main lobe in the far-field plot of Fig. D.1. The TE_{03} side lobe (which is a main lobe of the TE_{03} spurious mode, but is again considered a side lobe of the TE_{02} launcher because it is also undesirable) has a larger axial bounce angle than the TE_{02} mode, so it is located above the TE_{02} main lobe in the far-field plot of Fig. D.2. For the TE_{01} spurious mode, it can be seen that the magnitude of the TE_{01} side lobe is higher for a 0° phase difference (Fig. D.1a) compared to a 180° phase difference (Fig. D.1b). Correspondingly for the TE_{03} spurious mode, the magnitude of the TE_{03} side lobe is higher for a 0° phase difference (Fig. D.2a) compared to a 180° phase difference (Fig. D.2b). Through the process of constructive and destructive interference, there will be an optimum phase difference value for the spurious modes that will yield the smallest spurious mode side lobes. It is very difficult to theoretically or mathematically determine what this optimized phase difference value is because it is a function of the spurious mode power level, and also the launcher length and perturbation profile; coupled-mode equations would be needed to track and analyze the field and modal propagation and reflection throughout the launcher length, and the reflection at the launcher cut must also be taken into account. The phase values chosen in the simulations of Figs. D.1 and D.2 are meant to highlight the point that it is possible to minimize the magnitude of the spurious mode side lobe by changing the phase difference value; however, these chosen phase values are not the globally optimized value. To obtain the globally optimized phase difference value, painstaking and time-consuming Surf3d simulations for different phase difference value must be done, and this could easily take up an inordinate amount of time.

Figures D.3 and D.4 respectively show the far-field radiation patterns for the TE_{01} and TE_{03} spurious mode with the main TE_{02} mode, but for a 10% spurious mode power level. In this Appendix, the spurious mode side lobe minimization step is only done for individual spurious modes; the optimization for multiple spurious modes is possible, but it would involve a greater amount of permutations and time, and success is not guaranteed. Correspondingly, extending this optimization effort to multi-frequency and/or multi-modal spurious modes could be too intractably complex to implement.
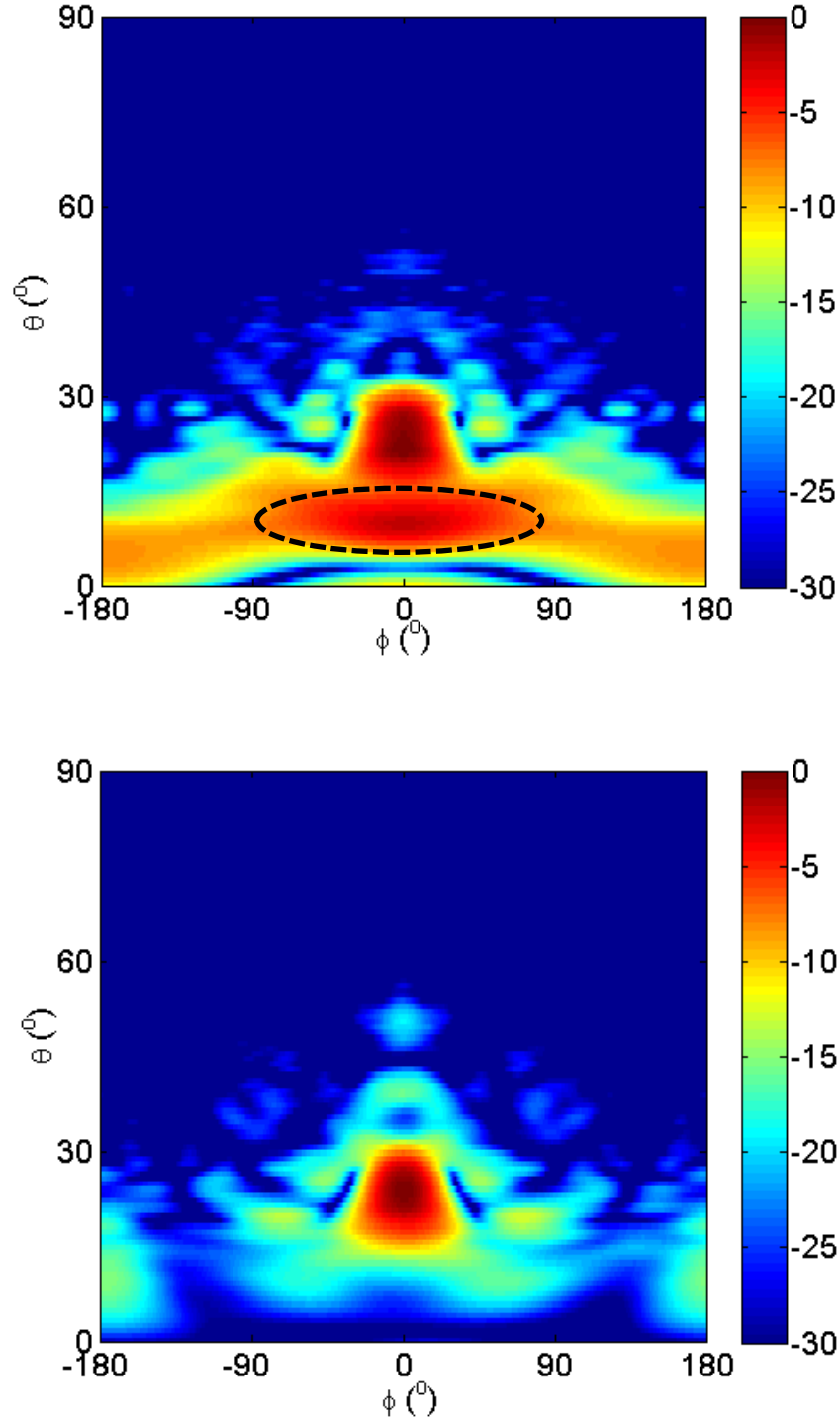
Figure D.1: The far-field pattern of $\left|E_\phi\right|$ (co-polarization) of the perturbed-wall HSX launcher (in dB) obtained from Surf3d for a 5% TE_{01} spurious mode power level with the main TE_{02} mode. Above (a) 0° phase difference, and below (b) 180° phase difference. The spurious mode side lobe is circled in black dotted lines.

Figure D.2: The far-field pattern of $\left|E_\phi\right|$ (co-polarization) of the perturbed-wall HSX launcher (in dB) obtained from Surf3d for a 5% TE_{03} spurious mode power level with the main TE_{02} mode. Above (a) 0° phase difference, and below (b) 180° phase difference. The spurious mode side lobe is circled in black dotted lines.
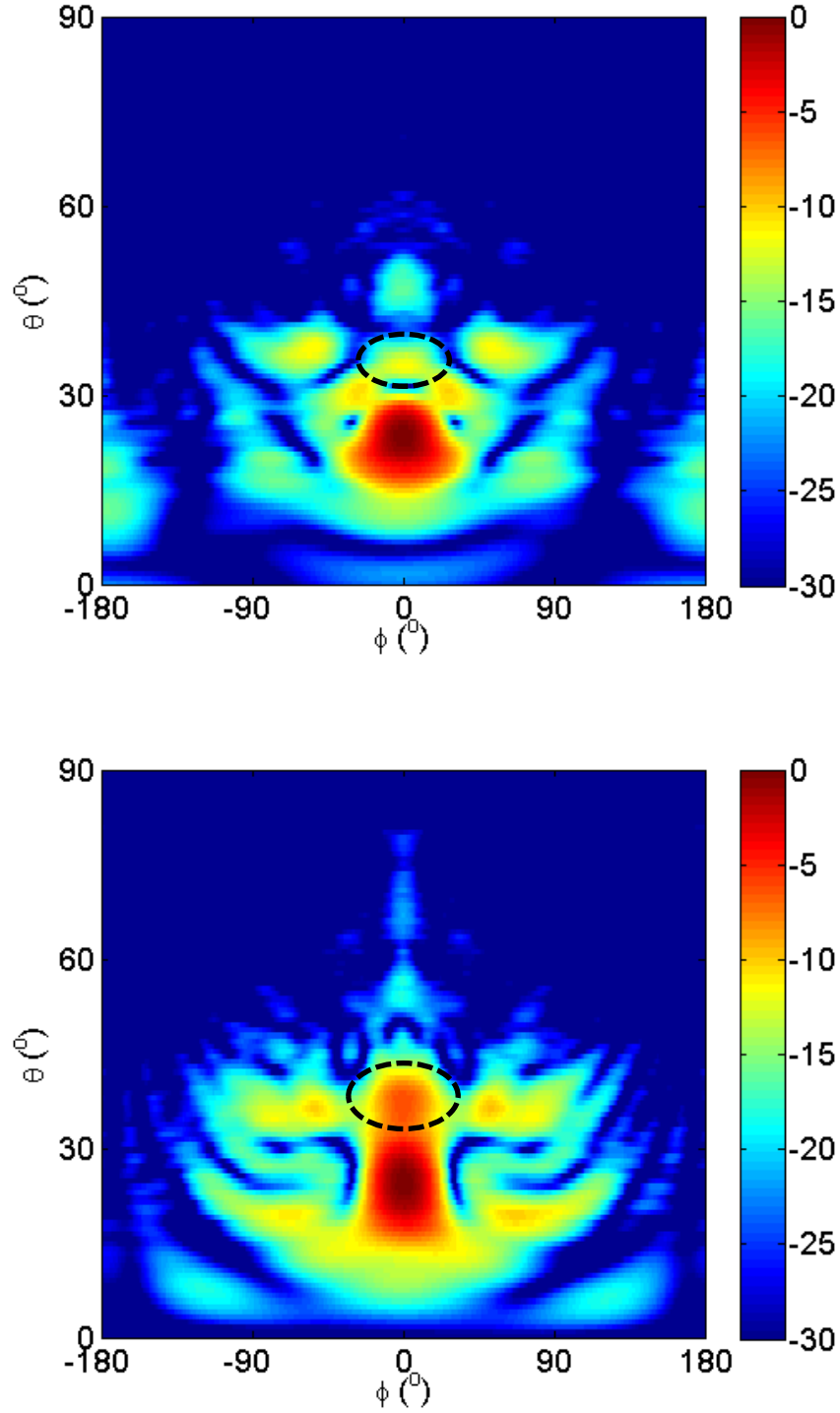
Figure D.3: The far-field pattern of $\left|E_\phi\right|$ (co-polarization) of the perturbed-wall HSX launcher (in dB) obtained from Surf3d for a 10% TE_{01} spurious mode power level with the main TE_{02} mode. Above (a) 0° phase difference, and below (b) 180° phase difference. The spurious mode side lobe is circled in black dotted lines.
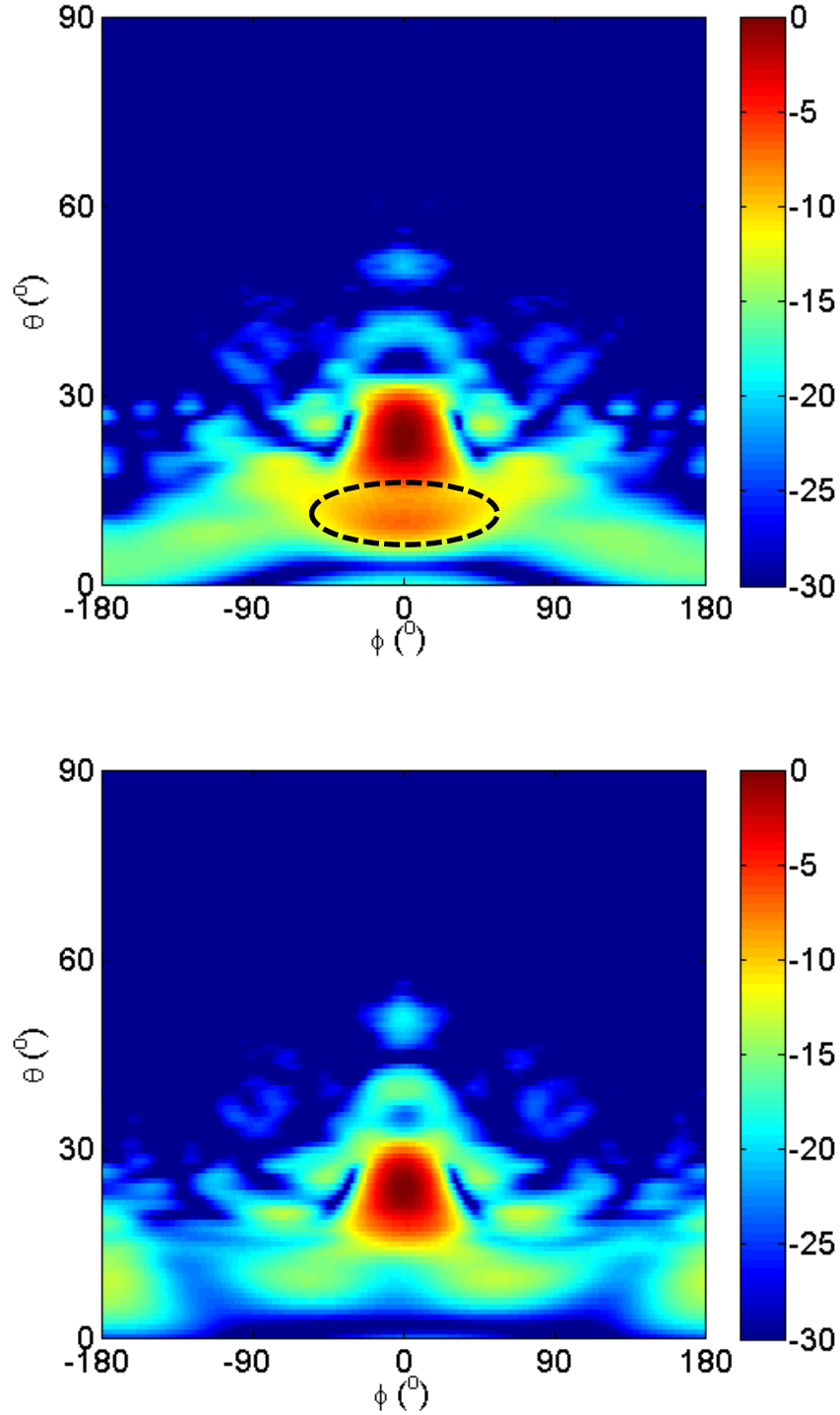
Figure D.4: The far-field pattern of $\left|E_\phi\right|$ (co-polarization) of the perturbed-wall HSX launcher (in dB) obtained from Surf3d for a 10% TE_{03} spurious mode power level with the main TE_{02} mode. Above (a) 0° phase difference, and below (b) 180° phase difference. The spurious mode side lobe is circled in black dotted lines.
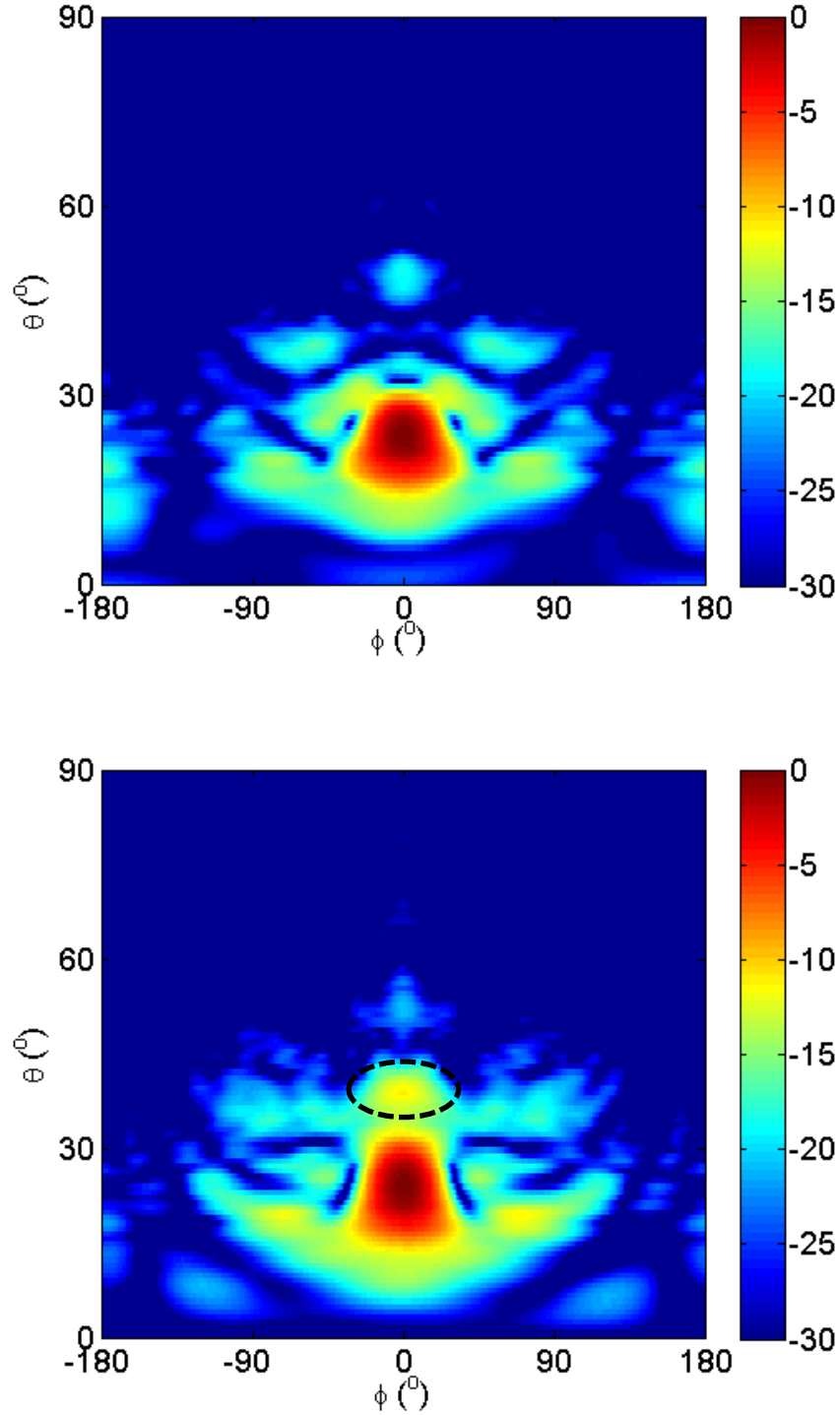
References

1. K. Felch, H. Huey, and H. Jory, "Gyrotrons for ECH applications," *J. Fusion Energy*, vol. 9, no. 1, pp. 59–75, 1990.

2. G. S. Nusinovich *et al., Modern Microwave and Millimeter-Wave Power Electronics*. New York, NY: Wiley, 2005, pp. 4-15.

3. J. P. Anderson, "Experimental study of a 1.5-MW, 110-GHz gyrotron oscillator," Ph.D. dissertation, Dept. Elect. Eng. and Comp. Sci., MIT, Cambridge, MA, 2005.

4. K. Chu, "The electron cyclotron maser," *Rev. Modern Phys.,* vol. 76, no. 2, pp. 489–540, Apr. 2004.

5. M. E. Read, "Depressed collectors for high-power gyrotrons," *IEEE Trans. Elec. Dev.*, vol. 37, no. 6, pp. 1579–1589, Jun. 1990.

6. M. Henderson *et al.*, "An overview of the ITER electron cyclotron H&CD system," in *34th Int. Conf. on Infrared, Millim. and Terahertz Waves*, Busan, Korea, Sep. 2009.

7. U. F. Ungku Farid and R. J. Vernon, "Some calculations concerning variable spacing double disk windows for possible use in step-tunable gyrotrons," in *Joint 32nd Int. Infrared Millim. Waves Conf./ 15th Int. Terahertz Electron. Conf.*, Cardiff, UK, Sep. 2007.

8. M. J. Buckley, G. H. Luo, and R. J. Vernon, "New compact broadband high-efficiency mode converters for high power microwave tubes with TE_{0n} or TM_{0n} mode outputs," in *IEEE MTT-S Int. Microw. Symp. Dig.*, NY, USA, May 1988, pp. 797-800.

9. M. J. Buckley and R. J. Vernon, "Compact quasi-periodic and aperiodic TE_{0n} mode converters in overmoded circular waveguides for use with gyrotrons," *IEEE Trans. Microw. Theory Tech.*, vol. 38, no. 6, pp. 712–721, Jun. 1990.

10. M. J. Buckley, D. A. Stein, and R. J. Vernon, "A single-period TE_{02}-TE_{01} mode converter in a highly overmoded circular waveguide," *IEEE Trans. Microw. Theory Tech.*, vol. 39, no. 8, pp. 1301–1306, Aug. 1991.

11. J. Shafii and R. J. Vernon, "Design of shorter TE_{11}-to-HE_{11} mode converters in a highly over-moded corrugated circular waveguide using a modified Chebyshev method," in *AP-S Dig. Antennas and Prop. Soc. Int. Symp.*, NY, USA, Jun. 1998, pp. 1290-1293.

12. K. Likin, private communications, HSX, 2012-2013.

13. J. W. Radder *et al.*, "Hybrid transmission line for ECRH in the helically symmetric experiment," *Int. J. Infrared Millim. Waves*, vol. 29, no. 4, pp. 360-372, Apr. 2008.

14. M. P. Perkins, "The design of beam shaping mirrors for gyrotrons to aid injection of an electromagnetic beam into a corrugated waveguide," Ph.D. dissertation, Dept. Elect. and Comp. Eng., UW-Madison, Madison, WI, 2004.

15. R. Cao, "Investigation of techniques for high frequency mirror system design for single frequency and multi-frequency gyrotrons" Ph.D. dissertation, Dept. Elect. and Comp. Eng., UW-Madison, Madison, WI, 2005.

16. X. Yang *et al.*, "Progress toward optimization of phase-correcting mirrors for a multifrequency 1-MW gyrotron," *IEEE Trans. Plasma Sci.*, vol. 34, no. 3, pp. 652–658, Jun. 2006.

17. M. P. Perkins and R. J. Vernon, "Mirror design for use in gyrotron quasi-optical mode converters," *IEEE Trans. Plasma Sci.*, vol. 35, no. 6, pp. 1747–1757, Dec. 2007.

18. S. Liao, R. J. Vernon, and J. Neilson, "A high-efficiency four-frequency mode converter design with small output angle variation for a step-tunable gyrotron," in *33rd Int. Conf. Infrared, Millim. and Terahertz Waves*, Pasadena, CA, Sep. 2008.

19. S. Liao, "Multi-frequency beam-shaping mirror system design for high power gyrotrons: theory, algorithms and methods," Ph.D. dissertation, Dept. Elect. and Comp. Eng., UW-Madison, Madison, WI, 2008.

20. B. Y. Rock, "Theoretical and algorithmic methods for integrated design of gyrotron internal mode conversion system," Ph.D. dissertation, Dept. Elect. and Comp. Eng., UW-Madison, Madison, WI, 2011.

21. A. Chirkov *et al.*, "Use of Huygens' principle for analysis and synthesis of the fields in oversized waveguides," *Radiophys. Quantum Electron.*, vol. 49, no. 5, pp. 344–353, 2004.

22. M. Blank, K. Kreischer, and R. Temkin, "Theoretical and experimental investigation of a quasi-optical mode converter for a 110-GHz gyrotron," *IEEE Trans. Plasma Sci.*, vol. 24, no. 3, pp. 1058–1066, 1996.

23. J. Jin *et al.*, "Novel numerical method for the analysis and synthesis of the fields in highly oversized waveguide mode converters," *IEEE Trans. Microw. Theory Tech.*, vol. 57, no. 7, pp. 1661–1668, 2009.

24. Y. Hirata *et al.*, "The design of a tapered dimple-type mode converter/launcher for high-power gyrotrons," *IEEE Trans. Plasma Sci.*, vol. 31, no. 1, pp.142–145, Feb. 2003.

25. J. Neilson, "Optimal synthesis of quasi-optical launchers for high power gyrotrons," *IEEE Trans. Plasma Sci.*, vol. 34, no. 3, pp. 635–641, Jun. 2006.

26. J. H. Flamm, J. Jin, and M. K. Thumm, "Wave propagation in advanced gyrotron output couplers," *Int. J. Infrared Millim. Waves*, vol. 32, no. 7, pp. 887-896, Jun. 2011.

27. G. G. Denisov *et al.*, "Synthesized quasi-optical TE_{02}-HE_{11} mode converter," in 3$4th^{d}$ *Int. Conf. Infrared, Millim. and Terahertz Waves*, Busan, Korea, Sep. 2009.

28. U. F. Ungku Farid, B. Y. Rock, and R. J. Vernon, "A highly oversized perturbed-wall TE_{02} launcher," in *37th Int. Conf. on Infrared, Millim. and Terahertz Waves*, Wollongong, Australia, Sep. 2012.

29. J. Neilson, "SURF3D and LOT: Computer codes for design and analysis of high-performance QO launchers in gyrotrons," in *Joint 29th Int. Infrared Millim. Waves Conf./12th Int. Terahertz Electron. Conf.*, Karlsruhe, Germany, Sep. 2004, pp. 667–668.

30. C. A. Balanis, *Advanced Engineering Electromagnetics*. New York: John Wiley & Sons, 1989.

31. R. E. Collin, *Foundations for Microwave Engineering*, 2nd ed. New York: IEEE Press, 1991.

32. A. A. Bogdashov and G. G. Denisov, "Asymptotic theory of high-efficiency converters of higher-order waveguide modes into eigenwaves of open mirror lines," *Radiophys. Quantum Electron.*, vo7. 49, no. 4, pp. 283–296, 2004.

33. M. Blank, "High efficiency quasi-optical mode converters for overmoded gyrotrons," Ph.D. dissertation, Dept. Elect. Eng. and Comp. Sci., MIT, Cambridge, MA, 1994.

34. M. Born and E. Wolf, *Principles of Optics*, 7th ed. Cambridge: Cambridge University Press, 1999, pp. 116-129.

35. S. N. Vlasov, L. I. Sagryadskaya, and M. I. Petelin, "Transformation of a whispering gallery mode, propagating in a circular waveguide, into a beam of waves," *Radio Eng.*, vol. 12, no. 10, pp.14-17, 1975.

36. B. Z. Katsenelenbaum and V. Semenov, "Synthesis of phase correctors shaping a specified field," *J. Rad. Elec.*, vol. 12, no. 2, pp. 223–231, 1967.

37. V. Veselago, "The electrodynamics of substances with simultaneously negative values of ε and μ," *Soviet Phys. Uspekhi*, vol. 10, no. 4, pp. 509–514, 1968.

38. D. C. Ghiglia and M. D. Pritt, *Two-Dimensional Phase Unwrapping*. New York: John Wiley & Sons, 1998.

39. B. Y. Rock and R. J. Vernon, "An improved numerical method for the analysis of the fields in a deformed waveguide," in *36th Int. Conf. on Infrared, Millim. and Terahertz Waves*, Houston, TX, Oct. 2011.

40. B. Y. Rock and R. J. Vernon, "A new method for the analysis of perturbed-wall waveguide mode converters," *IEEE Trans. Plasma Sci.*, vol. 40, no. 6, pp. 1502–1511, Jun. 2012.

41. W. M. Leach and D. T. Paris, "Probe compensated near-field measurements on a cylinder," *IEEE Trans. Antennas Propag.*, vol. 12, no. 4, pp. 435–445, 1973.

42. Q. Li, P. J. Sealy, and R. J. Vernon, "Preliminary work on a perturbed-wall Vlasov launcher for a TE_{0n} mode using surf3d," in *Joint 32nd Int. Infrared Millim. Waves Conf./ 15th Int. Terahertz Electron. Conf.*, Cardiff, UK, Sep. 2007.

43. U. F. Ungku Farid, B. Y. Rock, and R. J. Vernon, "A new design of a perturbed-wall TE_{02} launcher for a 60 GHz gyrotron," in *36th Int. Conf. on Infrared, Millim. and Terahertz Waves*, Houston, TX, Oct. 2011.

44. P. J. Sealy and R. J. Vernon, "Equivalence-principle model for radiation from TE_{0n} and TM_{0n} mode step-cut and slant-cut Vlasov feeds," in *AP-S Dig. Antennas and Prop. Soc. Int. Symp.*, Ontario, Canada, Jun. 1991, pp. 1836-1839.

45. H. Haus, *Waves and Fields in Optoelectronics*. Englewood Cliffs, New Jersey: Prentice-Hall, 1984.